Surface EXAFS Studies of Chromium and Titanium Upon α-Quartz (0001) Surfaces

Thesis submitted in accordance with the requirements of the
University of Liverpool for the degree of Doctor of Philosophy
by
Seán Paul Harte

September 1997

To my family, especially my parents and Laura, Marc, Becca,
Sarah Jane and Jemma.

"There is hope in honest error,
none in the icy perfections of the mere stylist."

Charles Rennie Mackintosh, Glasgow, 1901

Acknowledgments
(Or the without whom department!)

My first debt of thanks is without doubt to my supervisor Geoff Thornton for his assistance and also his goading of me where necessary.

Andi - for three very special years.

Unilever p.l.c. for financial support via a CASE award, especially Glyn Roberts and Christine Marsden.

Tony Banday for believing in me when I had severe doubts.

All my co-workers : Stevie -V- EEEEEHHHHH!!!!!, Chris for his tinkering, Harbs for the copious beers, Leon for listening even when I was talking complete crap, Vin for his excellent maintenance of 4.2 and the quality coffee, The Shed, Teresa all right dahlen, Peter, Paul Wincott, Sally, Paul Murray, Andy Robinson, Sergio, David Norman and Norman Binsted. And the inevitable cast of thousands from Leicester, Warwick, Nottingham and Cardiff.

Dr. D. Fischer for the use of the gas proportional counter.

Dr. F. Bart, Dr. M. Gautier-Soyer and Dr. S. Gota for their invaluable assistance in sample preparation.

A very special thank you to Dr. J.F.W. Mosselmans without whom this simply would not been completed.

Cat, Tommy, Charlie, Jono et al., for the beer.

The staff and certain customers, yes John that does mean you, of the Jabez Clegg Pub, a veritable home from home, especially Anna, Sam, Rachel S, Jamie, James, Rachel, Nicola, Manj, Wardy, Phil and Brian.

Abstract

In this thesis two studies of reactive metal adsorption upon a low index single crystal silicon dioxide surface are presented in addition to a study of sulphur adsorption upon a low index single crystal nickel surface.

Chromium growth upon the α-quartz $SiO_2(0001)$ $(\sqrt{84}\times\sqrt{84})R11^\circ$ surface is studied at three coverages, 0.25±0.08 ML, 0.5±0.16 ML and 1.0±0.33 ML, using surface extended x-ray absorption fine structure (SEXAFS). SEXAFS measurements, from the chromium K-edge, recorded at both grazing and normal incidence show that chromium growth proceeds via the formation of mesoscopic particles with a body centred cubic (b.c.c.) like structure having an average nearest neighbour Cr-Cr distance of 2.36±0.03 Å. This represents a contraction of 5.6 % from the bulk b.c.c. lattice spacing of 2.49 Å. There is no evidence of a surface reaction between chromium and the surface oxygen.

SEXAFS was used to study titanium reactional growth on α-quartz (0001) $(\sqrt{84}\times\sqrt{84})R11^\circ$ and (1x1). Three nominal coverages were studied, 0.25±0.08 ML, 0.5±0.16 ML and 1.0±0.33 ML. Both normal and grazing incidence SEXAFS data were recorded and show the formation of a spatially extensive region in which an interfacial reaction has occurred between surface oxygen and adsorbate titanium atoms. Coupled with this is the formation of subnanometre titanium clusters. The metal oxide has nearest neighbour Ti-O distances close to those of both the anatase and rutile forms of titania with the metallic titanium clusters having a Ti-Ti distance within experimental error that of bulk hexagonal close packed (h.c.p.) titanium, 2.89 Å.

A re-examination of the surface geometry of Ni(110)c(2x2)S using SEXAFS has been performed. Data out to an electron wavevector of 9 Å^{-1} are analysed with a new code to assess the influence of multiple scattering. The first shell S-Ni distance is determined to be 2.20±0.02 Å with the next nearest neighbour distance being 2.29±0.02 Å, giving a top-layer Ni expansion of 14±3% relative to the bulk. The influence of multiple scattering does not significantly alter these values from earlier studies.

Index

Chapter 1 Intoduction 1

Chapter 2 Theoretical Aspects 5

2.1 Introduction 6

2.2 X-ray Absorption Spectroscopy 6

2.2.1 EXAFS 8

2.2.2 NEXAFS 17

Chapter 3 Instrumentation 21

3.1 Introduction 22

3.2 The IRC NEXAFS Chamber 22

3.2.1 Vacuum Techniques 22

3.2.2 Level 1 24

3.2.3 Level 2 24

3.3 Sample Manipulation 27

3.3.1 Sample Transfer 27

3.4 Sample Characterisation 28

3.5 Metal Dosers 30

3.5.1 VSW ME10 Microevaporator 30

3.5.2 Titanium Filament 31

3.5.3 Electrodeposited Cr Source 31

3.6 Fluorescence Detectors 32

3.6.1 Gas Proportional Counter 33

3.6.2 Solid State Si-Li Detector 34

3.7 The SRS Daresbury Laboratory 36

3.7.1 Synchrotron Radiation 36

3.7.2 Beamline 4.2 39

Chapter 4 A SEXAFS study of α-quartz (0001)$(\sqrt{84}x\sqrt{84})$ R11° - Cr 44

4.1 INTRODUCTION 45

4.2 EXPERIMENT 46

4.3 RESULTS 50

4.4 DISCUSSION 60

4.4.1 Structural Considerations 60

4.4.2 Thermodynamic Considerations 62

4.4.3 Cr K-Edge XANES 65

4.5 Conclusion 65

Chapter 5 A SEXAFS study of α-quartz (0001)$(\sqrt{84}x\sqrt{84})$ R11° -Ti and α-quartz (0001)(1x1)-Ti 70

5.1 INTRODUCTION 71

5.2 EXPERIMENT 72

5.3 RESULTS 76

5.3.1 Ti Adsorption on the (1x1) (0001) α-quartz surface 76

5.3.2 Ti adsorption on α-quartz (0001) $(\sqrt{84}x\sqrt{84})$ R11° 94

5.4 DISCUSSION 97

5.4.1 General Considerations of TiOx Formation 97

5.4.2 Ti / SiO2 (0001) (1x1) 99

5.4.3 Ti / SiO2 (0001) $(\sqrt{84}x\sqrt{84})$ R11° 101

5.5 Conclusion 102

Chapter 6 A SEXAFS study of Ni(110)-Sc(2x2) 106

6.1 Introduction 107

6.2 Experimental 107

6.3 Results and Discussion 110

6.4 Conclusion 118

Chapter 1

Introduction

The adsorption of metals on oxides is an area of increasing interest in surface science.[1] This is due to the importance of such systems in areas as diverse as catalysis[2,3] and metalisation of semiconductors.[4] Another area of great interest is the poisoning of catalysts by sulphur containing molecules. The three studies described in this thesis deal with these two areas of current interest. The first two are experimental studies of the adsorption of highly reactive transition metals upon a low index face of a single crystal of silicon dioxide. The Cr - quartz system is intended as an idealised model of the Philips catalyst used in the polymerisation of ethene,[3] the addition of a small percentage by weight of Ti to this catalyst has been shown to alter the degree of branching, hence the density of the polythene produced,[3] this being the motivation behind the study of the Ti - quartz adsorption system. The third is an experimental study of a prototypical adsorption system of sulphur upon a low index face of a single crystal of nickel.

The two chapters which follow the Introduction describe the theoretical and instrumentational background to this work. Chapter 2 describes the theoretical details of surface extended x-ray absorption fine structure (SEXAFS) including descriptions of both the single scattering and multiple scattering formalisms used in the analysis of the data presented in this thesis. Chapter 3 describes the apparatus required for the experimental studies including a brief overview of vacuum techniques, sample manipulation and characterisation, detailed descriptions of the detection methods employed and a brief description of synchrotron radiation.

The first experimental study to be described is contained in chapter 4. This is an investigation of the α-quartz $(0001)(\sqrt{84}\times\sqrt{84})\,R11^{\circ}$ interface and is the first study of physical vapour deposition (P.V.D.) of a reactive transition metal upon single crystal silicon dioxide. SEXAFS measurements were employed at three coverages, 0.25±0.08 ML, 0.5±0.16 ML and 1.0±0.33 ML. The SEXAFS measurements, recorded at the Cr K-edge, are indicative of the formation of mesoscopic, b.c.c. like chromium particles with a nearest neighbour distance of 2.36±0.03 Å. This is a contraction of 5.6 % from the bulk b.c.c. nearest neighbour distance, 2.49 Å.

In chapter 5 SEXAFS studies of titanium adsorption on both the (1x1) and $(\sqrt{84}\mathrm{x}\sqrt{84})\,\mathrm{R}11^{\circ}$ terminations of a-quartz (0001) are reported.
Both normal and grazing incidence SEXAFS data were recorded and evidence of a spatially extensive, disordered sub-oxide of titanium is seen. This is manifested in the form of a Ti-O scattering pair with the Ti-O distances, at all coverages on both terminations, being very similar to the Ti-O distances in the anatase and rutile bulk phases of titania (1.96 Å - 2.03 Å). Also observed, simultaneously with the oxide formation, is the deposition of Ti in the form of metal atoms with a nearest neighbour distance very close to that of bulk h.c.p. titanium, 2.89 Å.

Chapter 6 is a multiple scattering study of a prototypical sulphur adsorption system, Ni(110)-Sc(2x2). The purpose of this study was in the commissioning of the IRCSS Beamline 4.2 with a well characterised and studied system.[4-7] In addition, data analysis was performed using a new variant of the Daresbury Laboratory EXCURVE code allowing the simultaneous fitting of up to three spectra thus exploiting crystallographic symmetry in order to increase the determinacy of the fit. The first S-Ni distance was found to be 2.20±0.02 Å with the next nearest neighbour distance being 2.29±0.02 Å. This corresponds to a top layer nickel expansion of 14±3 % relative to the bulk. Multiple scattering, whilst improving the fit quality, does not significantly modify these structural parameters.

References

1. C.T. Campbell, Surf. Sci. Rep., **27**, 1, (1997)

2. S.J. Tauster, S.C. Faung and R.J. Garten, J. Am. Chem. Soc., **100**, 170, (1978)

3. C.E. Marsden in "Preparation of Catalysts V", G. Poncelet, P.A. Jacobs, P. Grange and B. Delmon Eds., Elsevier Science Publishers B.V., Amstrdam, (1991)

4. K. Armstrong, Applied Materials HP PVD Update, **2**, 4, (1995)

5. S.W. Robey, J.J. Barton, C.C. Bahr, G. Liu and D.A. Shirley, Phys. Rev. B, **35**, 1108, (1987)

6. F. Sette, T. Hashizume, F. Comin, A.A. MacDowell and P.H. Citrin, Phys. Rev. Lett., **61**, 1384, (1988)

7. D.R. Warburton, G. Thornton, D. Norman, C.H. Richardson and R. McGrath, Phys. Rev. B, **43**, 12289, (1991)

Chapter 2

Theoretical Aspects

2.1 Introduction

This chapter provides a brief account of the theory employed to analyse the experimental results presented in this thesis. Firstly x-ray absorption theory is discussed. A more extensive review of these techniques can be found elsewhere.[1,2]

2.2 X-ray Absorption Spectroscopy

Initially X-ray Absorption Spectroscopy was used to provide a basic insight into the electronic structure of atoms and provided the experimental evidence for quantum theory. Then in the 1920's post absorption edge fine structure was observed in polyatomics.[2]

At the time, several opposing theories were advanced to explain this structure, amongst them that of Kronig.[3] He hypothesised that the fine structure arises following a photoelectron ejected from a core level by an x-ray, being scattered by neighbouring atoms. This idea is basically correct, although only a few studies were performed at the time. It was not until the early 1970's that this physics was exploited when Sayers, Stern and Lytle suggested that the post-edge fine structure could prove to be extremely powerful in the elucidation of the structure of solids.[4] Following their suggestion, which stimulated a great deal of new interest in x-ray absorption fine structure, the presently accepted theory for structural determination by XAS, which retains the basic principles of Kronig's original theory, was developed[5].

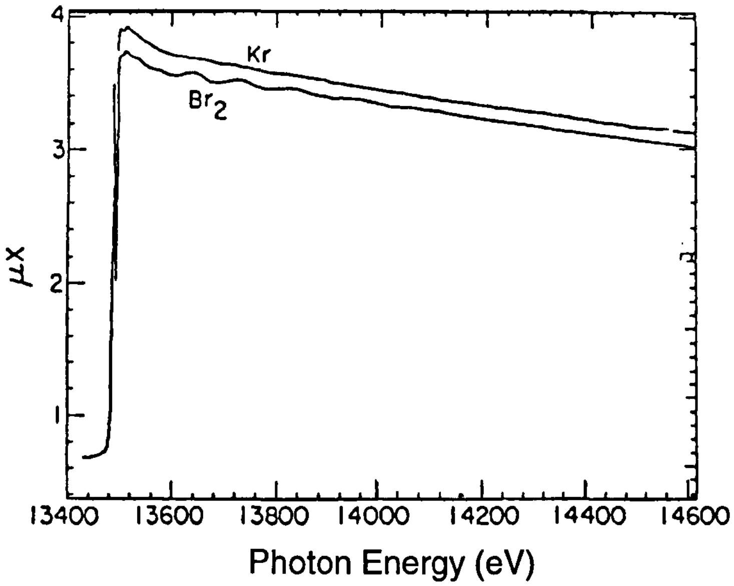

Figure 2.1 X-ray absorption spectra of monatomic Kr and diatomic Br_2. The Kr spectrum has been energy shifted to match the edge positions.

Figure 2.1 shows the x-ray spectra of monatomic Kr and diatomic Br_2. These two spectra are typical of x-ray absorption spectra in general. Firstly there is the sharp increase in the absorption profile , usually called an absorption edge. This edge corresponds to an increase in the absorption coefficient (μ) of an atomic sub-shell (in this case the 1s core level) as the energy of the x-ray beam, which is incident on the sample, is swept through the core level's threshold of electron excitation. Also there is the approximately exponential tail to the absorption edge, which is due to the decreasing overlap between the wave function of the outgoing photoelectron and atom and the wave function of the initial bound state. As well as displaying these features, which are characteristic of all x-ray absorption spectra, Figure 2.1 demonstrates that post edge fine structure is present only in polyatomic systems (i.e. Br_2). The obvious reason for this being that there are no atoms to scatter the outgoing photoelectron in monatomic systems. This fine structure is usually divided into two separate regions: firstly, the structure close to the edge, which is usually described as the near-edge x-ray absorption fine structure (NEXAFS), and secondly the extended x-ray absorption fine structure (EXAFS), which dominates from approximately 50 eV above the edge. The physics of these two regimes are discussed in the next two sections.

2.2.1 EXAFS

In quantum mechanics the photoabsorption coefficient (μ) of an atomic core shell is described as the probability of creating a core hole in that shell. Mathematically this may be written as

$$\mu \; \alpha < f \,|\, \mathbf{E.p} \,|\, i >, \qquad \text{Equation 2.1}$$

where, $| i>$, the initial state, is the core level, **E.p** is the interaction operator and $| f>$, the final state, is the photoelectron and ion. Note that the core level electron is excited into a continuum state in the EXAFS region. In a polyatomic system this outgoing photoelectron is partially backscattered by the surrounding atoms (see Figure 2.2) and the resulting backscattered photoelectron wave, which is shifted in phase relative to the outgoing photoelectron wave due to both the distance it has travelled and the potentials of the emitting and backscattering atoms,

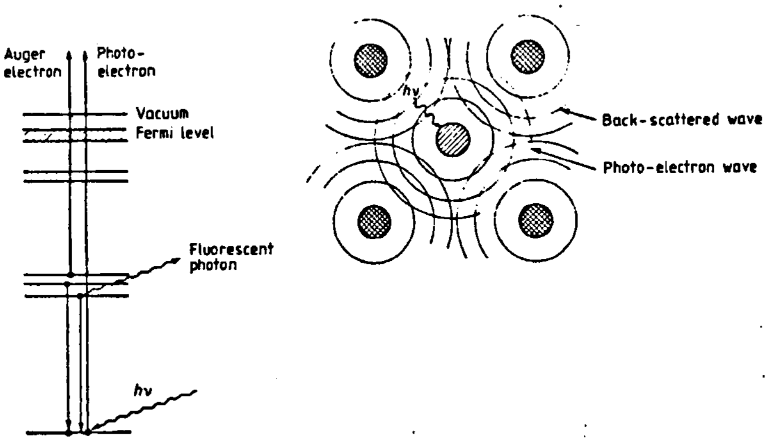

Figure 2.2 Schematics of both the photoabsorption and photoelectron scattering processes.

interferes with the original outgoing photoelectron wave. This final state interference , which need only be considered near to the centre of the absorber because the absorption coefficient is zero everywhere except where the initial state is non-zero, may be either destructive or constructive depending upon the phase difference between the two electron waves. Varying the incident x-ray energy changes the relative phase of the outgoing and backscattered waves and so the amplitude of the final state is modulated as a function of incident photon energy. It is this modulation of the final state, and thus the modulation of the x-ray absorption coefficient, which gives rise to the characteristic EXAFS "wiggles" in the post edge region of polyatomics. The wavelength of these wiggles depends upon the distance of the neighbouring atoms from the absorbing atom, and their amplitude depends upon the backscattering strength. Therefore, from this final state effect which is the fundamental basis of the EXAFS technique it is possible to gain structural data, even from systems with only short range order, since the final state modulation is derived from only near neighbour scattering.

Quantitative analysis of EXAFS data may be performed using plane wave single electron scattering theory. The expression:

$$\chi(k) = A(k) \sin [2kr_{ij}+\phi(k)] \qquad \text{Equation 2.2}$$

describes EXAFS, within this paradigm, for the most rudimentary case in which the EXAFS signal, $\chi(k)$, arises from a single shell of backscattering atoms at a distance r_{ij} from the central absorbing atom. The term $2kr_{ij}$ describes the phase difference between the two electron waves due to the separation of the backscattering atom (j) from the absorbing atom (i), where k is the photoelectron wavevector. $\phi(k)$ accounts for the phase shift due to the passage of the photoelectron wave through the potentials of the absorbing and backscattering atoms, and A(k) is the EXAFS amplitude term. A(k) is determined by a number of parameters: the number of backscattering atoms, the backscattering strength of these atoms, the disorder, both thermal and static, within the system, and finally the inelastic processes which affect the outgoing photoelectron. These factors are expressed quantitatively by the following equation,

$$A(k) = N^* \frac{f(k)}{kr^2} \exp(-2\sigma_i^2 k^2) \exp(-2r_i/\lambda(k)). \qquad \text{Equation 2.3}$$

Equation [3] holds as long as the initial state is an s-state (l=0), which is the case for all x-ray absorption data examined in this thesis. The term N* is related to the number of backscattering atoms. It is the effective co-ordination number of the central atom, which is employed in single crystal studies rather than the true co-ordination number N, because of the non-isotropic nature of the photoelectron wave[6]; N* reduces to N when studying polycrystalline or amorphous systems. For an l=0 to l=1 dipole allowed transition N* is given by:

$$N_i^* = 3 \sum_{j=1,\ N_i} \cos^2\theta_j , \qquad \text{Equation 2.4}$$

where θ_j is the angle between the electric field vector **E** and the vector $\mathbf{r}_{ij}$ which connects the central atom, a, to atom b as depicted in Figure 2.3. Equation 2.4 is

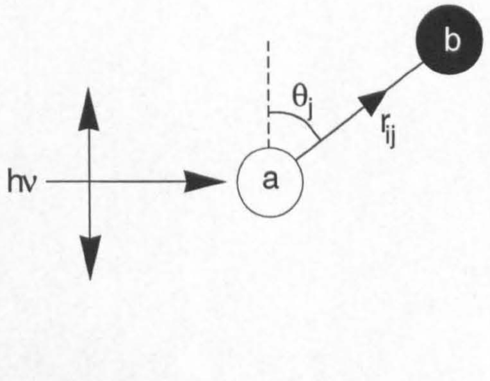

Figure 2.3 Illustration of the definition of θ_j, which is the angle between the electric field vector **E** and the vector $\mathbf{r}_{ij}$.

particularly useful in surface EXAFS studies of single crystals, since when it is coupled with the anisotropy and symmetry of a surface, along with the linear polarisation of synchrotron radiation it can aid adsorption site determination. The next term, $\phi(k)$, is the backscattering amplitude of an individual atom. This term depends upon the atomic potential of the backscattering atom, and thus is Z-dependent. Exp-$(2\sigma^2_i k^2)$, a Debye-Waller like term, accounts for the both the static disorder arising from imperfections in the crytsal and dynamic, thermal disorder of the system. Finally, the term $\exp(-2r_i/\lambda(k))$, in which l is the electron's mean free path, is used to describe the reduction in EXAFS amplitude arising from inelastic processes affecting the photoelectron.

As stated above, equation 2.2 is only applicable to scattering from a single shell of like atoms and therefore a more general form is required, in which the contributions from different scattering shells are accounted for by summing over all the different shells. This more general form is expressed thus:

$$\chi(k) = -\sum_i \frac{N_i^*}{kr_i^2} f_i(k)\, e^{-2\sigma_i^2 k^2} e^{2r_i/\lambda(k)} \sin(2kr_i+\phi_i(k)) \quad \text{Equation 2.5}$$

where $1/kr^2$ describes the decay in amplitude of the receding wavefront[7].

Equation 2.5 usually approximates rather well to experimentally observed EXAFS, but it must be borne in mind that several simplifying approximations have been made which may not always be valid. A brief discussion of these assumptions is now given. A more detailed analysis is to be found in the literature.[1]

Probably the most inadequate assumption made in the EXAFS formalism, as just described, is the approximation of the electron wave incident on the backscatterer to a plane wave. This approximation holds true only when the effective size of the backscattering atom is very small in comparison to the separation between it and the absorbing atom. At low k values, when the photoelectrons are less energetic, this approximation is not valid because the effective atom size is much greater and can be approximately equal to the interatomic distance. This increase in effective size occurs because a less energetic photoelectron penetrates less deeply into a scattering atom and is scattered by the more spatially diffuse valence electrons. Therefore a curved wave formalism is required if the information within this low k region is to extracted. Lee and Pendry formulated such a theory in 1976,[8] but it proved to be too computationally intensive. Gurman, Binsted and Ross[9] used an analytical averaging process to simplify the theory, in order to make the calculation more practicable. It is this simplified curved wave theory which provides the basis for the EXAFS analysis software EXCURV[10], which has been used to analyse all the EXAFS data in this thesis.

Secondly, the assumption that the EXAFS arises only from single scattering needs to be considered. Multiple scattering generally involves scattering through at least two angles close to 90° and a relatively long electron path. Usually the probability of this occurring at the relatively high electron energies of the EXAFS region is extremely low. This is because the probability of scattering through 90° is very small due to the scattering being very anisotropic (scattering at these energies is highly peaked in the forward direction, with a smaller backscattering probability and only a very small probability of scattering through 90°), and also because the mean free path of the electrons is quite short (not more than 2-3 times the interatomic distance at kinetic energies of 50 eV and greater). There is one geometry however where multiple scattering is important, and that is when a pair of atoms is colinear, or nearly colinear, with respect to the absorbing atom[7]. In this geometry the outer of the two atoms has an increased contribution to the scattering of the photoelectron due to the focusing of the electron wave by the potential of the intervening atom. This phenomenon is usually termed either shadowing or the focusing effect.

The assertion that a single scattering formalism is sufficient to describe the interactions of photoelectrons with kinetic energies > 40 eV in extended condensed media which contribute to EXAFS[1,11] is now being challenged as it has been shown that a significant improvement in fit quality can be obtained using a multiple scattering formalism for well ordered systems with high symmetry[12,13].

It is important, where possible, to account for both multiple and single scattering paths in cases of surface EXAFS with more than one post absorption edge oscillation in order to account for interference effects which may arise. However, the poor signal to noise ratios have limited attempts to establish the importance of multiple scattering at high Z K-edges. In C K-edge studies Baberschke's group have shown that MS is important.[14]

Multiple scattering is dependent upon the relative atomic positions of neighbouring atoms in several shells. Multiple scattering effects are therefore particularly sensitive to the stereochemical coordination of adsorbate atoms to the substrate. It is considered that the single scattering approximation is valid if the photoelectron wavelength, $\lambda = h/p = 2\pi/k$, is less than the interatomic distance, d, such that $k > 2\pi/d$.

A simplified treatment of multiple scattering arising from the K-edge EXAFS of

$$\chi(k) = -\sum_{i,j} \frac{3(\hat{\mathbf{e}}\cdot\hat{\mathbf{r}}_i)^2}{kr_i^2} |f_i(\pi)| \sin(2kr_i + 2\delta + \phi_i) - 6\frac{(\hat{\mathbf{e}}\cdot\hat{\mathbf{r}}_i)(\hat{\mathbf{e}}\cdot\hat{\mathbf{r}}_j)}{kr_i r_j r_{ij}} |f_i(\alpha_i)| |f_j(\alpha_j)| \sin$$

Equation 2.6

$$\left[k\left(r_i + r_j + r_{ij}\right) + 2\delta + \phi_i + \phi_j\right] - 3\frac{(\hat{\mathbf{e}}\cdot\hat{\mathbf{r}}_j)^2}{kr_j^2 r_{ij}^2} |f_i(\pi)| |f_j(\alpha_j)|^2 \sin\left[2k(r_j + r_{ij}) + 2\delta + \phi_i + 2\phi_j\right]$$

a three atom system is shown below.[15] A more complete treatment is given in reference 16:

In equation 2.6 the first term represents the single scattering contribution as in equation 2.3 and the second and third terms represent multiple scattering events. ϕ_i and δ are the phaseshifts due to scatterer and adsorber atoms at radius r_i. This treatment does not, however, include the effect of a finite photoelectron lifetime.

At long pathlengths multiple scattering may become more prevalent than single scattering photoelectron scattering paths, particularly in the case of favourable geometries such as adsorbate atoms which are near coplanar with substrate atoms.

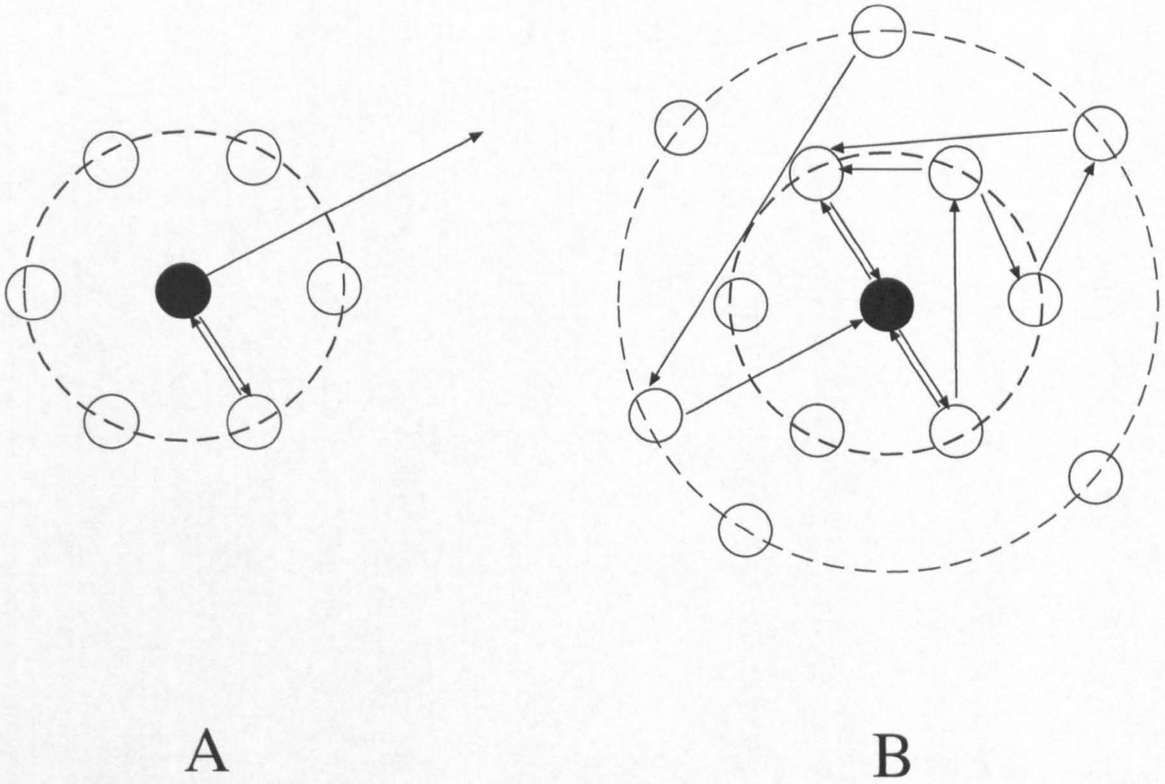

Figure 2.2 A) Single scattering process in EXAFS.
B) Multiple scattering processes responsible for XANES and contributions to EXAFS.

The treatment employed in this thesis is the full spherical theory including the small atom approximation to the polarisation dependent angle factor which breaks down only within about 30 eV of the absorption edge.[9] This was coupled with ab-initio calculated Hedin-Lundqvist potentials encompassing an energy dependent self-energy correction term[17].

Another assumption in equation 2.5 is that a system always exhibits Gaussian disorder. This is implicit in both the use of a Debye-Waller like type damping term and in the phase shift term. Again this assumption does not always hold true, and breaks down for atoms having large vibrational amplitudes, which can no longer be modelled using a simple parabolic approximation for their potential. To the lowest order, any such anharmonicity in the vibrational amplitude will manifest itself only in the phase and not in the amplitude of $\chi(k)$, and so an appropriate extra term is required only in the phase term of the EXAFS equation to avoid large errors in bond distance determination.[18]

Finally, equation 2.5 assumes that photoionisation is only into the primary channel. In other words it neglects many body channels such as shake-up, shake-off, and plasmon excitation. The outgoing photoelectrons resulting from these phenomena should also, in theory, suffer scattering and produce their own EXAFS, but fortunately their contributions to the EXAFS signal are not too significant. Shake-up processes are not important, because their cross section is too small to be detected in EXAFS. Shake-off and other processes have larger cross sections, but their large energy spread means that any EXAFS oscillations tend to be smeared out.[19] Thus almost exclusively it is the single electron channel which contributes to the EXAFS signal and these many body channels may be accounted for by merely introducing an amplitude reduction factor $S_0^2(k)$, which is dependent only on the type of absorbing atom[20].

Having discussed the merits of the various assumption made in equation 2.5, the final point which needs to be addressed is the importance of the phase shift term. As can seen from equation 2.5, accurate phase shift data are required to enable bond distances to be determined with any certainty. They may either be calculated or obtained from a suitable model compound. The use of model compounds for phase shift data is made possible because the phase shift of an element changes only slightly with chemical enviroment,[21] especially for photoelectron energies ≥ 100 eV, where the scattering is almost entirely from core electrons. Calculation of theoretical phase shift data is usually carried out by employing an *ab-initio* method developed by Lee and Beni.[19]

In summarising the above discussion one may conclude that EXAFS is an excellent technique for structural determination due to its elemental specificity and its reliance on short range order only. These attributes also mean that it is well suited to surface studies, especially adsorbate-substrate systems. Surface EXAFS (SEXAFS) measurements are, however, more exacting and generally more difficult to analyse, because the data ranges are usually shorter than for bulk measurements. This shortening of the data range arises from several sources. Firstly, the absorbing atom generally has a low atomic number and so there is a higher density of absorption edges, which can limit the data range. Secondly, the surface Debye temperature is often quite low, which gives rise to heavy damping of the EXAFS. In addition, surface bond distances are usually quite short leading to longer period EXAFS oscillations than is usual for bulk EXAFS. Lastly, the signal is weaker due to the reduction in the number of absorbers and sometimes scatterers, so that the EXAFS at higher k values may be obscured by experimental noise.

2.2.2 NEXAFS

The physics of the NEXAFS region is somewhat different to that of the EXAFS region. Firstly, although equation 2.1, which was used to describe a photoinduced electronic transition in the EXAFS region, may also be used to the describe the same process in the NEXAFS regime, the final state description must be changed. In the EXAFS region the electron is excited into a continuum state, whereas in the NEXAFS region the electronic excitation is into low-lying extended states, which arise from bonding interactions, and so these details need to be incorporated into the final state. Also, unlike EXAFS, the electrons suffer multiple scattering due to both the isotropic nature of the electron-atom scattering at these lower energies and the lengthening of the electron's mean free path; multiple scattering becomes progressively more important within the NEXAFS region as the absorption edge is approached. Therefore the NEXAFS region of an absorption spectrum is a far richer seam of information than the EXAFS region with more details about both the geometric and the electronic structure of the environment to be mined. For example, not only radial distances, but also the orientations of molecules with respect to the surface can be extracted from NEXAFS data.

The multiple scattering suffered by the photoelectrons in the NEXAFS region usually means that data analysis is rather more demanding in this region than in the EXAFS region. However, this is not always so and it is now generally accepted that most of the features in the NEXAFS spectrum of a simple molecular adsorbate can be analysed in a relatively straightforward manner without relying on cumbersome multiple scattering calculations. This is because the NEXAFS is dominated by excitations into the bound, or quasi-bound, electronic states of the molecule and not by excitation into the more delocalised states of the substrate.[15] However in the case of metals the core hole is well screened by the conduction electrons in the valence band and no bound states are present. Due to variation in the density of states near the Fermi energy, E_F, structure occurs within ±10 eV of the edge and this is separate from XANES and is known as XAMES, X-ray Absorption Main Edge Structure.[11] This, along with the chemical shift of the absorption edge, gives information concerning the oxidation state and interactions between metallic adsorbate atoms and the substrate.

The chemical shift of absorption edges is due to the tighter binding of core levels due to the change in effective nuclear charge associated with the valence electrons participating in bond formation and also the onset of an energy gap associated with the transition from, in the case of metals, a screened metallic form to a chemical compound. In general in the case of metals this shift is to the higher energy side of the absorption edge increasing in line with the increasing valence state of the cation formed. This effect can be masked by a high degree of covalent nature in the bonds formed, the shared nature of the covalent electrons screening the core hole.

References

1. Chemical Analysis Vol. 92 - X-ray Absorption: Principles, Applications, Techniques of EXAFS, SEXAFS and XANES, Eds. D.C. Koningsberger and R. Prins (John Wiley & Sons, 1988).

2. H. Fricke, Phys. Rev., **16**, 202, (1920); G. Hertz, Z. Phys., **3**,19, (1920); B.B. Ray, Z. Phys., **55**, 119, (1929)

3. R. de L. Kronig, Z. Phys., **70**, 317, (1931); R. de L. Kronig, Z. Phys., **75**, 190, (1932)

4. D.E. Sayers, E.A. Stern, and F.W. Lytle, Phys. Rev. Lett., **27**, 1204, (1971)

5. E.A. Stern, Phys. Rev. B, **10**, 3027, (1974); P.A. Lee, and J.B. Pendry, Phys. Rev. B, **11**, 2795, (1975); C.A. Ashley, and S. Doniach, Phys. Rev. B, **11**, 1279, (1975)

6. P.A. Lee, Phys. Rev. B, **13**, 5261, (1976)

7. Inorganic Chemistry Concepts 9 - EXAFS: Basic Principles and Data Analysis, B.K. Teo (Springer-Verlag, 1986)

8. P.A. Lee, and J.B. Pendry, Phys. Rev. B, **11**, 2795, (1975)

9. S.J. Gurman, N. Binsted, and I. Ross J. Phys. C, **17**, 143, (1984)

10. N. Binsted, J.W. Campbell, S.J. Gurman, and P.C. Stephenson, SERC Daresbury Laboratory EXCURV90 Program (1990)- EXCURV92 was also used.

11. B.K. Argawal, "X-Ray Spectroscopy", (Springer-Verlag, Berlin, 1991)

12. D. Arvanitis, K. Baberschke and L. Wenzel, Phys. Rev. B, **37**, 7143, (1988)

13. S.P. Harte, S. Vinton, R. Lindsay, L. Håkansson, C.A. Muryn, G. Thornton, V.R. Dhanak, A.W. Robinson, N. Binsted, D. Norman and D.A. Fischer, Surf. Sci. Lett., **380**, L463, (1997)

14. P.H. Citrin, J. Phys. (Paris) Colloq., **47**, C8-437, (1986)

15. J.J. Boland, S.E. Crane, J.B. Baldescwieler, J. Chme. Phys., **77**, 142, (1982)

16. L. Fonda, J. Phys.: Condens. Matter, **4**, 8269, (1992)

17. L. Hedin and S. Lundqvist, Solid State Phys., **23**, 1, (1969)

18. P. Eisenberger, and G.S. Brown, Solid State Comm., **29**, 481, (1979)

19. P.A. Lee, and G. Beni, Phys. Rev. B, **15**, 2862, (1977)

20. E.A. Stern, B.A. Bunker, and S.M. Heald, Phys. Rev. B, **21**, 5521, (1980)

21. P.H. Citrin, P. Eisenberger, and B.M. Kincaid, Phys. Rev. Lett., **36**, 1346, (1976)

22. J. Stöhr, K. Baberschke, R. Jaeger, R. Treichler, and S. Brennan, Phys. Rev. Lett., **47**, 381, (1981)

Chapter 3

Instrumentation

3.1 Introduction

This chapter contains a description of the equipment used to carry out the experiments described in later chapters. The equipment is associated with surface EXAFS experiments carried out at the Synchrotron Radiation Source (SRS), Daresbury Laboratory. A description of the sample characterisation techniques is also given, along with a description of the beam line used, namely the double crystal monochromator IRCSS Beamline 4.2.

3.2 The IRC NEXAFS Chamber

The equipment used to carry out the experiments actually comprises of two chambers; a beam monitor (I_0) instrument as well as the main experimental chamber. Both UHV chambers were constructed by Vacuum Science Workshop (VSW). The role of the I_0 chamber is extremely important for normalisation in the investigation of adsorbates on single crystals using SEXAFS. A schematic of the chamber is shown in Figure 3.1.

3.2.1 Vacuum Techniques

In order to achieve the UHV conditions necessary for these experiments, the chamber was pumped down from atmospheric pressure in a manner which put as small a loading as possible on each of the pumps. The requirement for UHV is of great importance in the study of Cr and Ti K-edge SEXAFS because of the great reactivity of these elements to water, oxygen and carbonaceous species.

The chamber was initially pumped down using an oil free carbon vane pump, which reduced the pressure to 2/3 bar. A liquid nitrogen cooled sorption pump

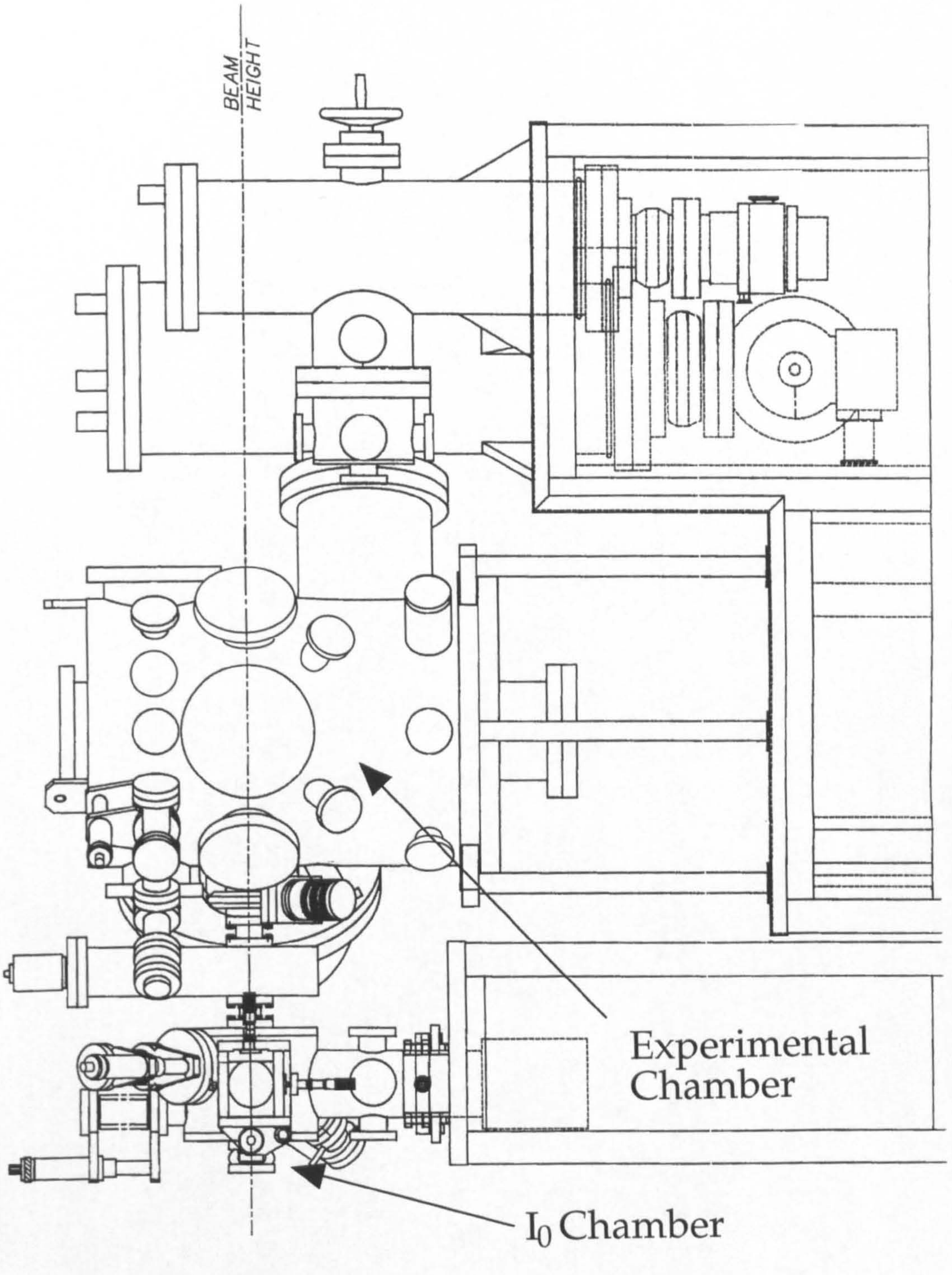

Figure 3.1 Side view of IRCSS NEXAFS chamber

was then used to reduce the pressure to approx. 1 x 10^{-3} mbar. The final pump down was achieved using 160 l/s and 510 l/s turbomolecular pumps, and ion pumps. The whole chamber can be baked, a typical bake being ~180° for 12 hours, resulting in a chamber pressure of 2 x 10^{-10} mbar.

3.2.2 Level 1

The upper level of the chamber in is shown in detail in Fig. 3.2. It contained :

(1) Omicron rear-view LEED optics for Low Energy Electron Diffraction,

(2) an AS10 or Phi ion gun for sample cleaning,

(3) a ME10 microevaporator metal source,

(4) a VG Quadrupole mass spectrometer (200 amu).

3.2.3 Level 2

The second level shown in detail in Figure 3.3 is the region in which the experiments are carried out. This contained :

(1) a HA 100 Electron energy analyser,

(2) a VSW EG5 electron gun,

(3) a liquid nitrogen cooled titanium sublimation pump, alternatively liquid nitrogen cooled Cr sources,

(4) a Ti filament source,

(5) EG&G 3 channel solid state fluorescence detector, or,

(6) Single wire gas proportional counter.

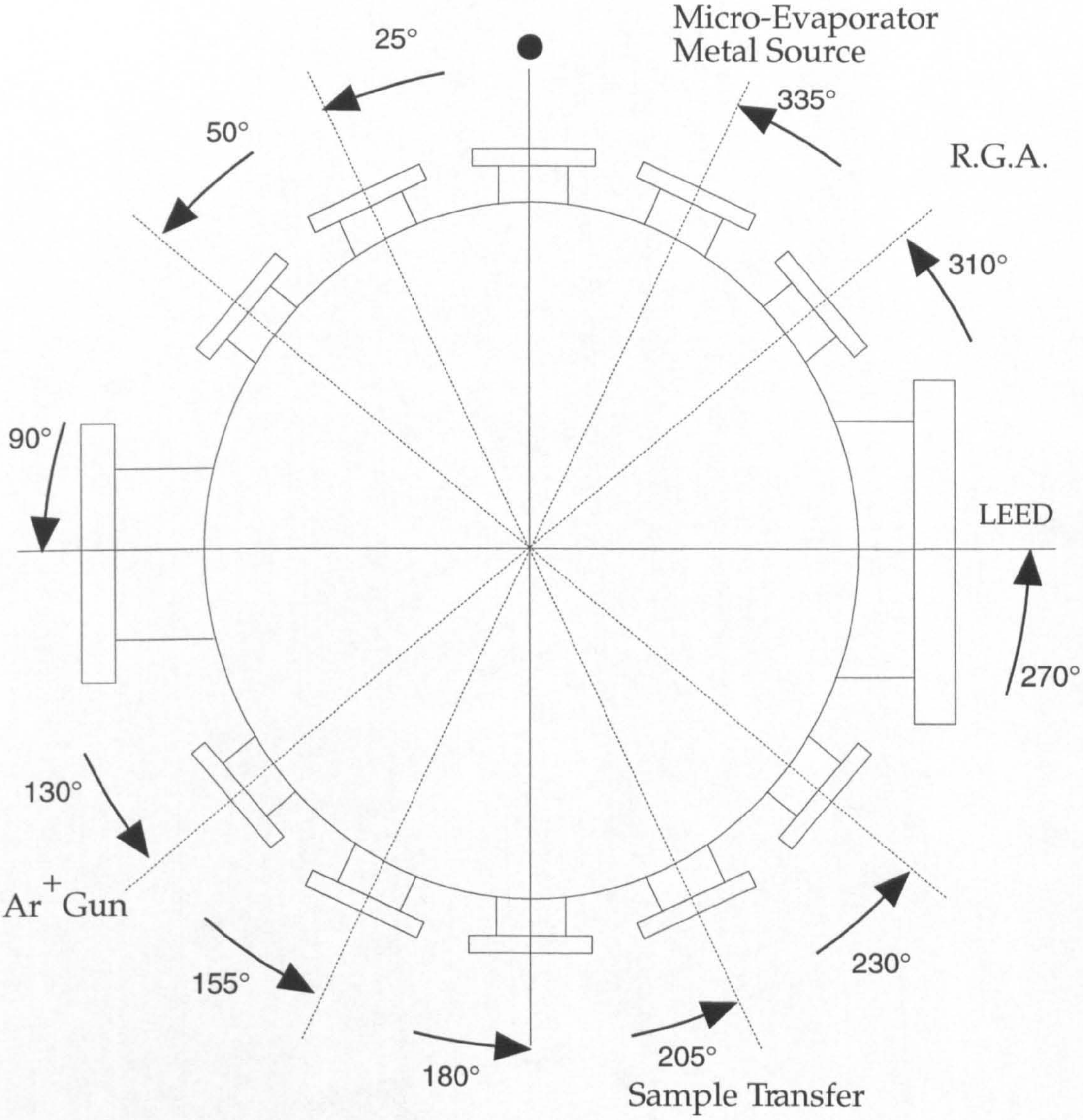

Figure 3.2 A schematic diagram of the upper level of the chamber in which sample preparation was carried out. (Scale = 1:5)

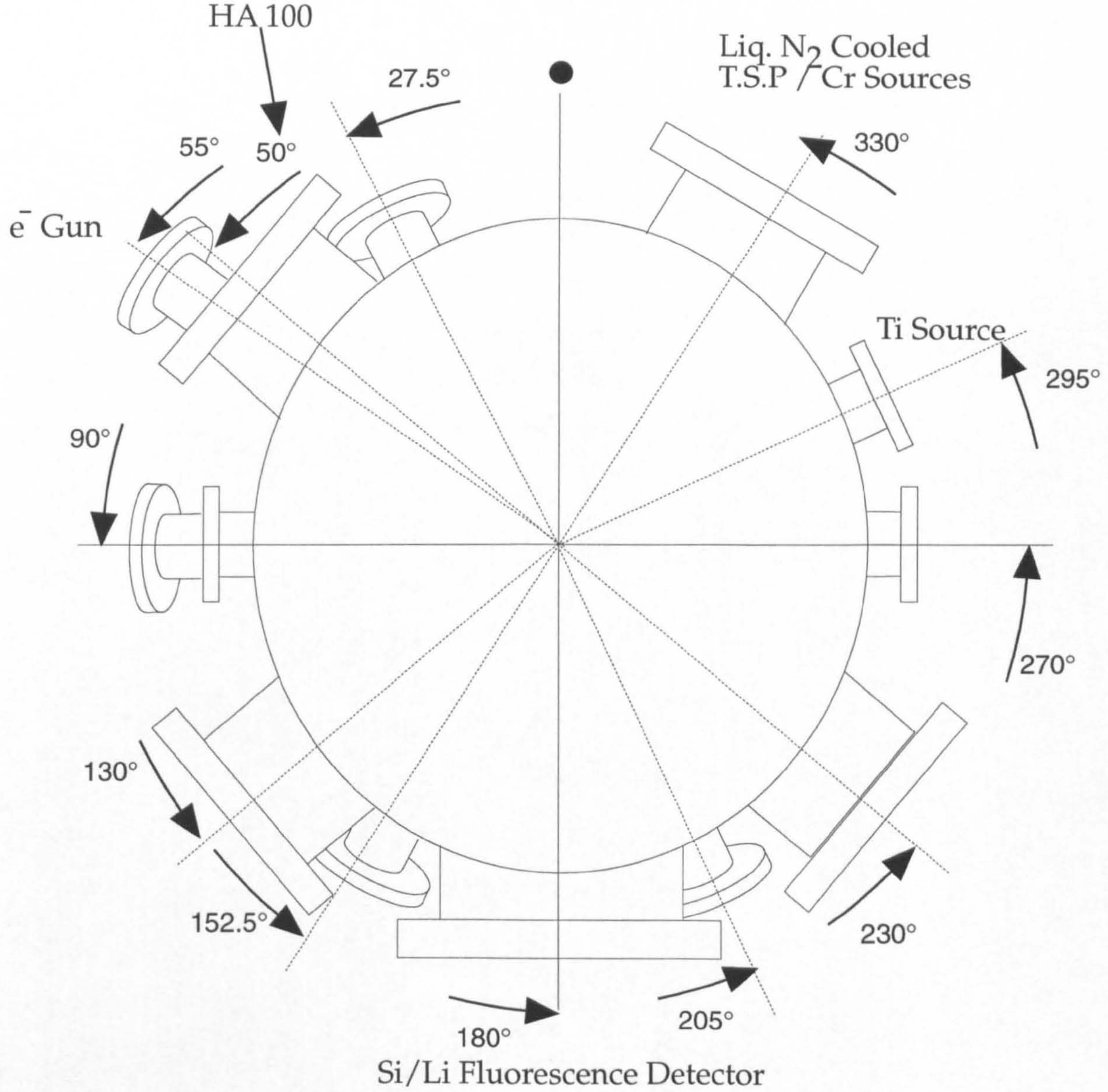

Figure 3.3 A schematic diagram of the middle/experimental level of the chamber. (Scale = 1:5)

3.3 Sample Manipulation

The samples used were mounted on a VG Omniax sample manipulator, which is inserted via an eight inch port at the top of the chamber. This allowed for the sample to be rotated in the plane of the synchrotron, i.e. the polar angle, and also allowed the azimuthal angle to be varied, i.e. the plane perpendicular to the that of the synchrotron. The sample was mounted on a sample plate which had the possibility of being heated by filaments at the back of the sample plate. A positive voltage could also be applied to the isolated sample plate. This enabled electron beam bombardment sample heating to high temperatures although this was not used in these experiments as it resulted in a degradation of surface quality. The sample plate also had a reservoir thermally attached, but electrically isolated, which could be filled with liquid nitrogen, thus allowing the sample to be cooled to ~ 90 - 100 K.

3.3.1 Sample Transfer

The sample transfer system consisted of a standard magnetically coupled transfer arm with 700 mm travel, a 40 mm x 20 mm molybdenum backplate and a sample plate as shown in Figure 3.4. The transfer arm was attached to a four way cross. On the orthogonal axis to the transfer arm a pumping hose to a 160 l/s turbomolecular pump and a loading port consisting of an FC38 windowed port with a Viton gasket were mounted. This pumping array achieved a base pressure better than 5×10^{-7} mbar, resulting in a main chamber pressure of less than 5×10^{-9} mbar during sample transfer.

The main chamber required only approximately 30-60 mins to return to base pressure. The transfer plate located in a space in a collar on the end of the transfer arm by the tab seen in Figure 3.4.

The sample was mounted horizontally on the transfer plate by the use of tantalum clips which located in a recess lying 0.5 mm below the sample surface along two sides of the sample. This allowed the synchrotron beam an uninterrupted path to the sample surface in both grazing and normal incidences.

The transfer plate is located on the backplate by tantalum clips overlying a 0.5 mm recessed area within the transfer plate. This allows movement in all planes normally associated with the use of an Omniax or HPLT crystal manipulator.

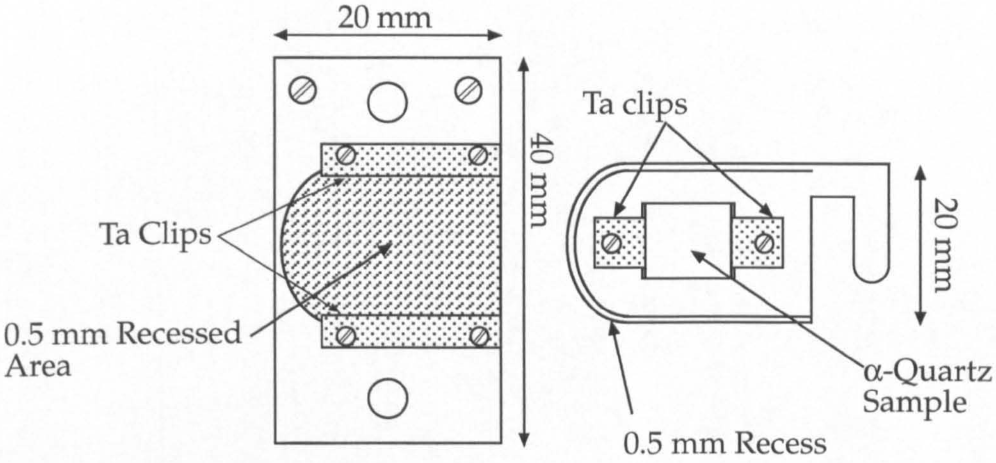

Figure 3.4 Transfer plate and backplate

3.4 Sample Characterisation

Sample cleanliness was investigated in all cases using Auger electron spectroscopy (AES),[1] which employed 3 keV electrons from the EG5 electron gun. Surface order was checked using LEED.[1] The surface sensitivity of AES comes from the short mean free path of electrons in a solid, typically < 20 Å for electrons of kinetic energy between 10 to 2000 eV.[2]

One of the disadvantages of using AES with such a powerful electron source, however, is that there is a distinct possibility that beam damage may occur.

Indeed this has been previously observed for high electron fluxes incident upon α-quartz surfaces[3] and therefore the use of AES was kept to a minimum.

LEED was used throughout, as previously mentioned, as a purely routine check on the surface order. A diagram of the setup used is shown in Fig. 3.5, and consists of a four grid system, with a LaB_6 filament in the integral electron gun. There is a problem with using such a filament when gases are introduced into the chamber, as the filament tends to be poisoned. The transfer width of the low energy electron beam is approximately 100 Å, and thus the surface needs to be ordered over such distances before a clear diffraction pattern can be observed.[1] The diameter of the electron beam is of the order of 0.5 mm. Hence, the diffraction pattern arises from scattering from the various domains on the surface. A detailed multiple scattering analysis is required if a full structural determination is to be carried out using LEED, and this can be time consuming. Electron beam damage is also an issue with LEED. Even though the energy used is comparatively low, the LEED pattern was seen to degrade with time.

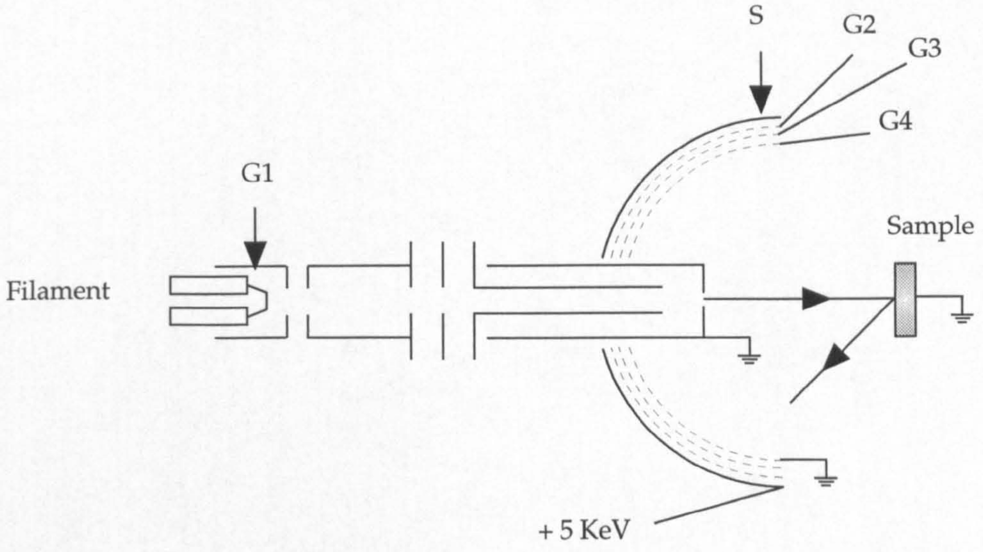

Figure 3.5 A schematic diagram of the low energy electron diffraction setup. The incident electron beam is provided by the electron gun and backscattered electrons are imaged on the

screen S after passing through grids G.

3.5 Metal Dosers

3.5.1 VSW ME10 Microevaporator

The ME10 microevaporator was utilised for the evaporation of a collimated beam of Ti atoms onto the quartz substrate. As shown in Figure 3.6, the microevaporator consists of a coiled 0.15 mm tungsten filament mounted approximately 3 mm distant from the tip of a positively biased 1.0 mm diameter Ti wire. The thermionic emission of electrons from the tungsten filament results in electron beam heating of the of the Ti wire causing the evaporation of atomic Ti.

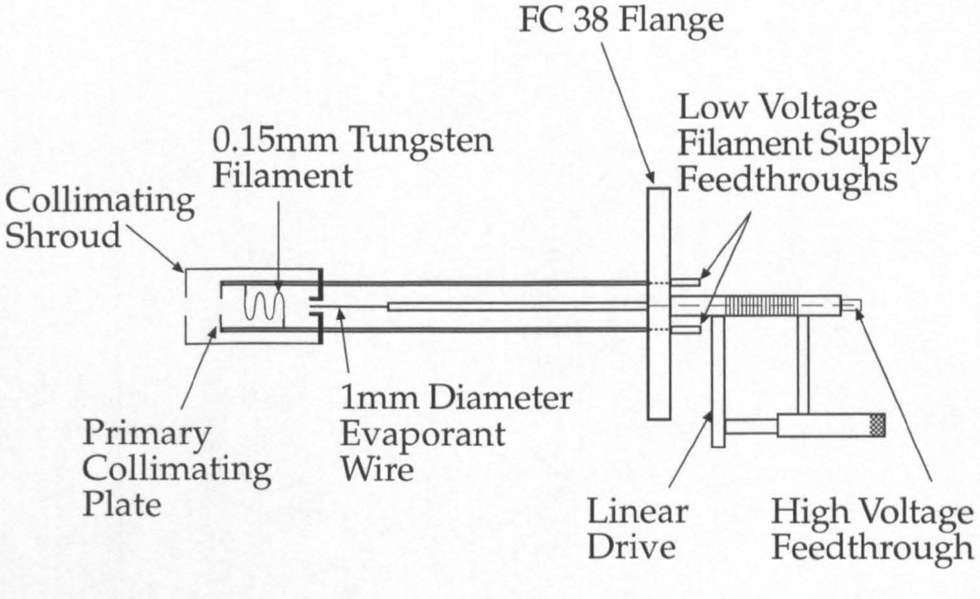

Figure 3.6 VSW ME10 Microevaporator

The input power is maintained at a constant level by use of a feedback circuit within the control unit. Typical operating conditions were 12.5 mA emission current and 1.25 kV bias voltage yielding a power density of 15.625 W/mm^2. The microevaporator was initially degassed by use of an internal degas programme and subsequently by the application of an emission current of approximately 6 mA at 1 kV whilst no deposition was carried out.[4] The two stage collimation system, shown in Figure 3.6, produced a 10 mm diameter beam at a distance of 60 mm from the second, outer shroud collimator. This doser could not be utilised for the dosing of chromium due to the difficulties associated with machining wire and rods from chromium.

3.5.2 Titanium Filament

This was a resistively heated titanium filament approximately 2 mm in diameter mounted in a liquid nitrogen cooling jacket in order to reduce outgassing to a minimum during operation. This doser was not collimated and resulted in the global dosing of the sample and its immediate environs. Typical operating conditions were 35 A at 12 V for approximately 10 s. Degassing consisted of the passing of 40 A through the filament for 10 s.

The maximum pressure observed during operation of this filament source was 5×10^{-10} mbar, rising to 8×10^{-10} mbar during degassing.

3.5.3 Electrodeposited Cr Source

A high purity Cr evaporator was fabricated via the electrodeposition of Cr onto a clean 0.25 mm tungsten wire bent into a hairpin shape from an alkaline solution of CrO_3.[5] Electroplating was carried out using a Pb anode and the W wire as cathode. A current of 45 mA and a voltage of 3 V were used, the current corresponding to a current density at the wire of the order of 10^4 Am^{-2}. Electroplating for 18 hours resulted in the deposition of approximately 75 mg onto a 0.25 mm W wire.

The sources were mounted on a standard low voltage three pin FC38 feedthrough within a liquid nitrogen cooled jacket in order to minimise outgassing into the chamber. The source was initially degassed at 5 A prior to bakeout of the vacuum system in order to remove any water incorporated into the source during fabrication. A second degassing cycle, again at 5 A, was carried out during the bakeout procedure. During deposition the sources were run at a current of 7 A and the base pressure of the chamber was not observed to increase above the base pressure of 2×10^{-10} mbar.

Following deposition only Cr, Si and O could be detected in AES spectra.

3.6 Fluorescence Detectors

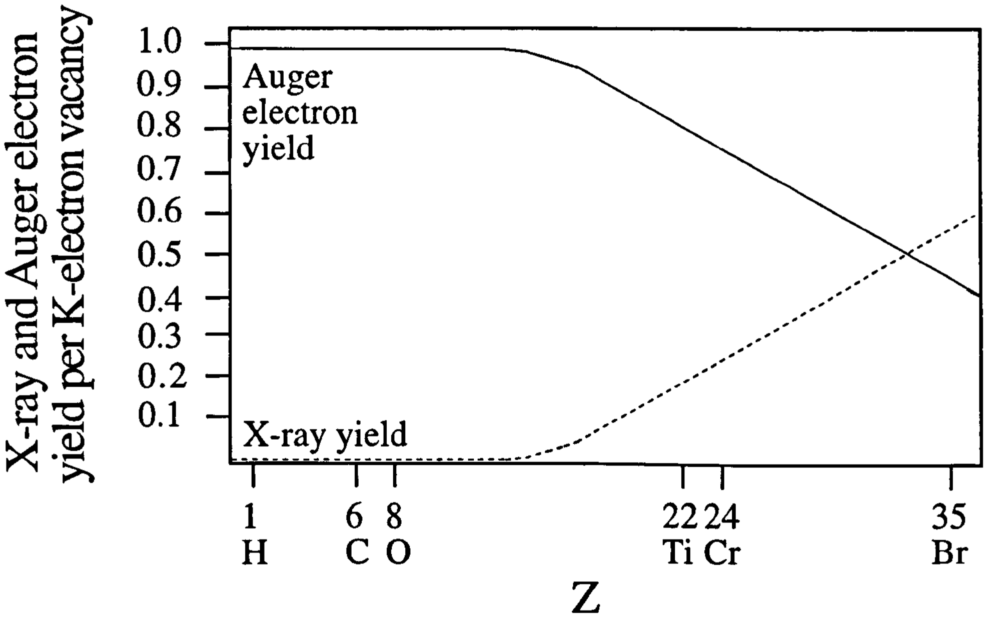

Figure 3.7 Relative cross sections of X-ray fluorescence yield and Auger electron yield for K shell ionisation as a function of Z.[6]

In surface X-ray absorption experiments the decay of the core hole is monitored rather than X-ray transmission. This involves detecting Auger electrons or fluorescent photons.

The use of a fluorescence detection scheme is necessitated by the large band gap of silicon dioxide. This results in sample charging rendering the use of electron detection schemes inappropriate. Figure 3.7 shows the relative fluorescence and Auger electron yields for a range of atom types, chromium and titanium being highlighted. This shows the preponderance of Auger electron emission over fluorescent photon emission for low Z atom types. Despite the relatively low cross-section, fluorescence detection can still be the method of choice because of the insensitivity to charging and high signal to background level.[7]

3.6.1 Gas Proportional Counter

This detector was utilised for the collection of the c(2x2)S-Ni(110) data presented in Chapter 6 of this thesis.[8] The detector is a gas flow proportional counter mounted on a reentrant flange assembly in the horizontal plane perpendicular to the synchrotron beam as shown in Figure 3.8. The supported 0.125 mm Be window is 50 mm in diameter allowing the collection of a solid angle of 0.4π sr.

The Be window acts to prevent the detector gas, P10 (10% CH_4 in Ar mixture), which is continuously flowing through the detector at slightly over atmospheric pressure from entering the U.H.V. chamber.

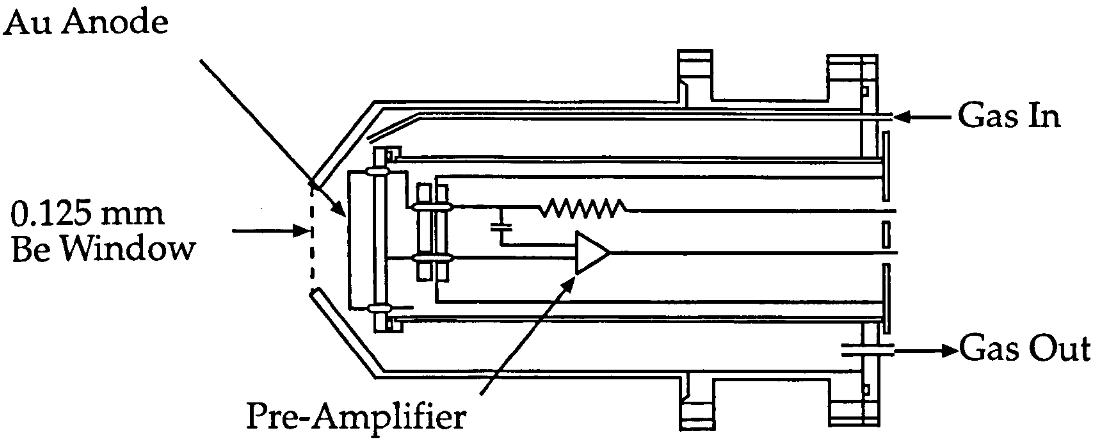

Figure 3.8 Single Wire Gas Proportional Counter

X-rays passing through the Be window ionise the counter gas, electrons being multiplied by impact ionisation due to the electric field of the gold anode wire. The standard operating conditions have the Au wire at +1.5kV bias. The resulting pulse of electron charge is collected at the anode wire and amplified by a charge sensitive preamplifier. The adsorbate fluorescence can be discriminated from bulk or contaminant fluorescence using a timing single channel analyser. The energy resolution of the analyser is ~1 keV at the S K-edge, which does not allow the resolution of the elastically scattered light peak from the adsorbate signal. However Ni Kα arising from Ni 1s ionisation by third order light could readily be discriminated out from the adsorbate signal.

3.6.2 Solid State Si-Li Detector

The 3 channel lithium drifted silicon X-ray fluorescence detector used in recording of all

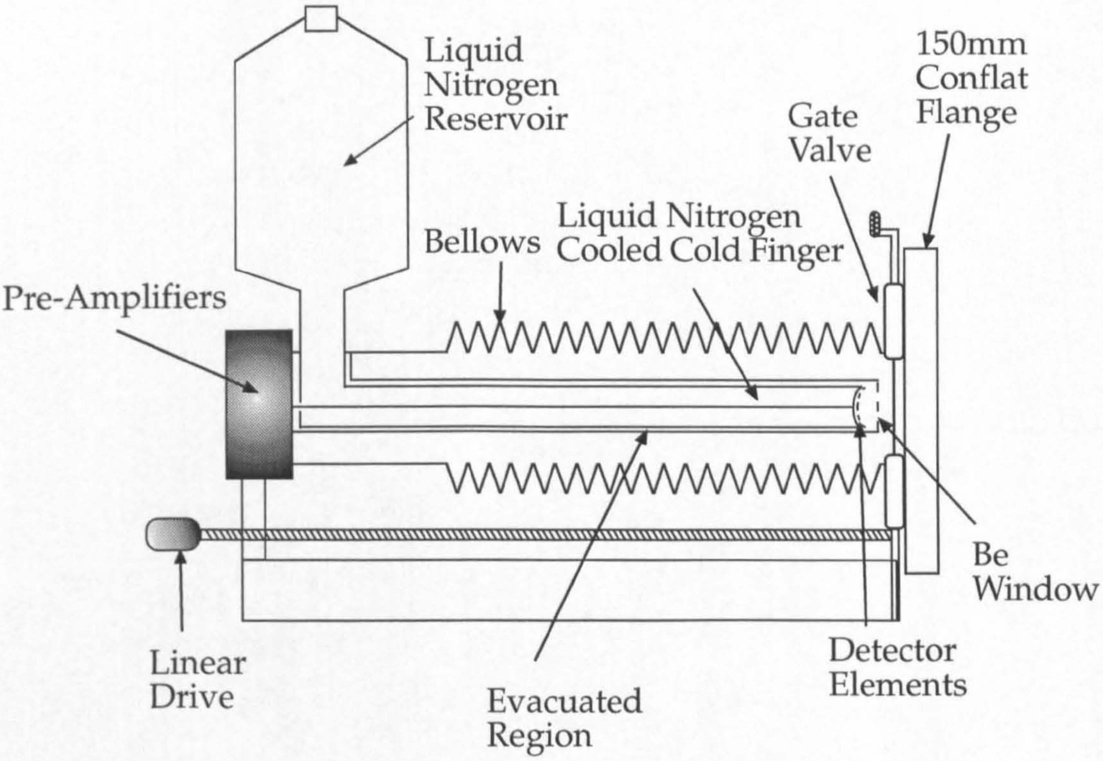

Figure 3.9 Schematic of EG&G 3 Channel Solid State Fluorescence Detector

titanium and chromium surface EXAFS data presented in this thesis is shown schematically in Figure 3.9. The 25 mm thick Be window serves to attenuate low energy substrate fluorescence and is 15 mm in diameter. The p-i-n junction is formed by the diffusion of Li into a p-type single crystal of silicon. The lithium serves to compensate charge due to impurities in the silicon single crystal thus increasing the intrinsic layer in which X-rays form electron-hole pairs. Upon the application of a negative bias (-400 V) the charge carriers generated by an incident photon are swept to the electrodes before recombination can occur. This is shown in Figure 3.10. The detector is operated at liquid nitrogen temperatures (~77 K) in order to reduce the mobility of the lithium ions.

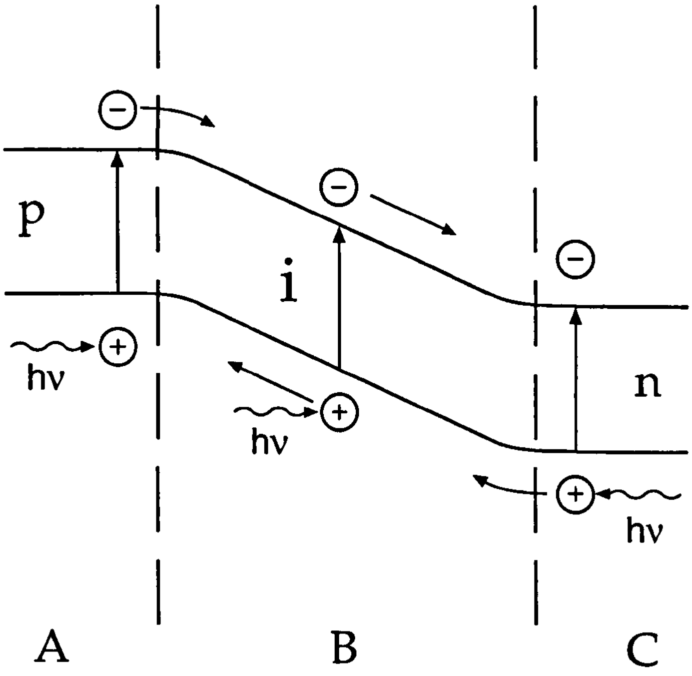

Figure 3.10 p-i-n Junction Energy Band Diagram Under Reverse Bias **A:** Electron Diffusion **B:** Drift Space **C:** Hole Diffusion

The number of electron-hole pairs generated is :[9]

$$n = \frac{E_v}{V_i'} \qquad \text{Equation 3.1}$$

E_n is the photon energy in eV,

V_i is the intrinsic bandgap of Si (3.8 eV),

n = 1309 at the Ti K-edge (4976 eV) and n = 1577 at the Cr K-edge (5996 eV)

The electrons are swept to the positive terminal where the total charge collected is:

$Q = n\, q_{e,}$ Equation 3.2

where $q_e = 1.6 \times 10^{-19}$ C,

This terminal is connected to a preamplifier where the charge, Q, is stored in a capacitor, C_f, so the resulting pulse has an amplitude of :

$$V_0 = \frac{Q}{C_f} = \frac{q_e\, E_v}{V_i\, C_f}. \qquad \text{Equation 3.3}$$

The resolution of the Si(Li) detector is given by :

$$\frac{\Delta E}{E_v} \sim \frac{FWHM}{E_v} \qquad \text{Equation 3.4}$$

where the full width half maximum, FWHM, of the peak is given by :

$$FWHM = \left\{ \sigma^2{}_{Noise} + \left[2.35 (F\, E_v\, V_i)^{\frac{1}{2}} \right]^2 \right\}^{\frac{1}{2}} \quad . \qquad \text{Equation 3.5}$$

s_{Noise} represents a degradation of the resolution due to preamplifier noise. Thus the theoretical resolution at the Ti K-edge, assuming zero preamplifier noise, is 85 eV and similarly at the Cr K-edge is 93 eV.

3.7 The SRS Daresbury Laboratory

The advantage of utilising a synchrotron for surface science experiments lies in the benefits which can had from a tunable, plane polarised, high intensity source of photons. The fact that all three of these desirable features can be exploited, which has been taken advantage of over the past two decades, leading to a wealth of science.

3.7.1 Synchrotron Radiation

Synchrotron radiation is the electromagnetic radiation produced by charged particles moving at relativistic velocities in a circular path.[10-12] This radiation represents the main energy loss mechanism for particles so constrained. Even for non-relativistic velocities the radiation is highly directional in the plane of rotation, as shown in Figure 3.11.

The radiated power of relativistic charged particles is inversely proportional to the fourth power of the particle mass, leading to the use of electrons in synchrotron radiation storage rings. The basic components of a synchrotron radiation source are a number of dipole magnets to bend the electron beam along a circular trajectory and therefore to act as the basic source of radiation.[12] These magnets are separated by straight sections in which are located numerous components, including multi-pole electron beam focusing magnets, wiggler insertion devices and undulators. Radio frequency cavities are used to

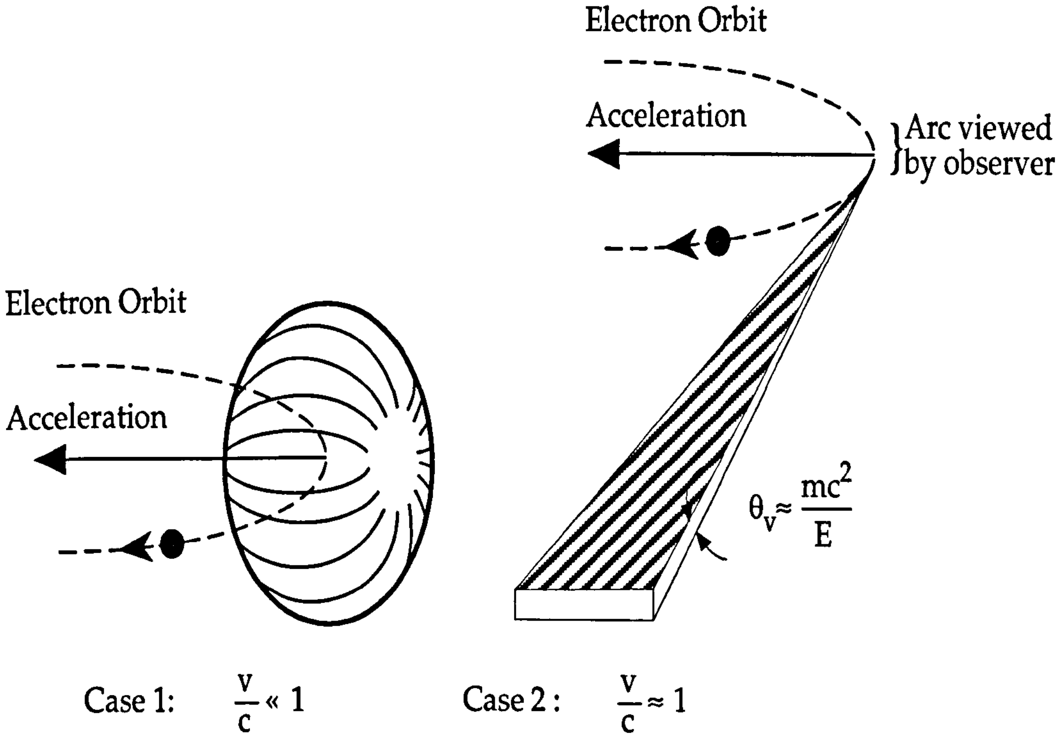

Figure 3.11 Radiation emission pattern of electrons in circular motion. Case 1, non-relativistic electrons. Case 2, relativistic electrons.[10]

accelerate the electron beam to the required energy (if necessary) and to make up the energy lost due to emission of synchrotron radiation. These devices generate an electric field parallel to the beam orbit alternating in polarity, usually sinusoidally at high frequency, typically in the range 50 - 500 MHz.[12] The electrons stored in such a magnetic lattice form into bunches; 160 bunches in the case of the SRS in multi-bunch mode. This effectively means that an observer only sees light whenever a bunch passes an observation window, giving synchrotron radiation a well defined pulsed time structure. At the SRS a pulse is seen every 2 ns in multibunch mode.

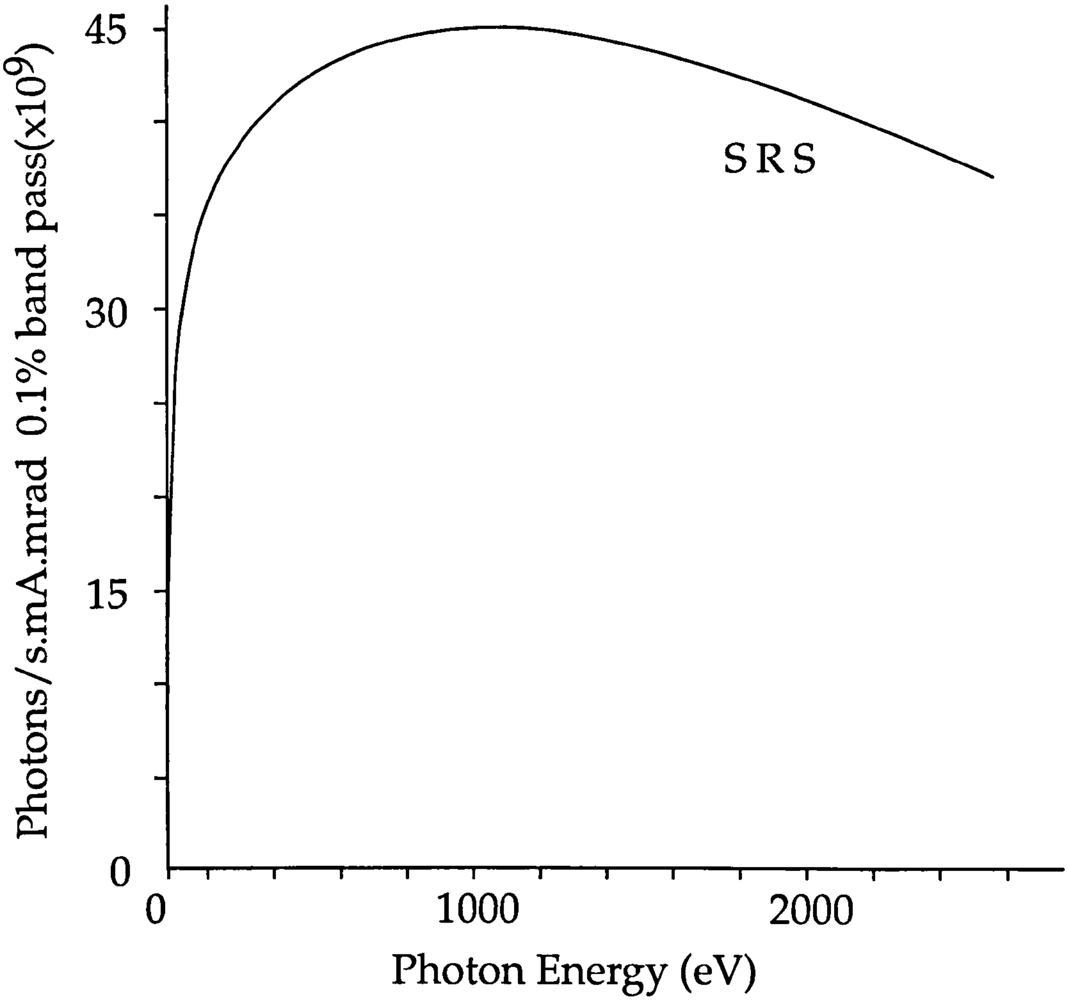

Figure 3.12 Vertically integrated photon flux from the Daresbury SRS as a function of photon energy (0.1% bandwidth).

The characteristics of the particular source depend on its operating energy, bending magnet radius, the stored current and the magnetic fields involved. The SRS typically runs at 2 GeV, with stored current of ca. 300 mA. The electromagnetic radiation so produced covers the energy range from the infrared to hard X-rays; the intensity distribution from the SRS is shown in Fig. 3.12.[11]

The photon energy range of importance for the Surface EXAFS experiments to be described are 2400 - 6200 eV. Hence the following discussion will be concerned with the double crystal monochromator designed for these photon energy ranges. Before discussing the monochromators, some of the special properties of synchrotron radiation can be summarised as:[10]

1. Wide spectral range;
2. Polarised;
3. High intensity;
4. Collimated in the vertical plane (hence small spot size can be achieved);
5. UHV compatible (since the storage ring itself is at UHV) and
6. Pulsed (feature not used in these experiments).

3.7.2 Beamline 4.2

A schematic layout of the beamline is shown in Figure 3.13. The premirror system consists of a plane mirror followed by a sagittal cylindrical mirror. They are placed close together at a distance of 12.5 and 13.5 m, respectively, from the SRS tangent point.[14] These mirrors are in a (+1, -1) configuration and are arranged to have the same fixed angle of incidence, 89.55°, so that the exit beam lies in the horizontal plane. The functions of the mirrors are decoupled. The first mirror takes the heat load, while the second mirror serves to focus the beam horizontally onto the sample. The plane mirror is made from Herasil and has an

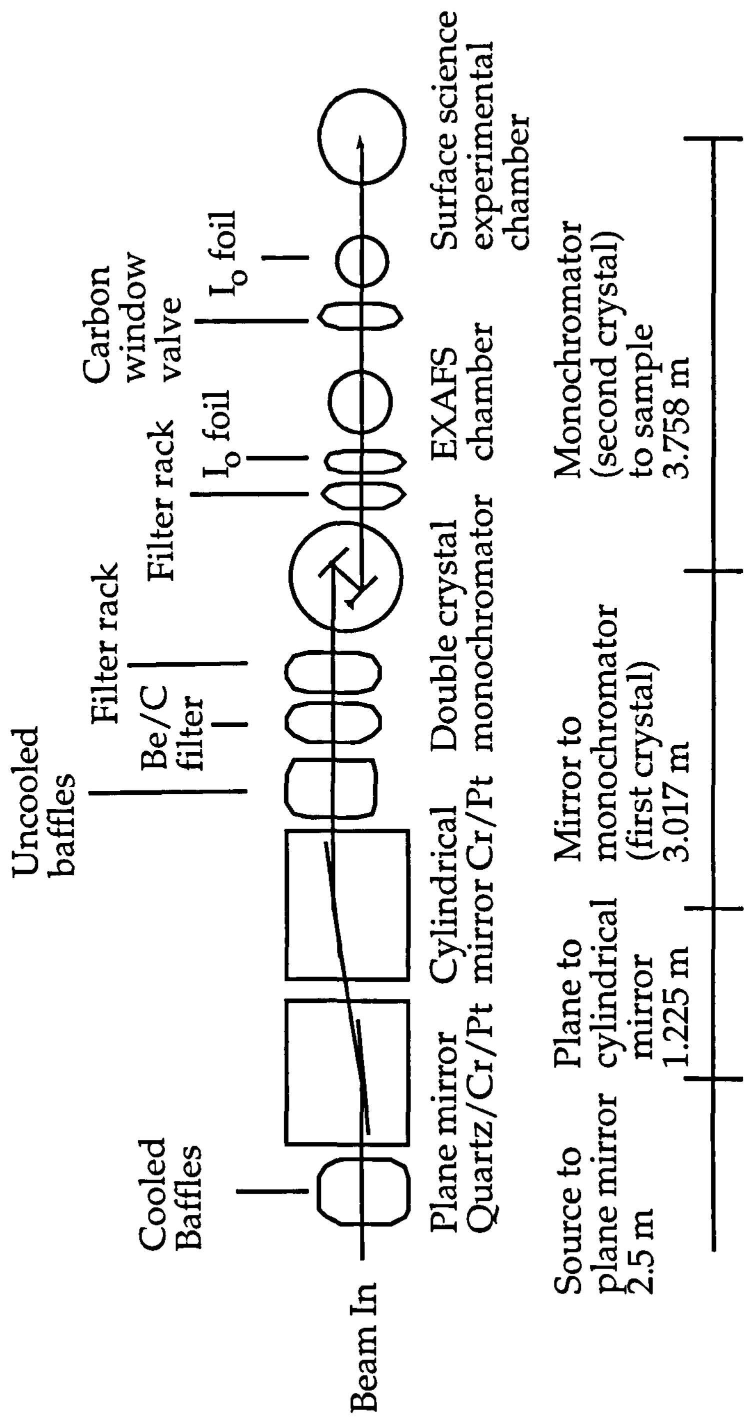

Figure 3.13 Schematic Diagram of IRCSS Beamline 4.2

optical surface of size 800 x 160 mm, with three reflective surfaces available in the shape of stripes along the length of the mirror. These consist of a 80 mm width of quartz and 40 mm width each of Pt and Cr. The mirror surface can be selected *in situ* by mechanical translation of the mirror. The cylindrical mirror has an optical surface of size 800 x 42 mm coated in two equal stripes of Pt and Cr. The metal coatings on the two mirrors allows for higher order rejection.[14] Its sagittal radius is 7.07 cm, giving a 2:1 demagnification onto the sample. The mirror mount incorporates an *in situ* bending mechanism to change the meridian radius. A meridian radius of 1146 m gives a stigmatically focused beam, while a radius of 3438 m gives a parallel exit beam. This allows the convergence onto the monochromator to be varied and thus a selection of two different resolution/spot size modes.[14] Baffles in the beamline allow selection of the reflective surface of the cylindrical mirror.

The double crystal monochromator was manufactured by Bird and Tole, Ltd. The photon energy range is spanned by rotation of the first crystal while the second crystal rotates and translates, keeping the beam position fixed. These movements are made by a drive mechanism that is coupled to a single ex-vacuum stepper motor. The Bragg angular range of the monochromator is 14° to 76°. In addition to the main drive, two other *in situ* adjustments of the first crystal are possible, using in-vacuum stepper motors. These are "pitch" about the rotation axis to rock on to the Bragg peak, and a "roll" adjustment in the direction normal to the beam. The roll of the second crystal can be adjusted in the same manner.

The two roll adjustments are required to ensure that the two crystals remain parallel during the photon energy scan, otherwise there can be a considerable horizontal tracking of the exit beam as function of photon energy. In practice, it has been found that to obtain a stationary exit beam requires a one time adjustment of the two roll movements when a photon energy range is selected for a particular experiment. Subsequently, no routine adjustment of roll is required during the experimental run.

The pitch adjustment is made by maximising the drain current signal from a 2.5 μm thick aluminium foil in the beam monitor (I_0) section immediately after the monochromator. It has been found necessary to maximise this signal at the start of a photon energy scan and subsequent use of computer controlled adjustment of pitch, using a feedback current from the I_0 foil to the stepper motor, at each discrete photon energy within a scan has proved essential in the acquisition of SEXAFS data.

With a Ge(111) crystal pair in the monochromator, the resolution of the beamline at 2500 eV is ~1 eV, with a photon flux of 1.5×10^{11} photons/sec/100 mA. The resolution at 5000 eV is approximately 2.4 eV and increases only marginally at 6000 eV when using Ge(111) crystal pairing.[15] The spot size with the full beam is 2 mm (vertical) by 4 mm (horizontal), which may be reduced by using baffles in the beamline. Different crystal pairs (Ge(111), InSb(111), Ge(220), Si(111) and Quartz$(10\bar{1}0)$) are available to vary the usable energy range and provide higher resolution. Using a combination of the mirror coatings and monochromator crystal pairs, the beamline is specified to operate in the energy range 640 eV < hv < 10 keV. The experiment described in chapter 6 utilises the spectral region above the S K-edge (2470 eV). For these experiments situation, the plane mirror was laterally translated to illuminate the uncoated quartz strip, and baffles were used to allow light only from the Cr coating of the second mirror into the monochromator. A pair of Ge(111) Bragg reflectors was installed in the monochromator. This combination allowed operation of the monochromator with little higher-order content in the output. The cylindrical mirror was not focused in the meridian direction so that a beam parallel in the dispersive direction was incident on the entrance slit of the monochromator. The experiments described in chapters 4 and 5 (4950 eV - 6400 eV) utilised the quartz strip of the plane mirror coupled with the platinum strip of the second mirror, again utilising the Ge(111) monochromator crystal pairing. This monochromator crystal pairing results in an increased flux but poorer resolution than the Ge(220) pairing which was available for this energy range.

References

1. D.P. Woodruff and T.A. Delchar, "Modern Techniques Of Surface Science", (Cambridge University Press, 1992)

2. M.P. Seah and W.A. Dench, Surface Interface Analysis, **1**, 2.

3. F. Bart, M. Gautier, F. Jollet and J.P. Duraud, Surf. Sci., **306**, 342, (1994)

4. Vacuum Science Workshops, "ME10 Operating Manual", Manchester, U.K..

5. J.J. McClelland, J. Unguris, R.E. Schollen and D.T. Pierce JVST A, **11**, 2863, (1993)

6. K. Siegbahn, C. Nordling, A. Fahlman, R. Nordberg, K. Hamrin, J. Hedman, G. Johansson, T. Bergmark, S.E. Karlsson, I. Lindgren and B. Lindberg, "ESCA: Atomic, Molecular and Solid State Structure Studied by Means of Electron Spectroscopy", (Almqvist and Wiksells Boktryckeri AB, Sweden, 1965)

7. J. Stöhr in "Chemical Analysis Vol. 92, 'X-ray Absorption - Principles, Applicatons, Techniques of EXAFS, SEXAFS and XANES'", Eds. D.C. Koningsberger and R. Prins, (Wiley Interscience, John Wiley and Sons Inc., London, 1988)

8. D.A. Fischer and C.Y.Yang, Nucl. Instrum. Methods A, **291**, 123, (1990)

9. B.K. Agarwal "X-Ray Spectroscopy", (Springer Verlag, Berlin, 1991)

10. H. Winick, in "Synchrotron Radiation Research" ed. H. Winick and S. Doniach, (Plenum Press, New York, 1980).

11. C. Kunz ed., "Synchrotron Radiation", (Springer-Verlag, Berlin, 1979).

12. R.P. Walker, Daresbury Laboratory Preprint No. DL/SCI/P513A.

13. J.B. West and H.A. Padmore, "Optical Engineering, Handbook of Synchrotron Radiation" Vol 2 (North-Holland Publishing, 1988).

14. A.W. Robinson, S D'Addato, V.R. Dhanak, P. Finetti and G. Thornton, Rev. Sci. Instrum., **66**, 1769, (1995)

15. V.R. Dhanak, Personal Communication.

Chapter 4

A SEXAFS study of α-quartz $(0001)\left(\sqrt{84}\times\sqrt{84}\right)R11^{\circ}$- Cr

4.1 INTRODUCTION

The metal - oxide interface of chromium has invoked interest due to the potential importance of the system in areas as diverse as the formation of novel CMOS structures,[1,2] formation of magnetic multilayers[3,4] and heterogeneous catalysis, the latter involving a strong metal support interaction.[5,6] This interest in the nature of these interfaces encompasses a wide range of phenomena from the nature of bonding in the interfacial region and the effect of further metal deposition to the electronic structure of the interface and its departure from those of the bulk, either substrate or adsorbate. The Cr / SiO_2 system has particular relevance as an idealised model system for a range of important ethene - polythene conversion catalysts.[7,8] EXAFS, the technique employed here, has successfully been used in the study of highly dispersed metal and zeolite catalysts for many years.[9-13]

The present study, an investigation of the effect of reactive metal adsorption upon a single crystal silicon dioxide substrate, follows from the systematic investigation of the growth of a wide range of metals upon TiO_2 (110)14-19, copper deposition upon α-alumina (0001) surfaces[20] and Ag upon MgO (100).[21,22]

A previous study of Cr adsorption upon TiO_2 (110) has evidenced the formation of a quasi two dimensional growth mode of Cr upon this substrate due to a surface wetting effect.[16] Studies have been carried out of metal adsorption upon single crystal surfaces of alumina and titania but not upon true single crystal surfaces of silica.[23]

Adsorption of metals upon silicon dioxide has until now been limited to studies carried out upon thin oxide films thermally grown upon single crystal silicon wafers[24,25] or cleaved polycrystalline glass samples.[26] This is due to the difficulties in applying electron spectroscopies[27] to bulk silicon dioxide arising from the highly insulating nature of the substrate, the bulk band gap being approximately 9.0 eV.[28] This problem is, however, circumvented in SEXAFS measurements of the local structure by the use of fluorescence yield detection. This is the method employed here. The (0001) surface of α-quartz has two known stable terminations,[29] the (1x1) unreconstructed surface and also $(\sqrt{84}\mathrm{x}\sqrt{84})\,\mathrm{R}11^{\circ}$ reconstruction. This reconstruction is thought to be due to the effect of Dauphiné twin domains resulting from an incommensurate phase at the surface upon cooling through the β - α phase transition.[29-31]

4.2 EXPERIMENT

Experiments were performed in an UHV chamber, base pressure below $2\mathrm{x}10^{-10}$ mbar, equipped with a VSW HA 100 MCD hemispherical analyser, VSW EG5 electron gun, Omicron rearview LEED for sample characterisation, VG Micromass 200 quadrupole mass spectrometer for residual gas analysis and sample transfer system. (See Section 3.3.1)

Chromium K-edge (5989 eV) SEXAFS measurements were performed using a Ge(111) crystal pair in the double-crystal monochromator of station 4.2 at the SRS, Daresbury Laboratory. (See Section 3.7.2)[32]

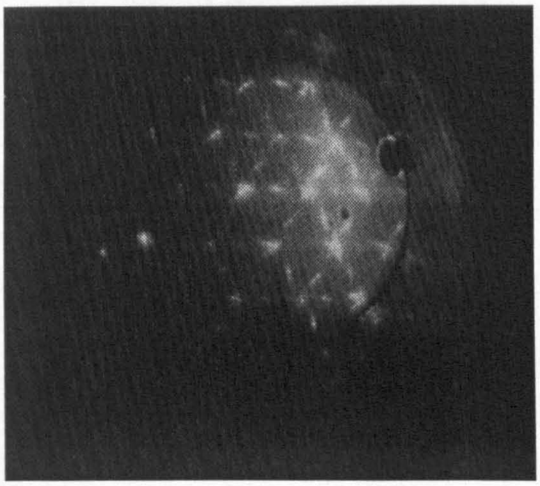

Figure 4.1 LEED Pattern of a clean α-quartz (0001) $(\sqrt{84}\mathrm{x}\sqrt{84})\,\mathrm{R}11^{\circ}$ reconstructed surface. Primary beam energy 63 eV.

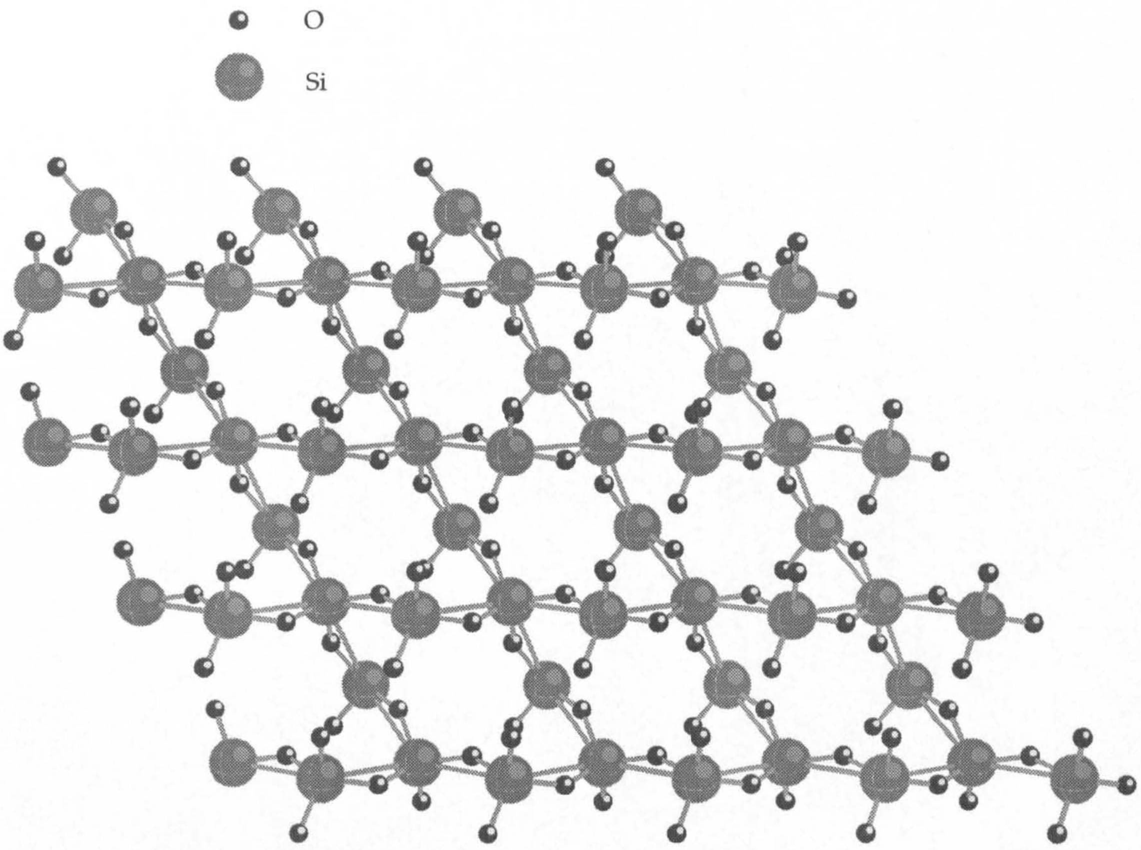

Figure 4.2 Idealised surface net for α-quartz (0001) (1x1) surface

An EG&G 3 channel lithium drifted silicon solid state fluorescence detector, (See Section 3.6.2), was used to record the Cr Kα fluorescence yield as a monitor of the surface X-ray absorption coefficient. Normalisation of the surface EXAFS data to the incident photon flux was accomplished by measuring the drain current from a thin Al foil placed between the monochromator and sample chamber. Surface EXAFS and XANES spectra were recorded at ambient temperature, 298K, with the **E** vector in the $[10\bar{1}0]$ azimuthal direction in both near normal, $\theta_i = 20^o$, and near grazing, $\theta_i = 70^o$, angles of incidence.

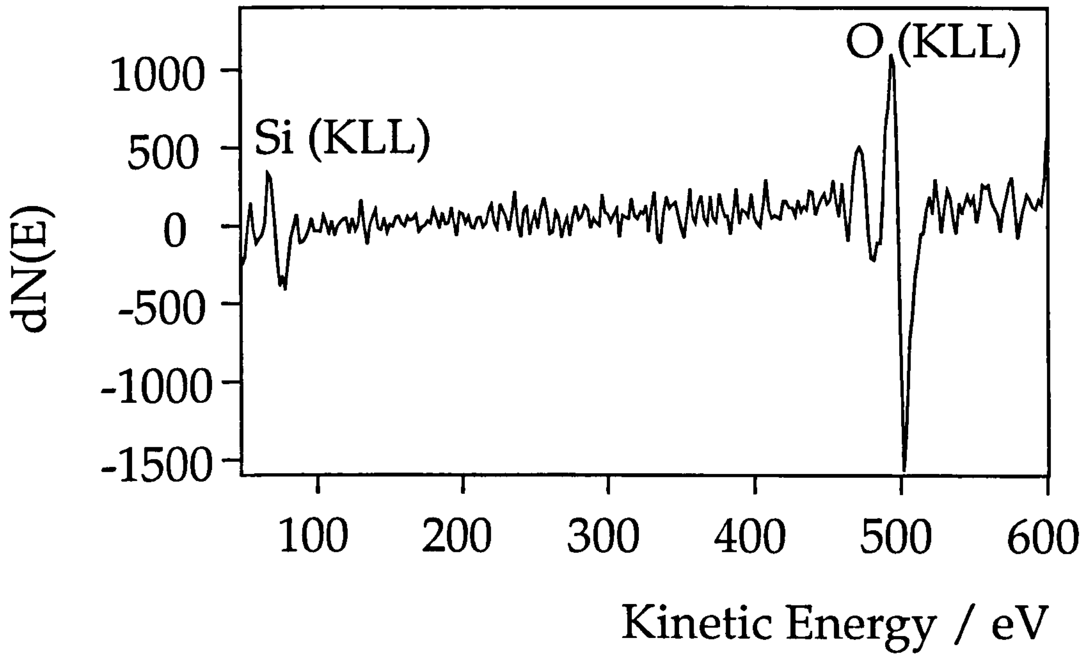

Figure 4.3 Auger electron spectrum from an as prepared α-quartz $(0001)(\sqrt{84}\times\sqrt{84})$ R11° surface. (Primary beam energy 3 keV, normal emission.)

The α-quartz sample (Pi-Kem) was polished to within 0.3° of the (0001) plane as determined by Laue diffraction. The $(\sqrt{84}\times\sqrt{84})$ R11° reconstruction was formed by an etch in 2% HF followed by ex-situ annealing of the sample to 900°C for 3 hours in air, then allowing the sample to cool to 350°C and transferring to UHV whilst still above 200°C.[29] Surface order and cleanliness were checked via LEED. A typical LEED pattern is shown in Figure 4.1, and an Auger spectrum from a freshly prepared α-quartz $(0001)(\sqrt{84}\text{x}\sqrt{84})\text{R}11^\circ$ surface is shown in Figure 4.3. These measurements were made at the edge of the sample in order to minimise electron beam damage to the surface area to be investigated.[33]

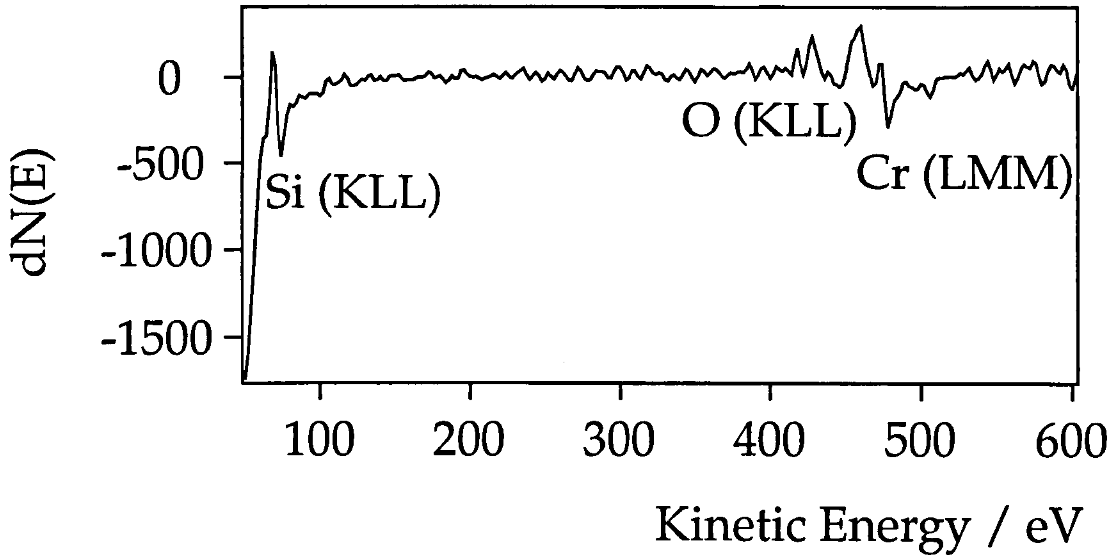

Figure 4.4 Auger electron spectrum from 0.25 ML Cr (assuming dispersed Cr) deposited upon an α-quartz $(0001)(\sqrt{84}\text{x}\sqrt{84})\text{R}11^\circ$ surface. (Primary beam energy 3 keV, normal emission.) Displacement of Cr and O features is due to dynamic sample charging.

Vapour deposition of chromium was achieved via evaporation of chromium electrodeposited upon a resistively heated tungsten wire.[34] During evaporation the pressure in the chamber was observed to increase to a maximum of $7\text{x}10^{-10}$ mbar. Prior to metal deposition the substrate fluorescences were monitored to ensure the substrate was free of chromium. Nominal chromium coverages were estimated from the ratios of the O(KLL) and Cr(LMM) Auger signals at 0.25 ML. Figure 4.4 shows the AES at 0.25 ML Cr coverage. Following correlation of the AES and edge steps at 0.25±0.08 ML, higher coverages were estimated from the Cr K-edge step. The Cr and O Auger signals were chosen to derive coverages due to their similar energies as this would result in similar behaviour under sample charging. This again was an attempt to minimise the known effects of electron beam damage on the SiO_2 surface. The surface cleanliness was checked again at the end of each set of measurements and coverages recalculated in order to check for oxygen and carbon contamination during data acquisition.

Background subtraction of the SEXAFS data was performed using the Daresbury Laboratory EXBACK programme and a single scattering fitting procedure used a new single scattering variant of the EXCURV92 code[35,36] which allows simultaneous fitting of both normal incidence and grazing incidence spectra in comparison to a previously constructed model, leading to a self-consistent array of fitting parameters. The refinement procedure exploits, where applicable, the crystallographic symmetry of the data to increase the determinacy of the fitting parameters.[37] This new code utilises full spherical wave theory, in which the small atom approximation to the polarisation-dependent angle factor breaks down only within about 15 eV of the edge [38,39] and also ab-initio derived phaseshifts using Hedin-Lundqvist potentials.[40]

4.3 RESULTS

To investigate the nature of the growth mode of Cr upon single crystal α-quartz (0001) surfaces a series of fluorescence yield Surface EXAFS measurements were performed at a range of chromium coverages from 0.25 ML to 1.0 ML, the raw data being shown in Figure 4.5. Fluorescence yield SEXAFS is particularly useful as it is insensitive to the effects of sample charging[27] which is likely to be exacerbated in this case by the formation of a surface capacitance upon metal adsorption.[41] It is also highly surface specific for the case of adsorption of a non-substrate atom type upon the substrate and also allows the detection of coverages below the level detectable by Auger electron spectroscopy due to the excellent signal-background ratio.[42]

Data analysis made use of the bulk EXAFS Cr spectrum, shown in Figure 4.6. This was recorded at 298K, using Station 8.4 at the SRS Daresbury by Dr. J.F.W. Mosselmans. The coordination numbers of the four shells utilised in the fit were

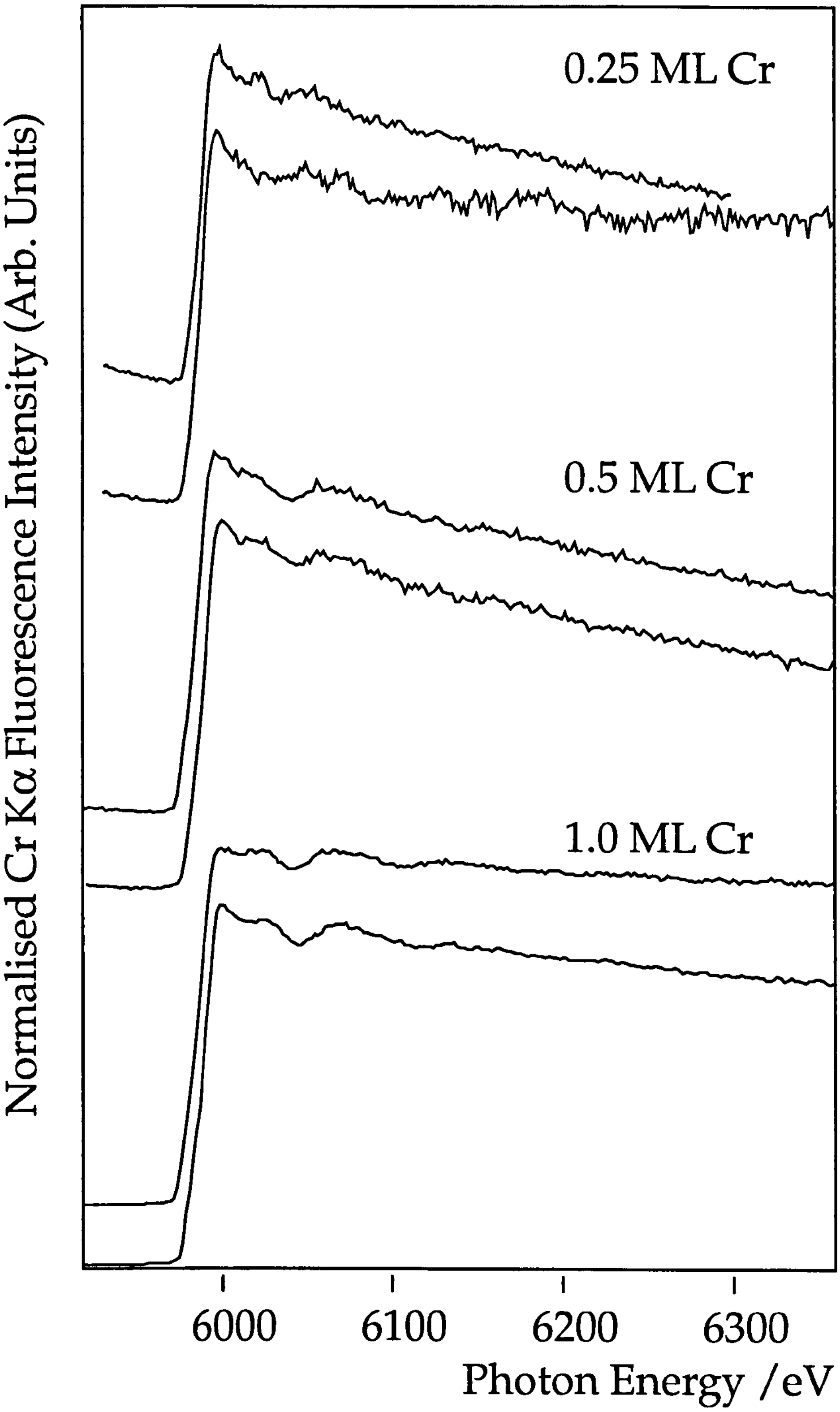

Figure 4.5 Cr K-edge surface EXAFS data recorded from the α-quartz (0001) $(\sqrt{84}\times\sqrt{84})$ R11° reconstruction at 298 Kwith the E vector parallel to the $[10\bar{1}0]$ azimuth with both 70° incidence angle (upper line) and 20° incidence angle (lower line). Coverages are as indicated. The data are normalised between coverages at 6040 eV.

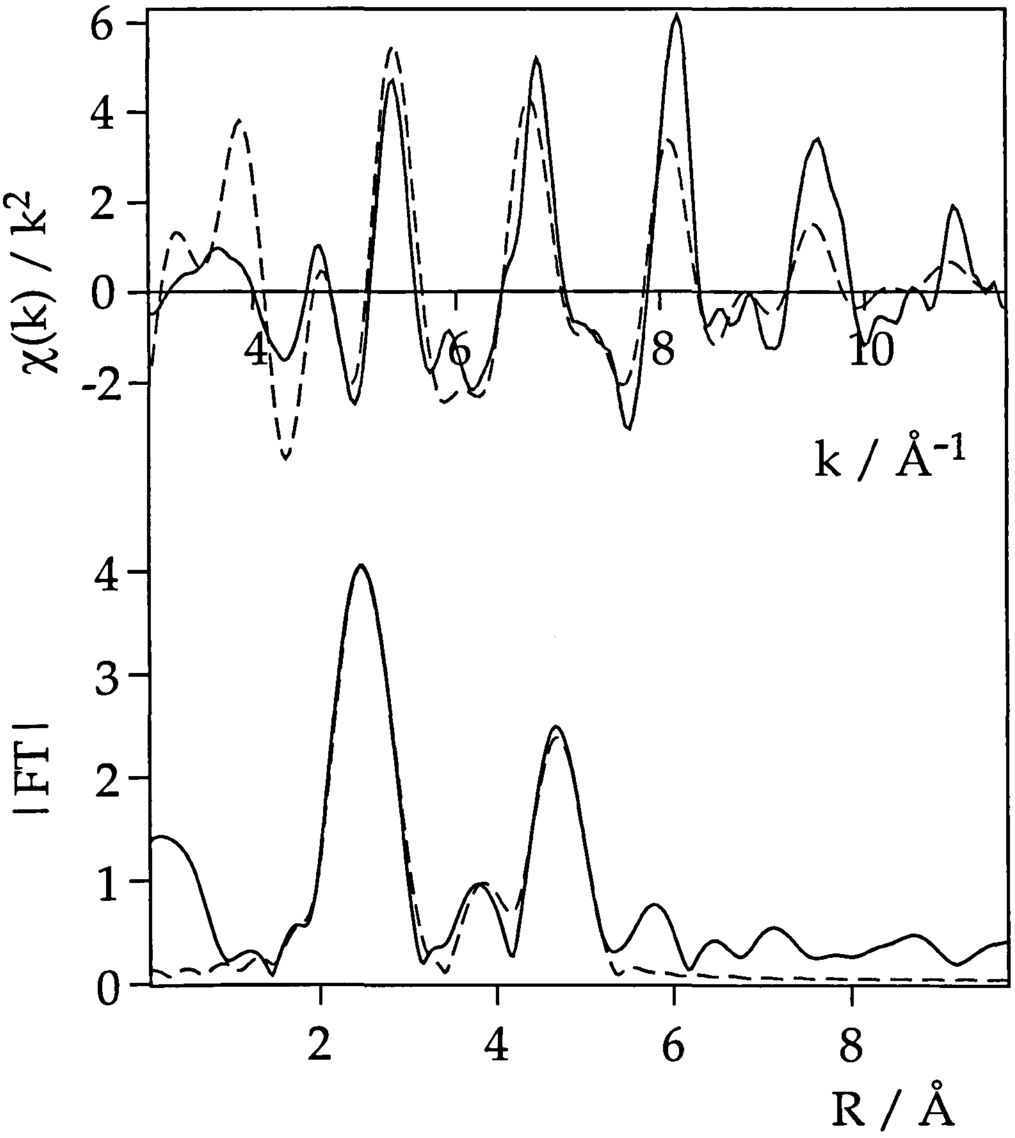

Figure 4.6 Cr K-edge bulk EXAFS spectrum and corresponding Fourier transform at 298 K after background subtraction conversion to k space and weighting to k^2. The experimental data (solid line) is compared to the best fit theoretical calculation (broken line) of a model containing the four nearest neighbour coordination spheres.

set to those of bulk Cr and the radial distances varying at most by only 0.01 Å from the bulk values. This allowed the initial values of the Fermi energy correction to the E_F value derived in background subtraction and also Debye-Waller like factors and other correlated factors known to affect the amplitude of the EXAFS such as the lifetime of the photoelectron and many body effects to be derived.[42]

In analysis of the surface EXAFS only structural parameters such as coordination number (in the case of randomly oriented sub-nanometric models) and the radial distances of coordination spheres were utilised as variables in the analysis procedure. This does however neglect the large degree of anharmonicity in the motion of atoms in small particles which can result in derived coordination numbers which are significantly less than the actual values.[43,44] The exclusion of the Debye-Waller like factor from the analysis is based upon the assumption that static and thermal disorder are comparable for all spectra. This assumption if wrong will lead to errors in the calculated coordination numbers.

Coverage	Coordination Number ±0.2	Radius / Å ±0.03 Å	R-factor
0.25 ML	1.4 0.6	2.37 2.86	75
0.5 ML	1.2 0.7	2.35 2.90	78
1.0 ML	1.2 0.7	2.37 2.86	69

Table 4.1 Best fit parameters and R-factors of theoretical models. Quoted errors are derived from EXCURVE programme.[33,34]

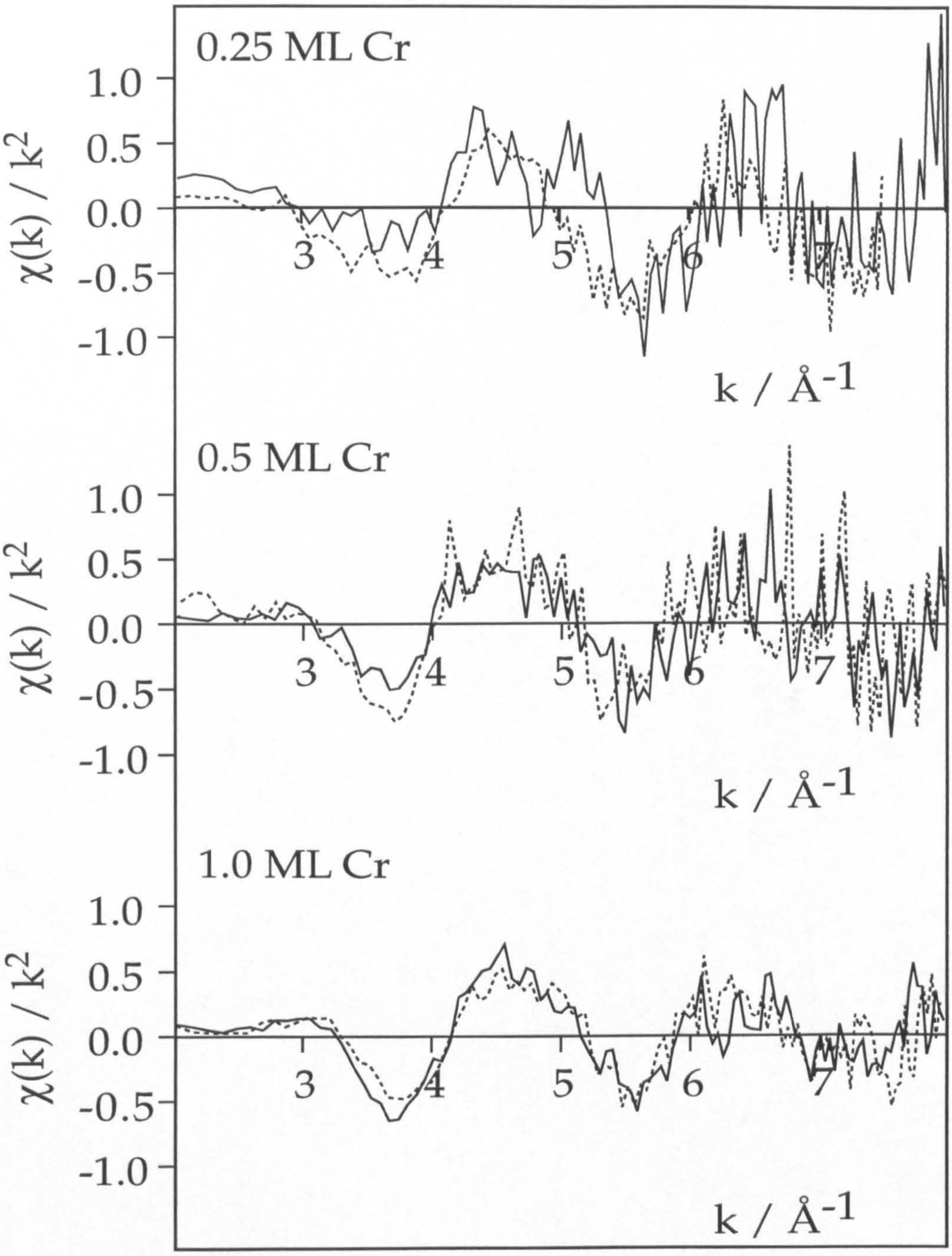

Figure 7 Rev

Figure 4.7 Cr K-edge SEXAFS spectra of Cr deposited on α-quartz (0001) $(\sqrt{84}\mathrm{x}\sqrt{84})$ R11° reconstruction at 298 K after background subtraction conversion to k space and weighting to k^2. The 70° incidence angle data (broken lines) and 20° incidence angle data (solid line) were recorded with the **E** vector parallel to the $[10\bar{1}0]$ azimuth.

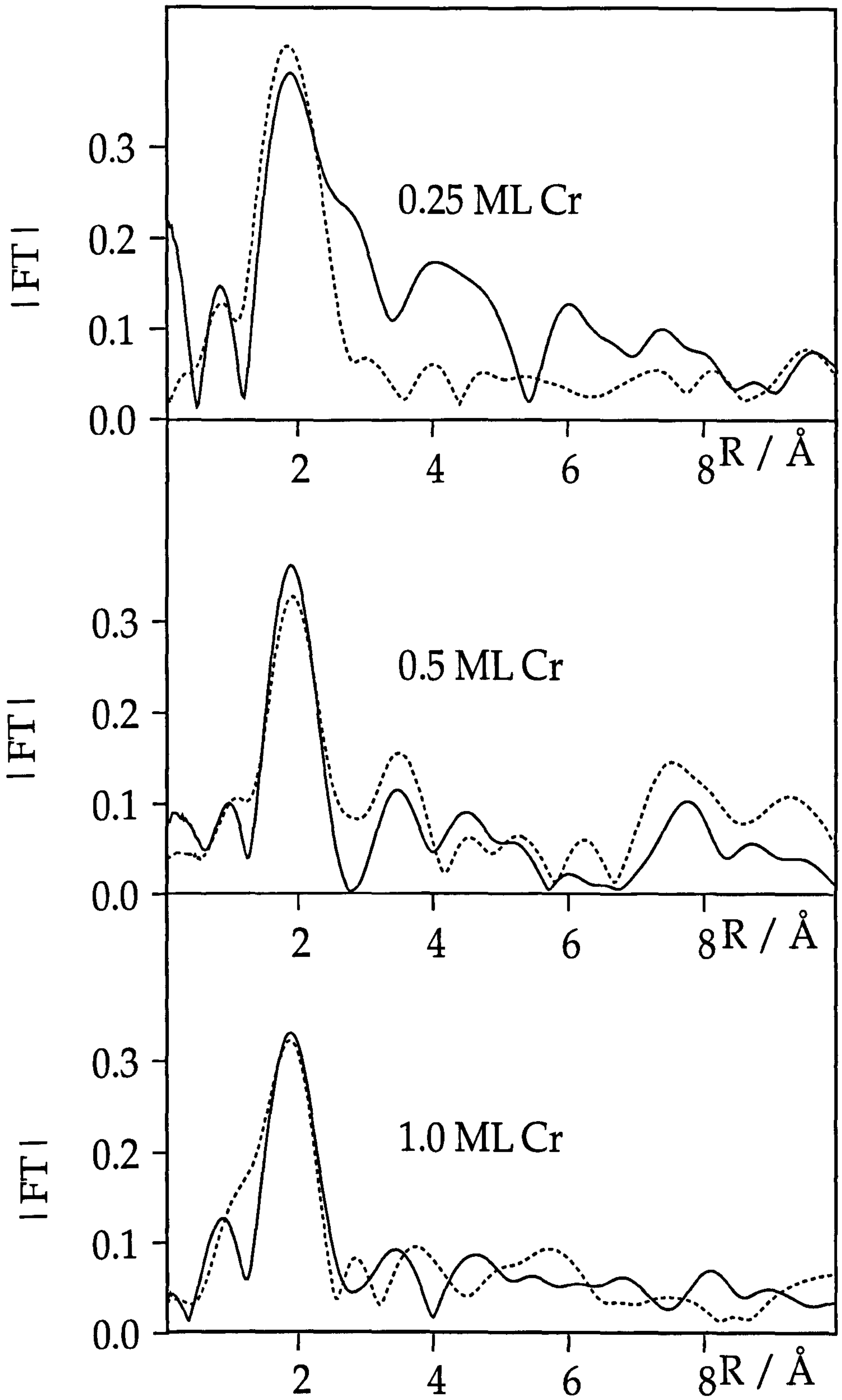

Figure 4.8 Fourier Transforms of Cr K-edge SEXAFS spectra of Cr deposited on α-quartz (0001) $(\sqrt{84}\mathrm{x}\sqrt{84})$ R11° reconstruction at 298 K after background subtraction, conversion to k space and weighting to k^2. The 70° incidence angle data (broken lines) and 20° incidence angle data (solid line) were recorded with the **E** vector parallel to the [10$\bar{1}$0] azimuth.

Model	R-factor
b.c.c (001)	431
f.c.c. (001)	669

Table 4.2 R-factor values for potential models used in data analysis.

The 20° and 70° angle of X-ray incidence data show no significant differences as evidenced by the data in Figures 4.6 and 4.7 the latter showing the experimentally recorded SEXAFS data after background subtraction. The corresponding Fourier transforms are shown in Figure 4.8

The model proposed is based upon a quasi-spherical b.c.c. like arrangement of Cr atoms with a centrally coordinated absorber Cr atom. The nearest neighbour, next nearest neighbour distances and coordination numbers derived from the 20° incidence angle data shown in Figures 4.9, 4.10 and 4.11, which relate to coverages of 0.25±0.08 ML, 0.5±0.16 ML and 1.0±0.33 ML respectively are shown in Table 4.1.

From this it can be seen that the meso-particles exhibit a nearest neighbour distance close to that of the bulk b.c.c. lattice, 2.49 Å,[45] with a second nearest neighbour distance of 2.88 Å.[45] The nearest neighbour distances do not vary significantly between the three coverages from 2.37±0.03 Å at 0.25 ML to 2.35±0.03 Å at 0.5 ML

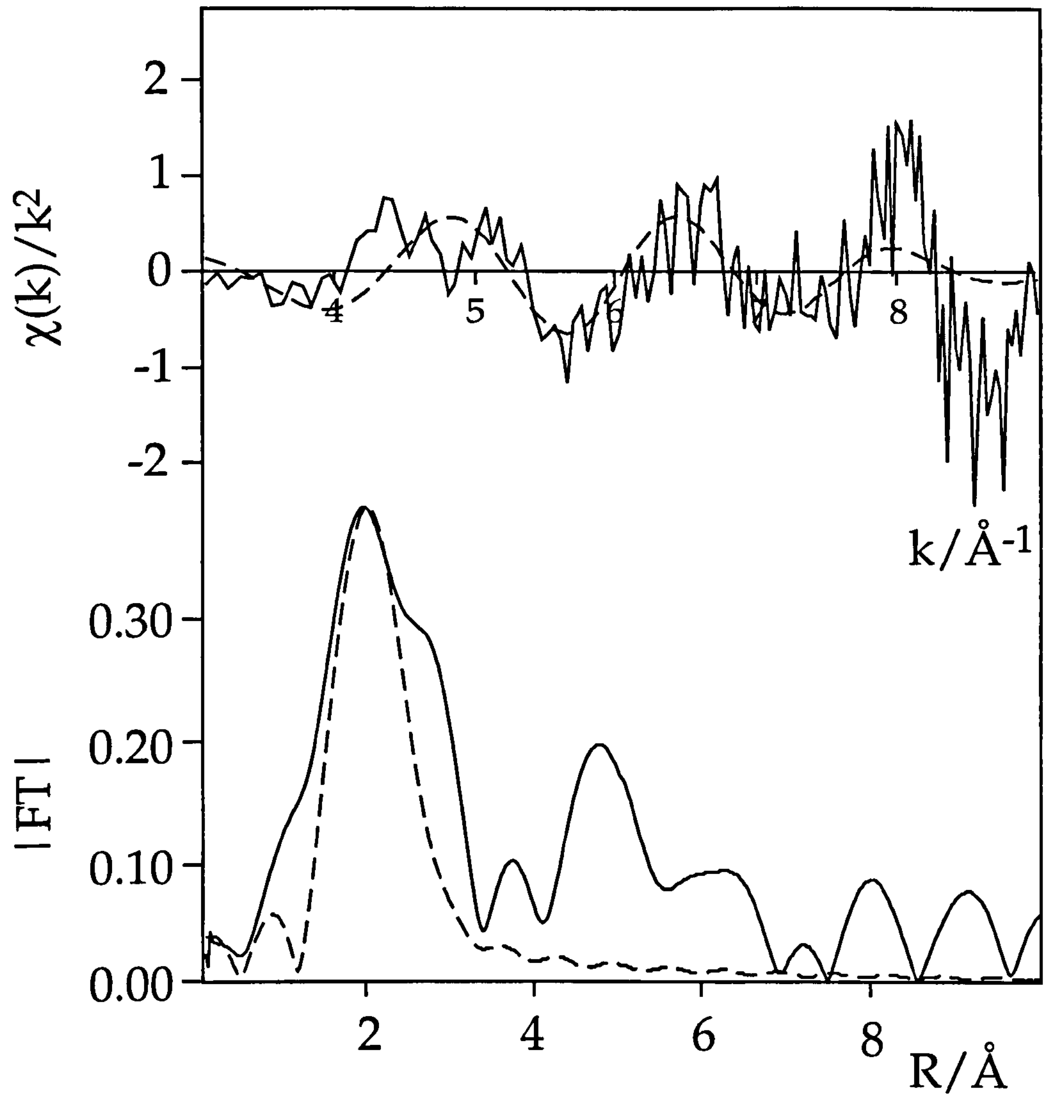

Figure 4.9 Cr K-edge SEXAFS spectrum and corresponding Fourier transform of 0.25 ML Cr deposited on α-quartz (0001) $(\sqrt{84}\times\sqrt{84})$R11° reconstruction at 298 K after background subtraction, conversion to k space and weighting to k^2. The experimental data (solid line) is compared to the best fit theoretical calculation (broken line). The spectrum was recorded at an incidence angle of 20° with the **E** vector parallel to the $[10\bar{1}0]$ azimuth.

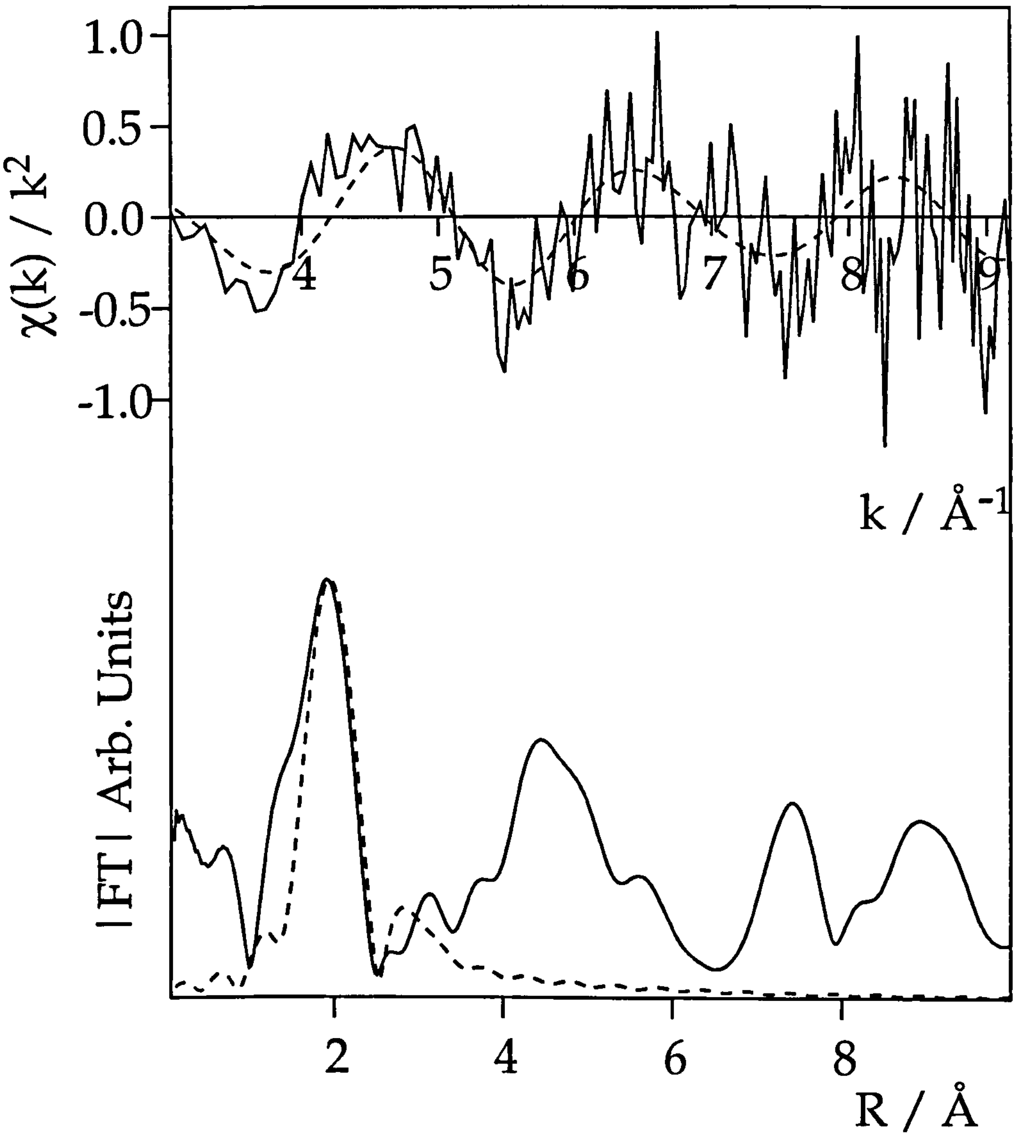

Figure 4.10 Cr K-edge SEXAFS spectrum and corresponding Fourier transform of 0.5 ML Cr deposited on α-quartz (0001) $(\sqrt{84}\times\sqrt{84})$R11° reconstruction at 298 K after background subtraction, conversion to k space and weighting to k^2. The experimental data (solid line) is compared to the best fit theoretical calculation (broken line). The spectrum was recorded at an incidence angle of 20° with the **E** vector parallel to the $[10\bar{1}0]$ azimuth.

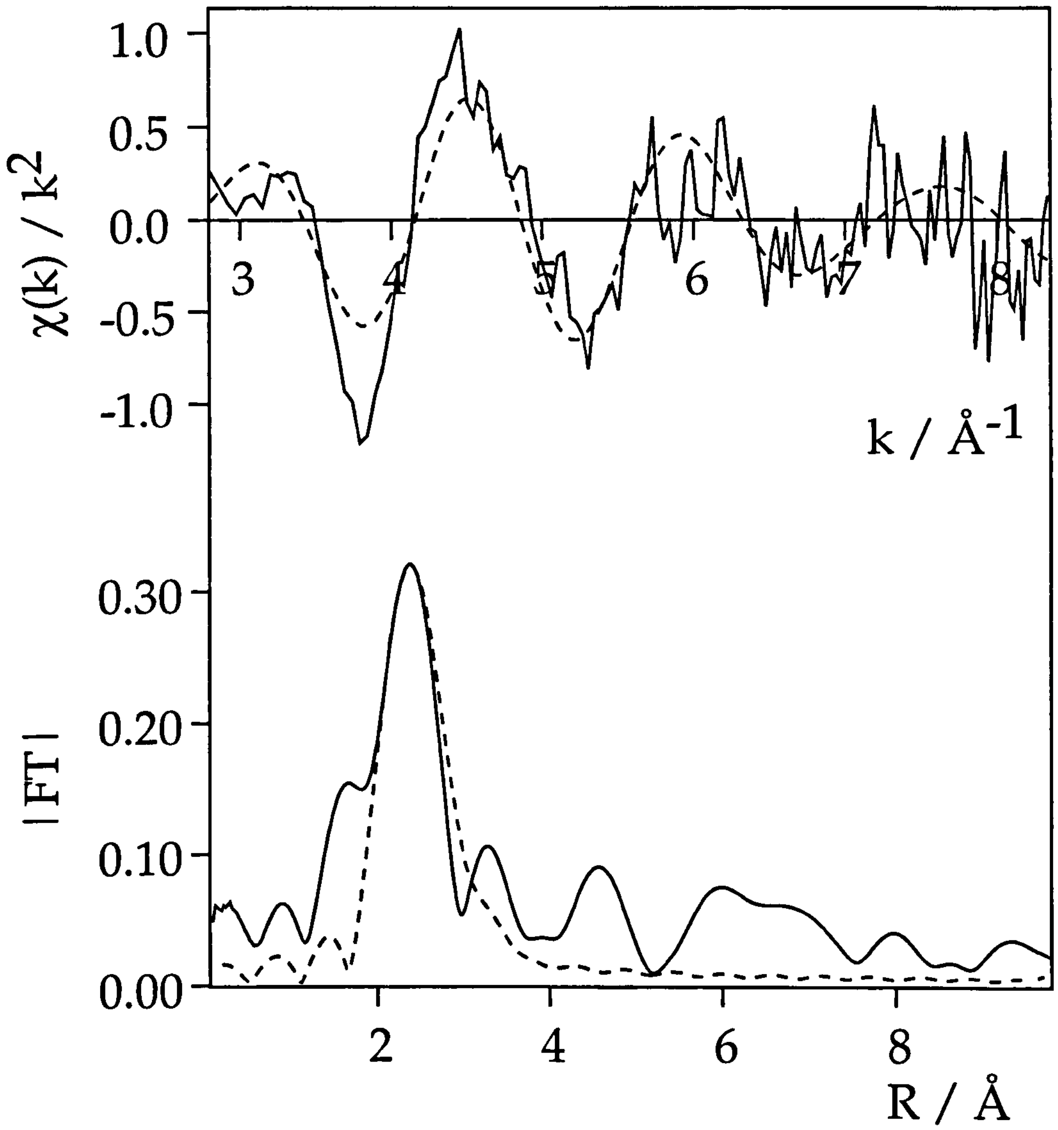

Figure 4.11 Cr K-edge SEXAFS spectrum and corresponding Fourier transform of 1.0 ML Cr deposited on α-quartz (0001) $(\sqrt{84}\times\sqrt{84})$R11° reconstruction at 298 K after background subtraction, conversion to k space and weighting to k^2. The experimental data (solid line) is compared to the best fit theoretical calculation (broken line). The spectrum was recorded at an incidence angle of 20° with the **E** vector parallel to the $[10\bar{1}0]$ azimuth.

coverage and 2.37±0.03 Å at 1.0 ML Cr coverage.

In all three Cr coverage cases, as seen in Figures 4.9, 4.10 and 4.11, there is a constant decrease in nearest neighbour distance of 5.6 % from the bulk b.c.c. lattice distance.

4.4 DISCUSSION

4.4.1 Structural Considerations

A number of models were utilised in attempting to fit the data. An f.c.c. bulk lattice and a b.c.c. bulk lattice were investigated in addition to the use of a freely varying nearest neighbour coordination number in order to emulate a variation in size of an approximately spherical b.c.c.-like sub-nanometric particle. In the f.c.c. and b.c.c. models a good fit in the experimentally derived bond length, was readily attainable, however the amplitude of the calculated rapid curved wave results for these models was too large in both recorded polarisations. The least squared minimisation R-factor for these models at 1.0 ML Cr coverage are shown in Table 4.2. It should be noted that the lack of polarisation dependence in the experimentally derived data is indicative of meso-particulate formation.[20]

The reduction in the Cr nearest neighbour distance is in excellent agreement with an earlier EXELFS study of air oxidised chromium particles[46] and EXFAS of small UHV deposited chromium particles.[47] It is also consistent with EXAFS studies of small particles of Pt in which an apparent bond contraction was noted with increasing temperature,[48] this apparent contraction being attributed to the effect of anharmonicity in the atomic motion of atoms in very small clusters.[44] EXAFS studies of Pt adsorption on γ-alumina have shown three dimensional particle formation with annealing to 300°C, a higher temperature anneal at 450°C resulted in the formation of two-dimensional rafts of Pt.[49] Structural transformations have been previously attributed to hydrogen desorption from the metal-support interface.[50] However it should be noted that there is a high degree of correlation present between E_F and the radial distances, typically 0.85, would be sufficiently large to significantly affect these radial distances if there were significant variation in E_F, however E_F remained within 1.5 eV of the initial value of 12.5 eV for all spectra.

Theoretical studies have shown a dimer growth mode dominates at Cr cluster sizes of less than 12 atoms.[51] However the experimentally derived bond length of the dimers is significantly less, 1.68 Å,[52] than the 2.36 Å observed here which is, as noted earlier,[47] in keeping with a b.c.c. like arrangement in small particles. At cluster sizes of greater than 12 atoms a b.c.c. like arrangement is seen to dominate.[51] The apparent reduction of coordination number below 2.25, for an idealised b.c.c. cluster of 12 atoms, can be explained by the errors introduced due to the large anharmonicity of 'edge' atoms in clusters,[43,44] which represent a significant fraction of the total number of atoms in these mesoscopic particles and also the contribution to the edge step, used in normalisation procedures (See Chapter 2), from Cr atoms present in sites which do not contribute coherently to the SEXAFS, further it neglects surface wetting effects that have been shown to be appreciable in the case of reactive metal adsorption upon oxides.[53] The effects of anharmonicity are exacerbated by the weighting of experimental data to high powers of the wavenumber, k.[43,44] Further to this the ratio of first to second shell coordination numbers, typically 0.6±0.2, lies very close to the expected value of 0.75 for a b.c.c. lattice. The apparent reduction is attributable to only partial occupation of the second coordination sphere.

An attempt to calculate the surface fraction covered can be made by assuming the formation of single discrete spherical mesoscopic particles. Each particle will contain, utilising the calculated coordination numbers and b.c.c. like structure, on average approximately 4-5 atoms and therefore at 0.25 ML coverage only 6.0% of the surface will be covered by the particles and similarly 12.0 % at 0.5 ML and 24.0 % at 1.0 ML Cr coverages.

Attempts to include O or Si in the model resulted in no improvement in the quality of the fit as indicated by no change in the least squared minimisation R-factor, coupled with the reduction in the O and Si coordination numbers to a near zero value. It is therefore concluded that unlike Ti adsorption, on both this the $(\sqrt{84}\mathrm{x}\sqrt{84})$ R11° reconstructed surface and the unreconstructed (1x1) surface, no intercalation of adsorbate metal atoms into the subsurface layers is suggested.

Despite the appearance of shoulders in the Fourier transforms of the data that correspond to the bond lengths of the known chromium oxide structures attempts to include Cr - O scattering could not be justified as there was no improvement in the quality of the fit. Cr_2O_3 has 3 O atoms at 1.97 Å and a further 3 O atoms at 2.02 Å.[45] Cr in CrO_3 has four O nearest neighbours lying between 1.79 Å and 1.81 Å,[54] while in CrO_2 there are four O atoms lying 1.92 Å and a further two at 1.87 Å.[45]

The formation of a chromium silicide phase is not evidenced. The metal rich Cr_3Si phase has a metal silicon distance in excess of 2.86 Å[55] and no feature is observed at this distance in the data. Moreover the Si rich $CrSi_2$ phase has a Cr - Cr distance which is expanded from the bulk spacing of 2.49 Å by approximately 15%.[55] By comparison a Cr-Cr distance of ca. 2.36 Å is observed here.

4.4.2 Thermodynamic Considerations

When considering the nature of interfacial reactions between reactive metals and oxide substrates it is convenient to consider the thermodynamic properties of the interface in terms of the free surface energies of the substrate and the adsorbate species and also the interfacial energy must be accounted for.[56] The principal component of this interfacial energy is the relative enthalpies of the adsorbate oxygen bond and the substrate-oxygen bond.[15] The deposition of Cr upon a TiO_2 (110) substrate has been seen to result in the growth of a quasi-two-dimensional overlayer at coverages of less than 0.8 ML.[17] However the free surface energy of TiO_2 is in the range 0.27 -0.39 Jm^{-2},[57] this is significantly lower than the surface energy of SiO_2,[57] 0.604 Jm^{-2}. On this basis the total energy of the system could be lowered significantly more by an interfacial reaction and spreading of Cr adsorbate upon the SiO_2 substrate than in the case of Cr adsorption upon TiO_2 .

The lack of formation of a metal oxide layer, e.g. Cr_2O_3, is entirely consistent with the thermodynamic stability of the Si - O bond versus the Cr - O bond. The Si - O bond has a bond energy of 4.5 eV[58] and the Cr - O bond is less stable with a bond energy of 3.8 eV.[58] On this basis a negligible reaction of substrate bound oxygen with adsorbed chromium is expected. Further to this is the increase in free surface energy of Cr upon oxidation, from 2.056 Jm^{-2} [59] for the polycrystalline metal to 2.77 - 4.59 Jm^{-2} [60] for various single crystal oxide faces of Cr_2O_3. This would favour the stable formation of metallic particles with only a very limited degree of interfacial reaction. Similarly the reaction of Cr with Si has been shown to have an activation energy of 2.9 eV[61] and is therefore thermodynamically unfavourable at room temperature.

In addition it is possible, considering the preparative method employed,[29] that the quartz surface will be at least in part hydroxylated as it has been shown that quartz surfaces hydroxylate spontaneously in air.[62] Therefore when considering the probability of oxide formation the enthalpy requirements for the rupture of the Si - OH bond must be considered. This has been shown to be 3.4 eV[63] which is only slightly less than the Cr - O bond energy. Again however the relative surface energies of the resultant compounds would serve to limit any such reaction. As noted earlier low temperature Pt adsorption upon γ-alumina[49] results in three-dimensional particles associated with a hydroxylated termination of the substrate at the metal-substrate interface.

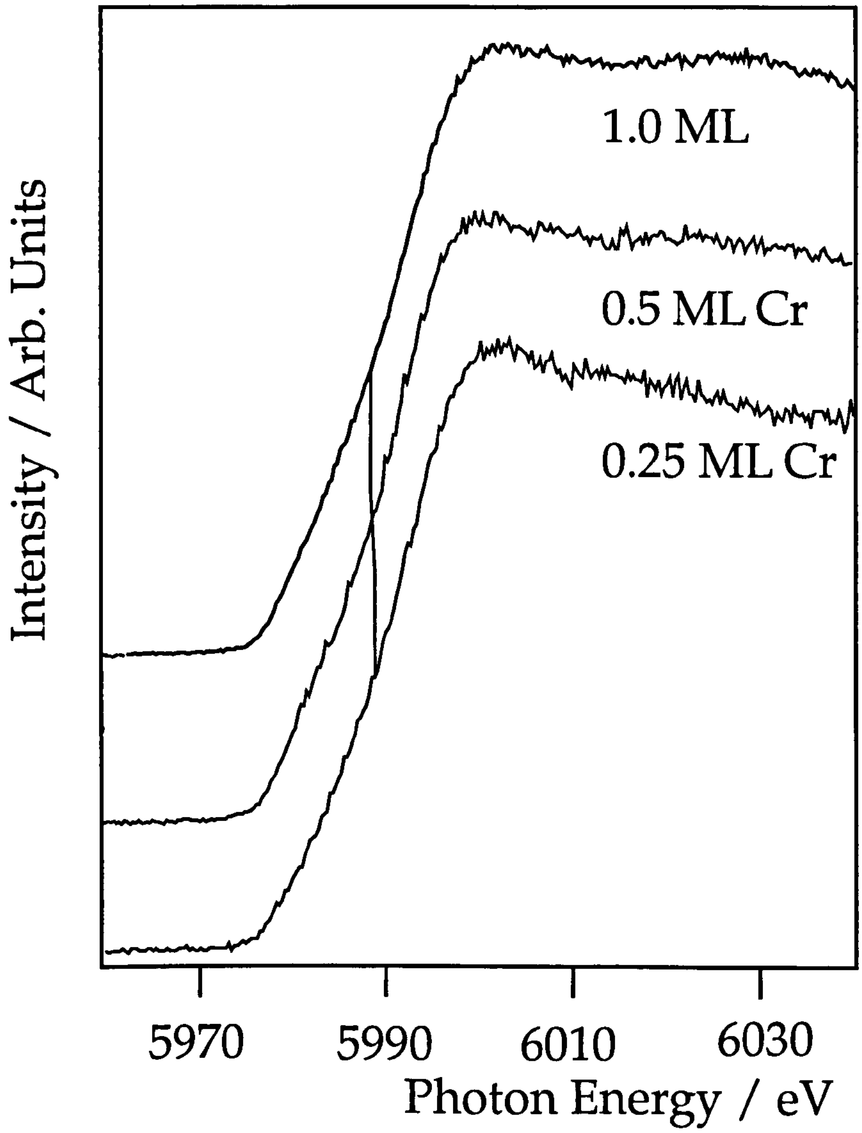

Figure 4.12 Cr K-edge XANES recorded from α-quartz (0001) $(\sqrt{84}\mathrm{x}\sqrt{84})$R11° at 298 K at 0.25 ML, 0.5 ML and 1.0 ML coverages. The spectra were recorded at an incidence angle of 20° with the E vector parallel to the $[10\bar{1}0]$ azimuth.

The constancy in the size of the Cr particles formed infers a limitation in surface diffusivity of the adsorbed Cr atoms. This may arise from the possible hydroxylation of the surface or the pinning of Cr clusters by dislocations at the Dauphiné twin domain walls.[64]

4.4.3 Cr K-Edge XANES

Figure 4.12 shows Cr K-edge XANES, taken at 20° incidence angle at 298K from all three coverages studied. This shows no significant increase in the binding energy of the core level at the half intensity point, 5988.5 eV at 0.25 ML 5988.0 eV at 1.0 ML Cr coverage. This is in direct contrast to the corresponding 2.4 eVshift in edge position observed for Ti adsorption upon both the (1x1) and $(\sqrt{84}\mathrm{x}\sqrt{84})\mathrm{R}11^\circ$ α-quartz surfaces. It is suggested that the lack of the absorption edge shift in the case of Cr adsorption when compared to Ti adsorption is due to the nature of the surface interaction in that a direct chemical reaction is occurring on Ti adsorption but no reaction is observed for Cr adsorption.

4.5 Conclusion

Cr adsorption upon α-quartz (0001) $(\sqrt{84}\mathrm{x}\sqrt{84})\mathrm{R}11^\circ$ results in the formation of subnanometric meso-particles having an average size of approximately 4 -5 atoms for coverages below 1.0 ML. The lack of reaction of Cr with surface oxygen and coalescence of these particles in attributed to either possible hydroxylation of the silica surface resulting is a more stable surface than the O terminated surface or the pinning of the clusters at the Dauphiné twin boundaries by dislocations in the quartz lattice.

References.

1. G. Leveque, J. Peisner and Y. Sangare, Appl. Opt., **33**, 1857, (1994)

2. P.C. Karulkar, Thin Solid Films, **121**, 259, (1984)

3. A. Zalar, S. Hofmann and P. Panjan, Thin Solid Films, **206**, 327, (1991)

4. T.J. Finstad, O. Thomas and F.M. D'Heurle, Appl. Surf. Sci., **38**, 106, (1989)

5. S.J. Tauster, S.C. Faung and R.J. Garten, J. Am. Chem. Soc., **100**, 170, (1978)

6. H.R. Sadeghi and V.E. Henrich, J. Catalysis, **109**, 1, (1988)

7. C.E. Marsden in "Preparation of Catalysts V", pp. 215-227, G. Poncelet, P.A. Jacobs, P. Grange and B. Delmon eds., (Elsevier Science Publishers B.V., Amsterdam, 1991)

8. M.P. M^{c}Daniel, Ind. Eng. Chem. Res., **27**, 1559, (1988)

9. J.B.A.D. Van Zon, D.C. Koningsberger, H.F.J. Van't Blik and D.E. Sayers, J. Chem. Phys., **82**, 5742, (1985)

10. R.W. Joyner and P. Meehan, Vacuum, **33**, 691, (1983)

11. R.W. Joyner, E.S. Shpiro, P. Johnston, K.M. Minachev and G.G. Tuleova, Catal. Lett., **11**, 319, (1991)

12. F.B.M. Duivenvoorden, B.J. Kip, D.C. Koningsberger and R. Prins, J. C. Physique, **47**, 227, (1986)

13. A.S. Fung, M.J. Kelley, D.C. Koningsberger and B.C. Gates, J. Am. Chem. Soc., **119**, 5877, (1997)

14. J.-M. Pan and T.E. Madey, J. Vac. Sci. Technol., **A11**, 1667, (1993)

15. U. Diebold, J.-M. Pan and T.E. Madey, Surf. Sci., **287/288**, 896, (1993)

16. U. Diebold, J.-M. Pan and T.E. Madey, Surf. Sci., **331-333**, 845, (1995)

17. J.-M. Pan and T.E. Madey, Surf. Sci., **295**, 411, (1993)

18. J.T. Mayer, U. Diebold, T.E. Madey and E. Garfunkel, J. Electron Spectrosc. Relat. Phenom., **73**, 1, (1995)

19. U. Diebold, J.-M. Pan and T.E. Madey, Phys. Rev. B, **47**, 3868, (1993)

20. M. Gautier-Soyer, S. Gota, L. Douillard, J.P. Duraud and P. Le Fèvre, Phys. Rev. B, **54**, 10366, (1996)

21. F. Didier and J. Jupille, Surf. Sci., **309**, 587, (1994)

22. A.M. Flank, R. Delaunay, P. Lagarde, M. Pompa and J. Jupille, Phys. Rev. B., **53**, R1737, (1996)

23. S.N. Towle, J.R. Bargar, G.E. Brown Jr., G.A. Parks and T.W. Barbee Jr., Stanford SRL Activity Report 1994, p. 125.

24. X.Xu, J. Szanyi, Q. Xu and D.W. Goodman, Catalysis Today, **21**, 57, (1994)

25. M.A. Taubenblatt and C.R. Helms, J. Appl. Phys., **53**, 6308, (1982)

26. S.K. Saha, H. Jain, A.C. Miller and R.K. Brown, Surf. Interface Analysis, **24**, 113, (1996)

27. 'Charging Effects In Electron Spectroscopies', Special Issue of J. Electron Spectrosc. Relat. Phenom., **59**, (1992)

28. F. Bart, M.J. Guittet, M. Henriot, N. Thromat, M. Gautier and J.P. Duraud, J. Electron Spectrosc. Relat. Phenom., **69**, 245, (1994)

29. F. Bart and M. Gautier, Surf. Sci. Lett., **311**, L671, (1994)

30. R.B. Sosman, "The Phases of Silica", (Rutgers University Press, New Jersey, 1965)

31. J. Van Landuyt, G. Van Tendeloo, S. Amelinckx and M.B. Walker, Phys. Rev. B, **31**, 2986, (1985)

32. A.W. Robinson, S. D'Addato, V.R. Dhanak, P. Finetti and G. Thornton, Rev. Sci. Instrum., **66**, 1769, (1995)

33. F. Bart, M. Gautier, J.P. Duraud and M. Henriot, Surf. Sci., **274**, 317, (1992)

34. J.J. M^{c}Clelland, J. Unguris, R.E. Scholten and D.T. Pierce, J. Vac. Sci. Technol., **A11**, 2863, (1993)

35. S.J. Gurman, N. Binsted and I. Ross, J. Phys. C, **17**, 143, (1984)

36. S.J. Gurman, N. Binsted and I. Ross, J. Phys. C, **19**, 1845, (1986)

37. N. Binsted and D. Norman, in : "The Strucutre of Surfaces IV", Eds. Xide Xie, S.Y. Tong and M.A. Van Hove, (World Scientific, Singapore, 1994)

38. N. Binsted and D. Norman, Phys. Rev.B, **49**, 15531, (1994)

39. S.J. Gurman, J. Phys. C: Solid State Phys., **21**, 3699, (1988)

40. L. Hedin and S. Lundqvist, Solid State Phys., **23**, 1, (1969)

41. S. Ogawa and S. Ichikawa, Phys. Rev. B, **51**, 17231, (1995)

42. J. Stöhr in "Chemical Analysis Vol. 92, 'X-ray Absorption - Principles, Applications, Techniques of EXAFS, SEXAFS and XANES'", Eds. D.C. Koningsberger and R. Prins, (Wiley Interscience, John Wiley and Sons Inc., London, 1988)
43. B.S. Clausen, H. Topsøe, L.B. Hansen, P. Stoltze and J. Nørskov, Jpn. J. Appl. Phys., **Suppl. 32 - 2**, 95, (1993)
44. B.S. Clausen, H. Topsøe, L.B. Hansen, P. Stoltze and J. Nørskov, Catalysis Today, **21**, 49, (1994)
45. R.W.G. Wyckoff "Crystal Structures Vol. 2", (Wiley Interscience, John Wiley and Sons Inc., London, 1964)
46. M. Diociaiuti and L. Paoletti, J. Microsc., **162**, 279, (1991)
47. M. Decrescenzi, L. Lozzi, M. Passacanantando, P. Picozzi and S. Santucci, Thin Solid Films, **193**, 318, (1990)
48. E.C. Marques, D.R. Sandstrom, F.W. Lytle and R.B. Greegor, J. Chem. Phys., **77**, 1027, (1982)
49. M. Vaarkamp, J.T. Miller, F.S. Modica and D.C. Koningsberger, J. Catal., **163**, 294, (1996)
50. D.C. Koningsberger and B.C. Gates, Catal. Lett., **14**, 271, (1992)
51. H. Cheng and L.-S. Wang, Phys. Rev. Lett., **77**, 51, (1996)
52. E.P. Kundig, M. Moskovits and G. Ozin, Nature (London), **254**, 503, (1975)
53. H.-P. Steinrück, F. Pesty, L. Zhang and T.E. Madey, Phys. Rev. B, **51**, 2427, (1995)
54. A.F. Wells, "Structural Inorganic Chemistry", (Oxford University Press, London, 1986)
55. B. Aronsson, T. Lunström and S. Rundqvist, "Borides, Silicides and Phosphides. A Critical Review Of Their Preparation, Properties and Crystal Chemistry", (Methuen and Co. Ltd., London, 1965)
56. C.T. Campbell, Surf. Sci. Rep., **27**, 1, (1997)
57. S.H. Overbury, P.A. Bertrand and G.A. Somorjai, Chem. Rev., **75**, 547, (1975)
58. R.C. Weast, Ed., "CRC Handbook of Chemistry and Physics", (1977-1978)
59. L.Z. Mezey and J. Giber, Jap. J. Appl. Phys., **21**, 1569, (1982)
60. P.J. Lawrence, S.C. Parker and P.W. Tasker, J. Am. Ceram. Soc., **71**, C389, (1988)

61. T.E. Schlesinger, R.C. Cammarata and S.M. Prokes, Appl. Phys. Lett., **59**, 449, (1991)

62. C. Noguera, J. Goniakowski and S. Bouette-Russo, Surf. Sci., **287/288**, 188, (1993)

63. A. Vittadini, A. Selloni and M. Casarin, Phys. Rev. B, **52**, 5885, (1995)

64. M.B. Walker and R.J. Gooding, Phys. Rev. B., **32**, 7408, (1985)

Chapter 5

A SEXAFS study of α-quartz (0001)$\left(\sqrt{84}\text{x}\sqrt{84}\right)$ R11$^{\text{o}}$-Ti and α-quartz (0001)(1x1)-Ti

5.1 INTRODUCTION

The titanium - silicon dioxide interface has gained prominence due to its importance in a wide range of commercially and technologically important systems such as metalisation of CMOS devices,[1] the formation of low resistivity contacts to Si in ultra-large scale integration (ULSI)[2] and the effect of Ti loading in ethene polymerisation catalysts on the degree of branching of the polyethene formed.[3]

The study described in this thesis is the first investigation of the effect of reactive metal physical vapour deposition (PVD) upon a single crystal silicon dioxide substrate. It follows from the systematic investigation of the growth of a wide range of metals upon TiO_2 (110), which have elucidated trends in surface wetting which are correlated to metal reactivity, the growth modes of metals upon this surface[4-12] and the surfactant effect of coadsorbed reactive gases with metal deposition.[13]

Adsorption of metals upon silicon dioxide has until now been limited to studies carried out upon thin oxide films thermally grown upon single crystal silicon wafers or mica sheets[14-19] and cleaved polycrystalline glass samples.[20,21] This is due to the difficulties in applying electron and ion spectroscopies[22] to bulk silicon dioxide arising from the highly insulating nature of the substrate, the bulk band gap being approximately 9.0 eV.[23] This problem is circumvented here via the use of a fluorescence yield detection scheme for the surface EXAFS measurements presented. The (0001) surface of α-quartz has two known stable terminations,[24] the (1x1) unreconstructed surface and also the $(\sqrt{84}\times\sqrt{84})R11^\circ$ reconstruction. This reconstruction is thought to be due to the effect of Dauphiné twin domains resulting from an incommensurate phase at the surface upon cooling through the β - α phase transition.[24-26]

5.2 EXPERIMENT

Experiments were performed in a UHV chamber, base pressure below $2\mathrm{x}10^{-10}$ mbar, equipped with a VSW HA 100 MCD hemispherical analyser, VSW EG5 electron gun and Omicron rearview LEED for sample characterisation. A VG Micromass 200 quadrupole mass spectrometer was used for residual gas analysis and sample transfer system. (See Section 3.3.1)

Titanium K edge (4966 eV) SEXAFS measurements were performed using a Ge(111) crystal pair in the double-crystal monochromator of station 4.2 at SRS, Daresbury Laboratory.[27] (See Section 3.7.2) An EG&G 3 channel lithium drifted silicon solid state fluorescence detector (See Section 3.6.2) was used to record the Ti Kα fluorescence yield as a monitor of the surface X-ray absorption coefficient. Normalisation of the surface EXAFS data to the incident photon flux was accomplished by measuring the drain current from a thin Al foil placed between the monochromator and sample chamber. Surface EXAFS and XANES spectra were recorded at ambient temperature, 298 K, with the E vector in the $[10\bar{1}0]$ azimuthal direction at both near normal, $\theta_i = 20°$, and near grazing, $\theta_i = 70°$, angles of incidence.

The α-quartz sample (Pi-Kem) was polished to within 0.3° of the (0001) plane as determined by Laue diffraction. The (1x1) surface was obtained by etching the sample in 2% HF followed by ex-situ annealing of the sample, in air, to 350°C for 6 hours then transfer to the UHV chamber via the sample transfer system whilst still at a temperature in excess of 200°C.[24] A typical LEED pattern from the (1x1) α-quartz (0001) surface is shown in Figure 1. The $(\sqrt{84}\mathrm{x}\sqrt{84})\,\mathrm{R}11^{\circ}$ reconstruction was formed by an etch in 2% HF followed by ex-situ annealing of the sample to 900°C for 3 hours in air, allowing the sample to cool to 350°C, and transferring to UHV whilst still at a temperature in excess of 200°C.[24] Surface order and cleanliness were checked via LEED and AES at the edge of the sample in order to minimise electron beam damage to the surface area to be investigated.[28]

Vapour deposition of titanium was achieved via either an electron beam microevaporator, VSW ME10, or direct evaporation from a resistively heated titanium filament. During evaporation the pressure in the chamber was observed to increase to a maximum of 7×10^{-10} mbar, of which the predominant gas was hydrogen. Titanium coverages were calculated from the ratios of the O(KLL) and Ti(LMM) Auger electron signals at 0.25±0.08 ML. This was then correlated with the Ti K-edge step at 0.25 ML coverage. Higher coverages employed the interpolation of the magnitude of the absorption edge. The Ti and O Auger signals were chosen as they exhibit similar charging effects due to their similarity in kinetic energy. The Auger spectrum from which the coverages were estimated is shown in Figure 4.2. This again was an attempt to minimise the known effects of electron beam damage on the SiO_2 surface.[28] The surface cleanliness was checked at the end of each set of measurements and coverages were recalculated in order to check for oxygen and carbon contamination during data acquisition. No contamination was detected.

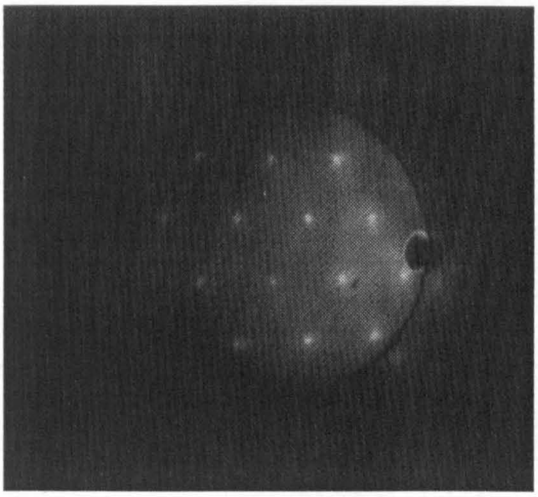

Figure 5.1 LEED pattern from α-quartz (0001) (1x1). (Primary beam energy 92 eV)

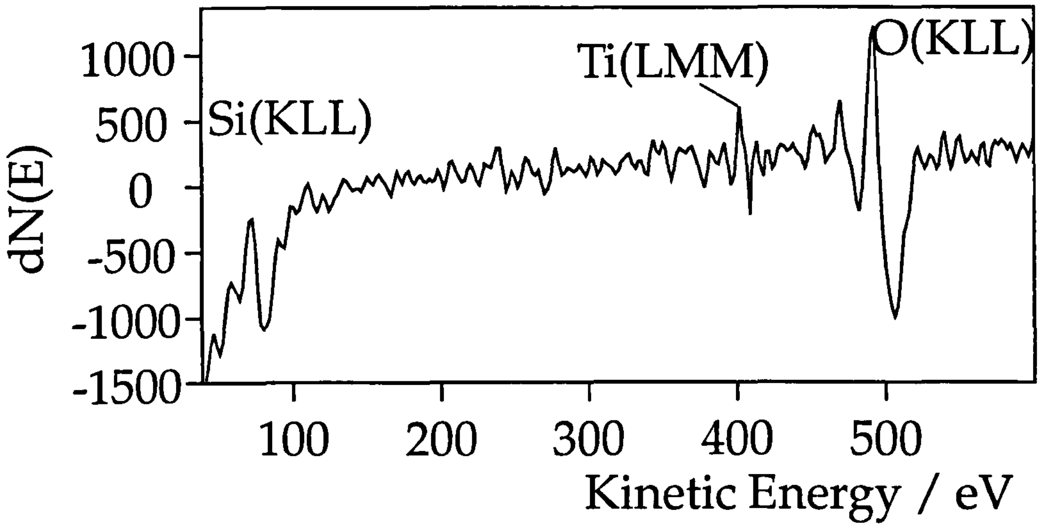

Figure 5.2 Auger electron spectrum from 0.25 ML Ti deposited upon α-quartz (0001) (1x1). (Primary beam energy 3 keV, normal emission)

Background subtraction of the EXAFS data was performed using the Daresbury Laboratory EXBACK programme utilising first order polynomials in the pre-edge region and up to three second order polynomials with a constant first derivative for the post edge region. The fitting procedure used a new variant of the EXCURV92 code [29,30] which allows simultaneous fitting of both normal incidence and grazing incidence spectra in comparison to a preconstructed model, leading to a self-consistent array of fitting parameters. The refinement procedure exploits, where applicable, the crystallographic symmetry of the data to increase the determinacy of the fitting parameters.[31] Non-structural parameters such as Debye-Waller like factors and many body effects were ascertained from the fitting of a multilayer Ti spectrum, shown in Figure 5.3, leaving only structural parameters to be varied during the fitting procedure. This new code utilises full spherical wave theory in which the small atom approximation to the polarisation-dependent angle factor breaks down only within about 15 eV of the edge [32,33] and also employs ab-initio derived phaseshifts using Hedin-Lundqvist potentials.[34]

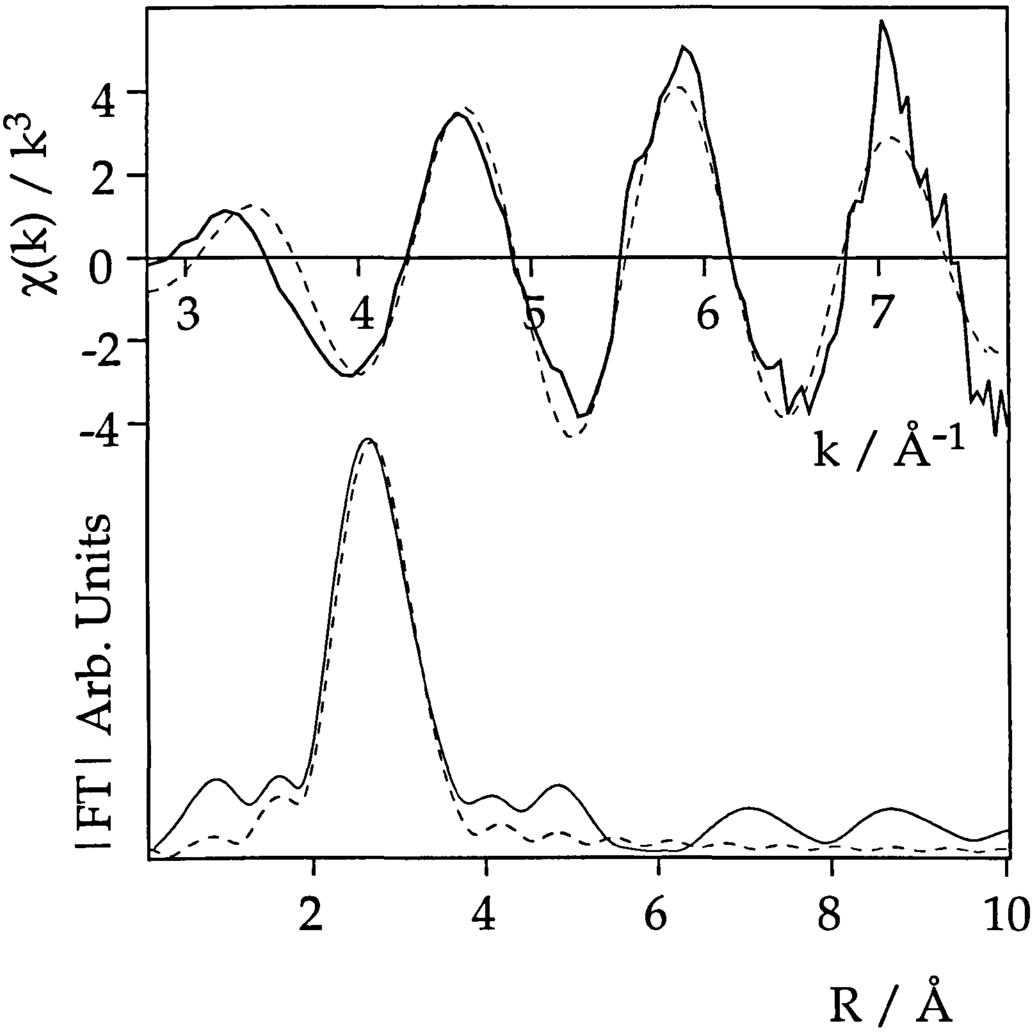

Figure 5.3 Ti K-edge EXAFS spectrum and corresponding Fourier transform of multilayer Ti deposited on α-quartz (0001) $(\sqrt{84}\times\sqrt{84})$R11° at 298 K after background subtraction, conversion to k space and weighting to k^3. The spectrum was recorded with the E vector parallel to the $[10\bar{1}0]$ azimuth at an incidence angle of $\theta_i=20^{\circ}$.

5.3 RESULTS

To investigate the nature of the growth mode of Ti upon single crystal α-quartz (0001) surfaces a series of fluorescence yield Surface EXAFS measurements were performed for titanium coverages of 0.25±0.08 ML, 0.5±0.16 ML and 1.0±0.33 ML. Fluorescence yield SEXAFS is particularly useful as it is insensitive to the effects of sample charging[22] which is likely to be exacerbated in this case by the formation of a surface capacitance upon metal adsorption.[35] It is also highly surface specific for the case of adsorption of a non-substrate atom type upon the substrate and also allows the detection of coverages below the level detectable by Auger electron spectroscopy due to an improved signal-background ratio.[36]

Figure 5.4 shows normalised Ti K-edge SEXAFS data from Ti on the α-quartz (0001) (1x1) surface. Correspondingly, Figure 5.5 shows the normalised SEXAFS data from the $(\sqrt{84}\times\sqrt{84})\,R11^{\circ}$ termination.

As can be seen from Figure 5.6 there is a lack of a polar angular dependence in the data, which is taken as an indication of an interfacial region which extends significantly both in the plane of the surface and also perpendicular to it. Figure 5.7 contains the corresponding Fourier transforms. This lack of polar angular dependence is a feature common to all spectra for both the (1x1) and $(\sqrt{84}\times\sqrt{84})\,R11^{\circ}$ surfaces and therefore only near normal incidence spectra, recorded at $\theta_i = 20^{\circ}$ will be shown.

5.3.1 Ti Adsorption on the (1x1) (0001) α-quartz surface

Figures 5.8, 5.9 and 5.10 shows the background subtracted SEXAFS data, weighted to k^3, recorded at 0.25±0.08 ML, 0.5±0.16 ML and 1.0±0.33 ML Ti coverages respectively, on the α-quartz (0001) (1x1) surface and their Fourier transforms with the

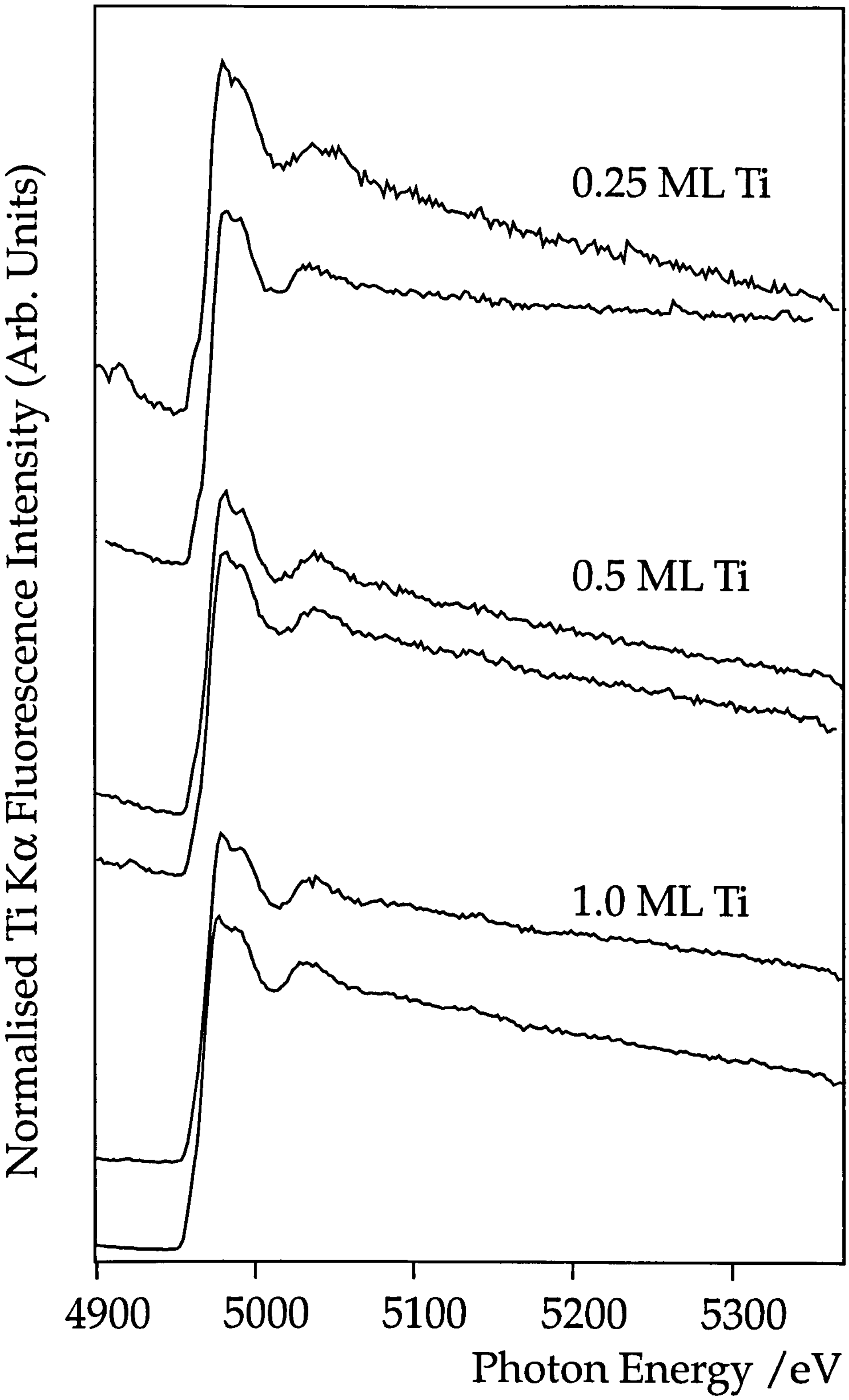

Figure 5.4 Ti K-edge X-ray absorption spectra from Ti adsorption upon α-quartz (0001) (1x1) at 298 K with the **E** vector parallel to the $[10\bar{1}0]$ azimuth with both 70° incidence angle (upper line) and 20° incidence angle (lower line). Nominal coverages are indicated. The data have been edge step normalised between coverages at 5020 eV.

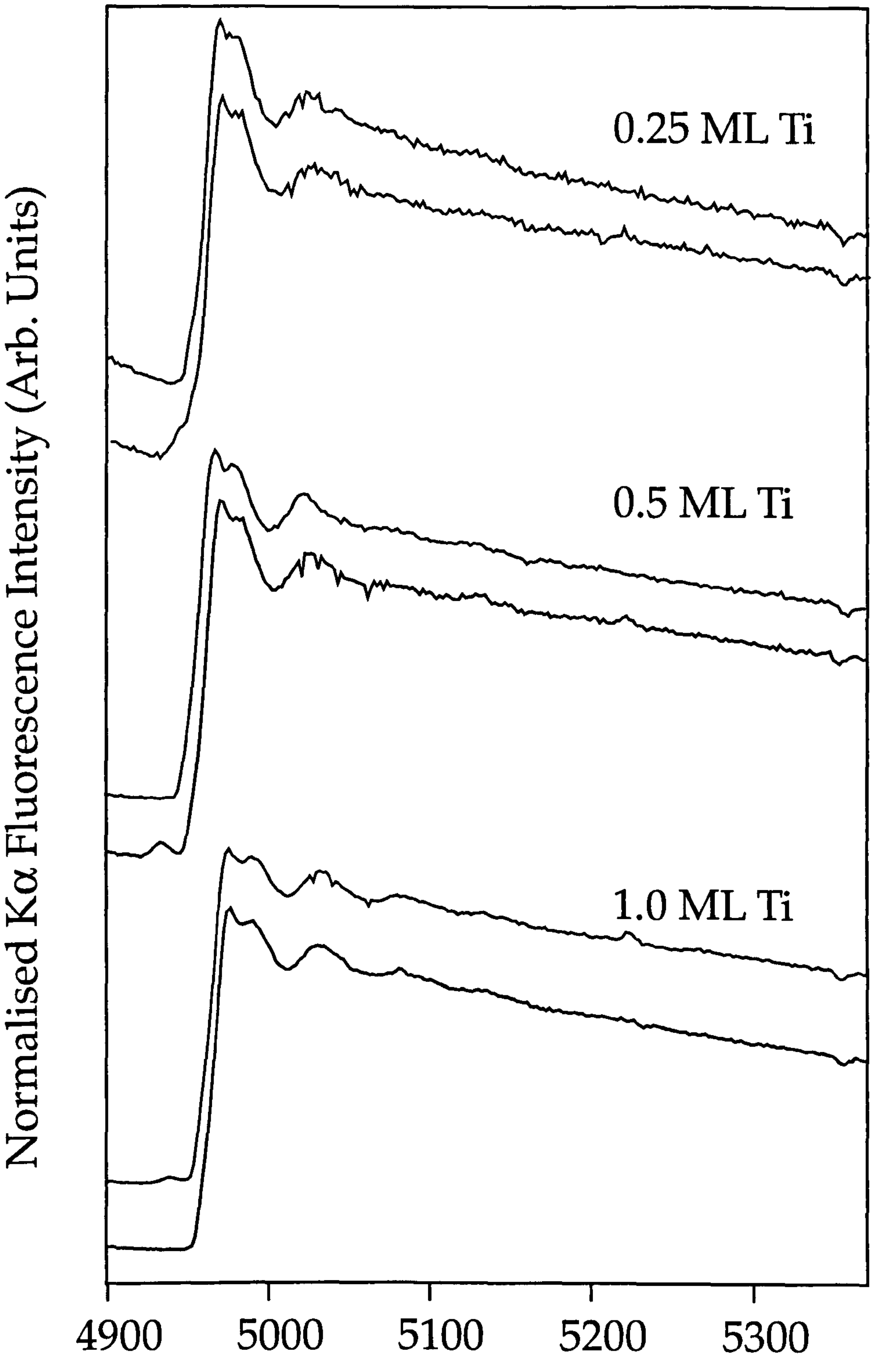

Figure 5.5 Ti K-edge X-ray absorption spectra from Ti adsorption upon α-quartz (0001) $(\sqrt{84}\times\sqrt{84})$ R11° at 298 K with the **E** vector parallel to the $[10\bar{1}0]$ azimuth with both 70° incidence angle (upper line) and 20° incidence angle (lower line). Nominal coverages are indicated. The data have been edge step normalised between coverages at 5020 eV.

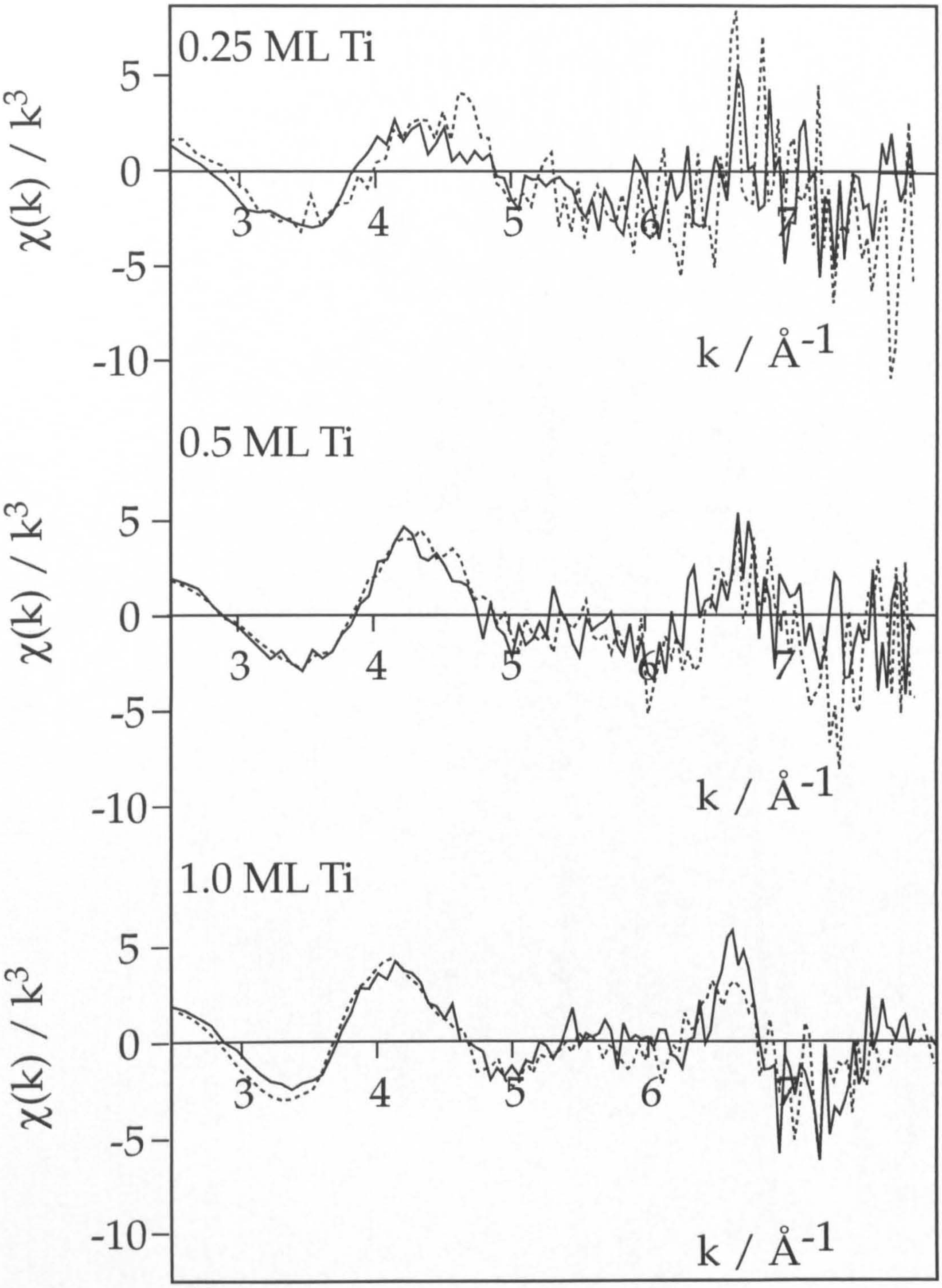

Figure 5.6 Ti K-edge SEXAFS spectra of Ti adsorbed upon α-quartz (0001) (1x1) after background subtraction and weighting to k^3. Shown are both near normal incidence (solid lines) and grazing incidence (broken lines) spectra. The nominal coverages are indicated.

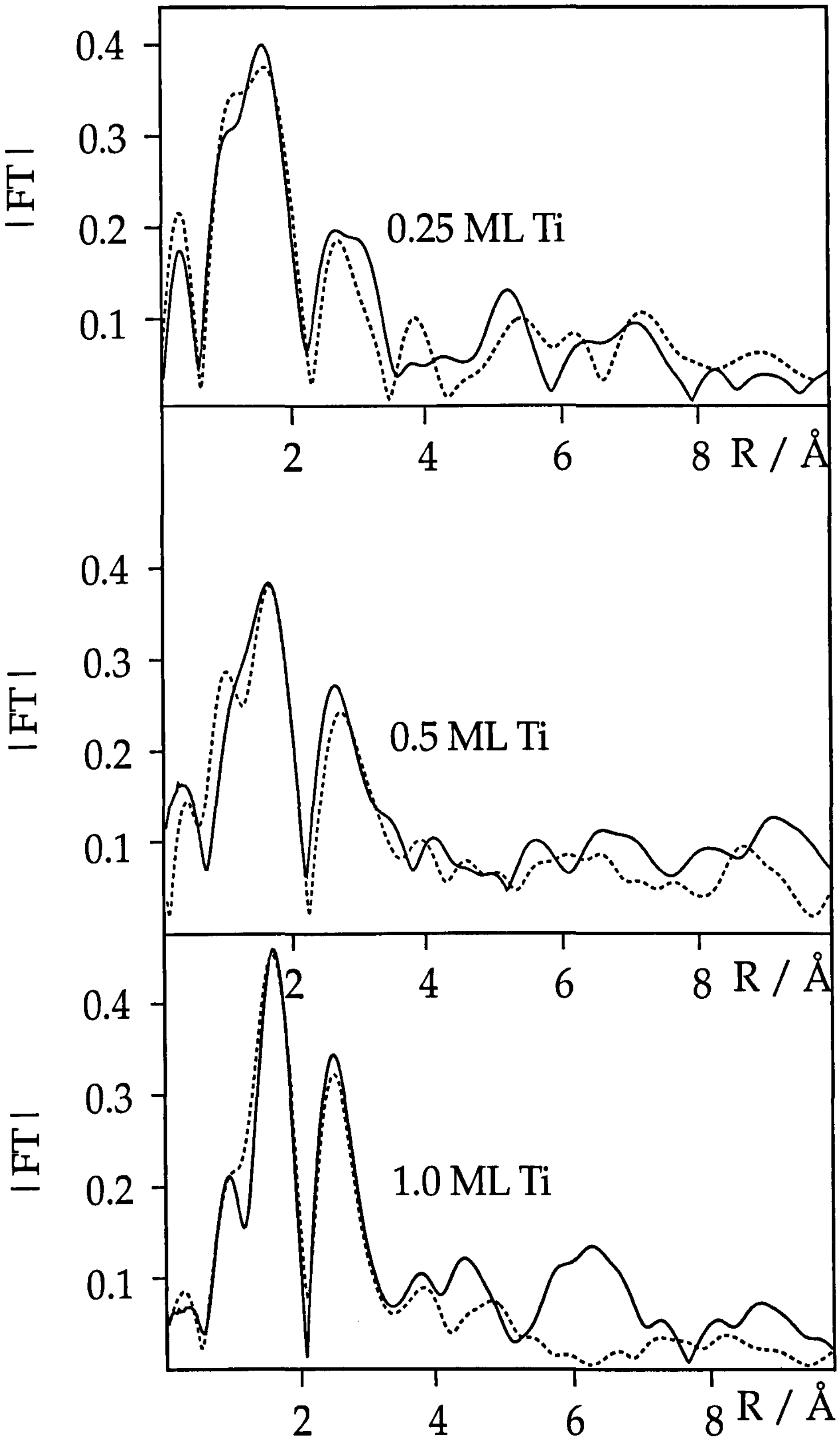

Figure 5.7 Fourier transforms of Ti K-edge SEXAFS shown in Figure 5.6, from Ti adsorbed upon α-quartz (0001) (1x1). Shown are both near normal incidence (solid lines) and grazing incidence (broken lines) spectra. Nominal coverages are indicated.

Coverage / ML	Si Model R-Factor	No Si Model R-Factor
0.25	66.67	67.63
0.5	55.61	46.83
1.0	50.80	38.90

Table 5.1 Least squared R-factor for intercalation model (Si) and surface reaction model (No Si) on the (1x1) surface.

best fit theoretical models.

Table 5.1 summarises the results obtained from the least squared R-factor best-fit analysis utilised in the fitting procedure.[29,30] Table 5.1 shows the least squared R-factor values for the best fits obtained for both a model including Ti, Si and O coordination implying an intercalation of Ti into the substrate lattice, and also a model containing only O coordination indicating a surface reaction and passivation of the substrate.

Coverage / ML	Si Model χ^2/x10^{-6}	No Si Model χ^2/x10^{-6}
0.25	194.03	116.47
0.5	171.99	58.48
1.0	217.65	65.11

Table 5.2 χ^2 quality of fit index for the intercalation (Si) model and surface reaction (No Si) model on the (1x1) surface.

The intercalation model, in which a Ti atom was placed in the centre of a quartz unit cell and the position of the Ti within the unit cell is varied, does yields comparable R-factors to the surface reaction model to the data at 0.25 ML and 0.5 ML Ti coverages. However, the intercalation model does have a higher number of degrees of freedom[37] associated with the fitting procedure than the surface reaction model. The higher the number of degrees of freedom of a system, the better the fit would be expected to be. Therefore the use of a more rigorous statistical χ^2 analysis,[38] which account for the number of degrees of freedom of the system and the number of relevant independent data points in the spectrum,[39] is essential in order to prevent the data analysis becoming a statistical irrelevance. The results of this analysis are shown in Table 5.2, from which it can be seen that the surface reaction model is preferred.

Coverage /ML	Atom Type	Coordination Number	Radius /Å ± 0.03 Å
0.25	O Ti	6.6±1.2 2.5±1.5	2.00 2.92
0.5	O Ti	4.0±0.9 3.4±1.4	1.96 2.89
1.0	O Ti	4.9±1.0 5.7±1.8	2.00 2.90

Table 5.3 Best fit parameters for Ti/SiO_2(0001) (1x1) surface.

It must be noted that due to the inseparable nature of the absorption edges arising from Ti - Ti backscattering and Ti - O backscattering, which prevents normalisation to the actual surface concentration of each species. An attempt has been made to correct for this by normalising the derived Ti - O coordination to 6 and scaling the

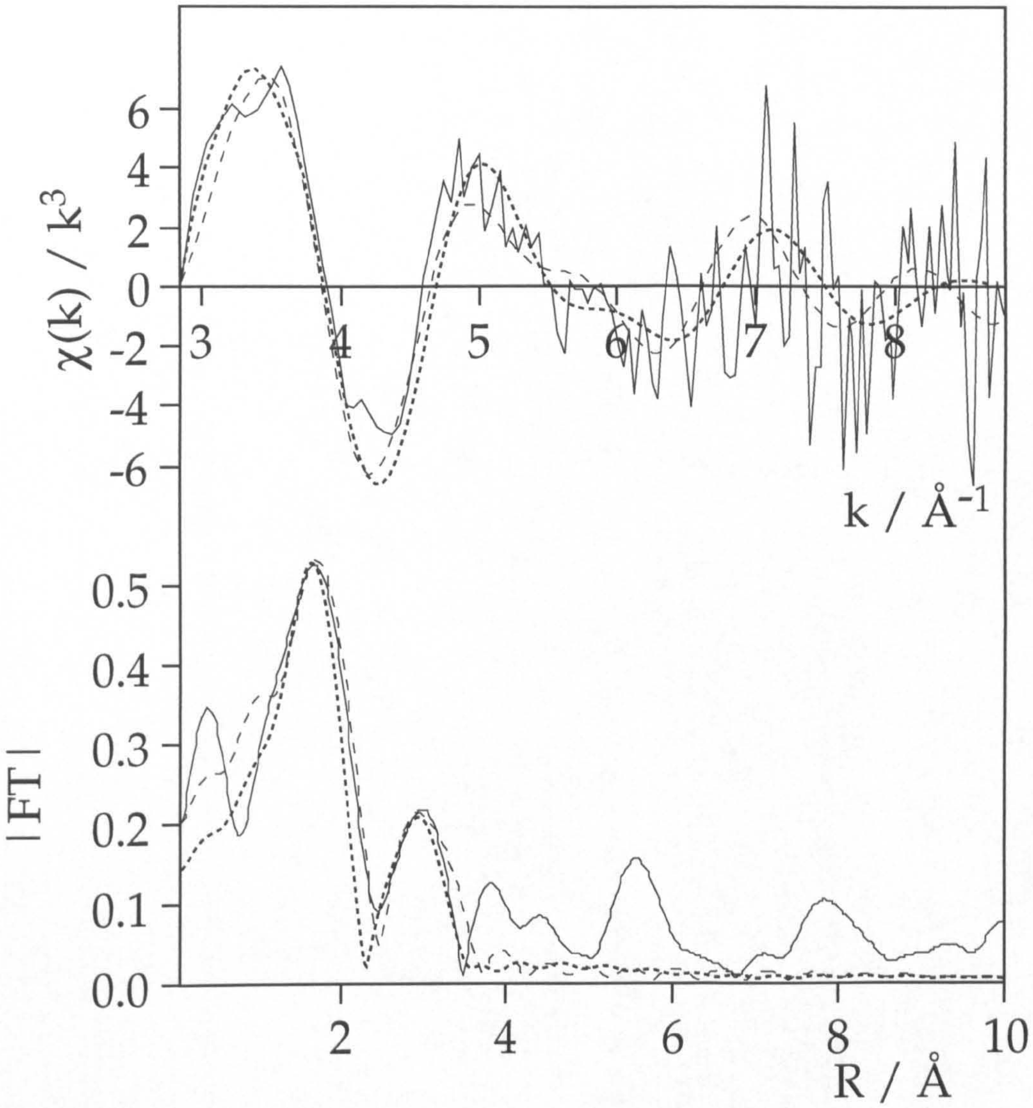

Figure 5.8 Ti K-edge SEXAFS spectrum and corresponding Fourier transform of 0.25 ML Ti deposited on α-quartz (0001) (1x1) at 298 K after background subtraction conversion to k space and weighting to k^3. The data was recorded at 20° incidence angle (solid line). Shown are the theoretical fits with the intercalation model (dashed line) and the surface rection model (dotted line). The spectra were recorded with the **E** vector parallel to the $[10\bar{1}0]$ azimuth.

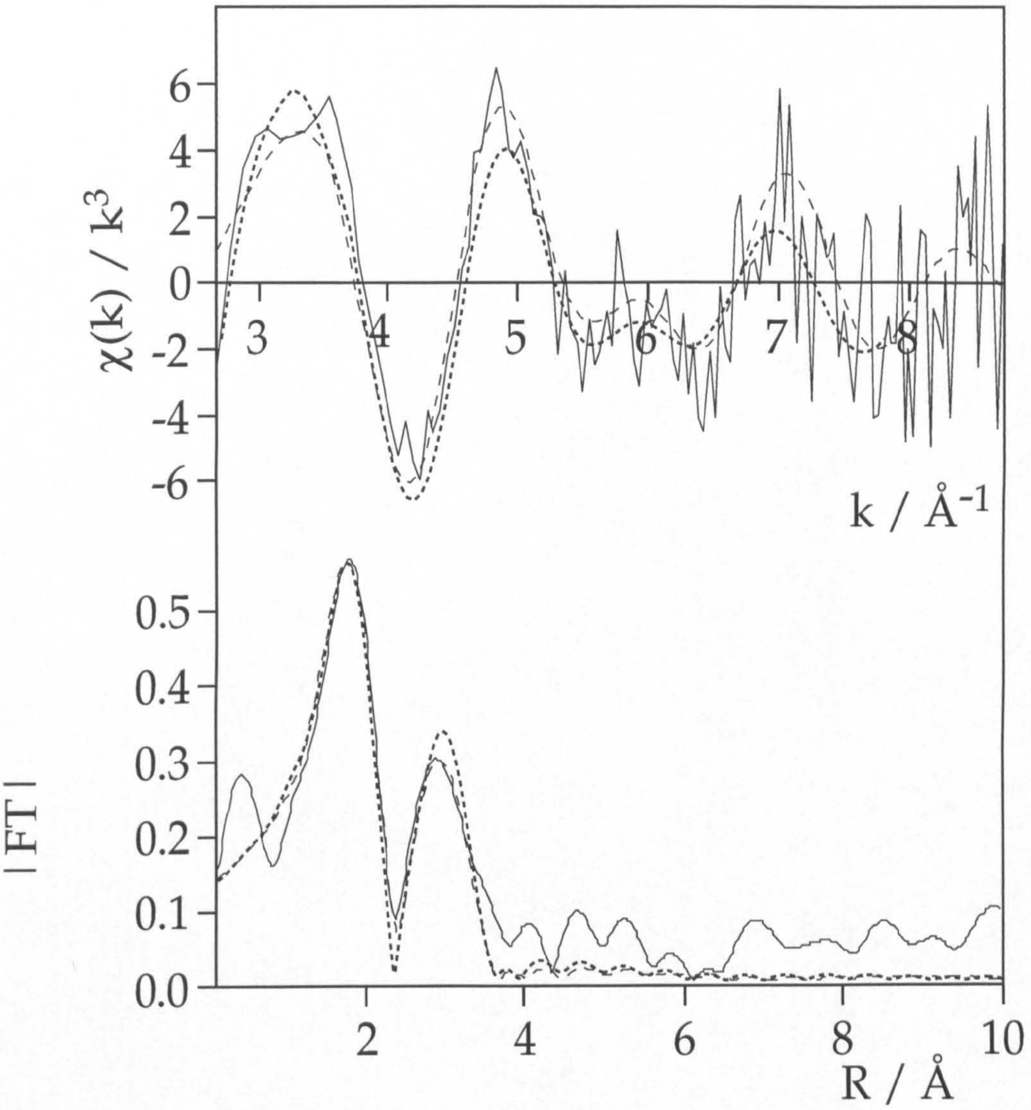

Figure 5.9 Ti K-edge SEXAFS spectrum and corresponding Fourier transform of 0.5 ML Ti deposited on α-quartz (0001) (1x1) at 298 K after background subtraction conversion to k space and weighting to k^3. The data was recorded at 20° incidence angle (solid line). Shown are the theoretical fits with the intercalation model (dashed line) and the surface rection model (dotted line). The spectra were recorded with the **E** vector parallel to the $[10\bar{1}0]$ azimuth.

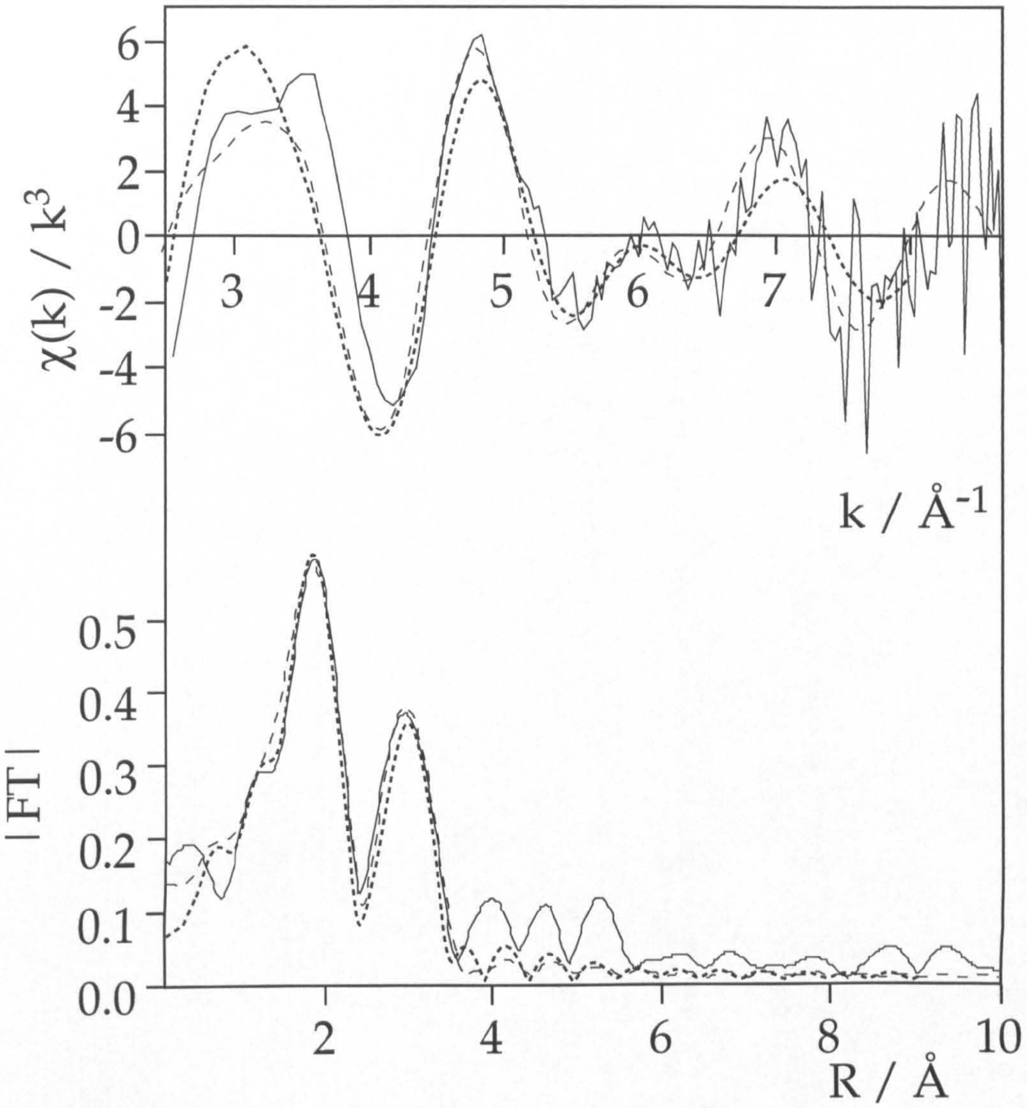

Figure 5.10 Ti K-edge SEXAFS spectrum and corresponding Fourier transform of 1.0 ML Ti deposited on α-quartz (0001) (1x1) at 298 K after background subtraction conversion to k space and weighting to k^3. The data was recorded at 20° incidence angle (solid line). Shown are the theoretical fits with the intercalation model (dashed line) and the surface rection model (dotted line). The spectra were recorded with the **E** vector parallel to the $[10\bar{1}0]$ azimuth.

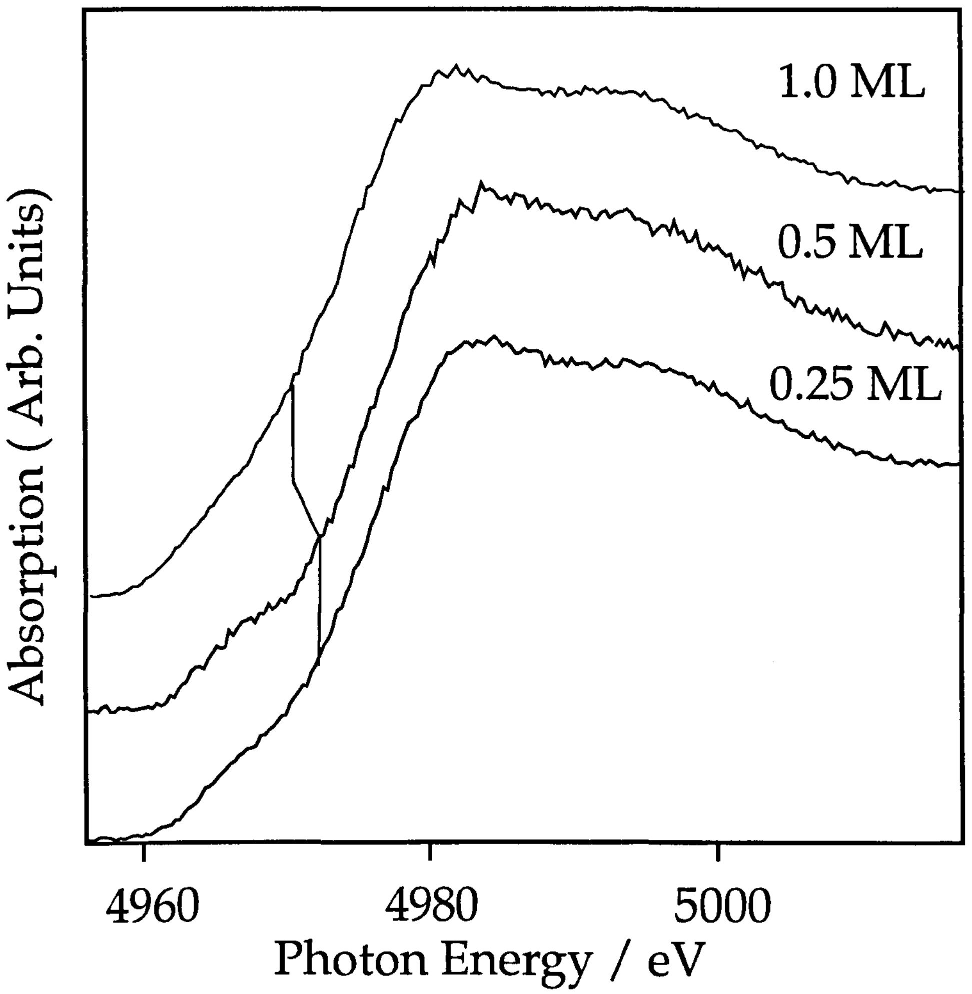

Figure 5.11 Ti K-edge XANES recorded from Ti on α-quartz (0001) (1x1) at 298 K recorded at 0.25, 0.5 and 1.0 ML nominal Ti coverages.

Ti - Ti coordination number accordingly. The value of six for the Ti - O coordination number was chosen as it is the bulk coordination number of Ti in both anatase and rutile structures and the derived bond distances are close to those of anatase and rutile (See below). This correction allows a semi-quantitative analysis of Ti cluster size to be performed at all coverages.

Further to this only one backscatterer type can be represented as a truly phase corrected shell. The radial distances as observed in the Fourier transform of any subsequent backscattering atom types will be subject to a slight error.[29,30]

The Ti - Ti coordination number varies a large amount between 0.25 ML and 0.5 ML Ti coverages with a value of 2.5±1.5 and 3.4±1.4 respectively increasing to 5.7±1.8 at 1.0 ML coverage. The data being shown in Figures 5.5, 5.6 and 5.7.

The corrected coordination number cannot be calculated for 0.25 ML Ti as the Ti - O coordination number is 6.6±1.2. However the corrected Ti - Ti coordination numbers for 0.5 ML being in the range 4.1 to 28.7 and for 1.0 ML 12.3 to 355.

Clearly the upper coordination numbers are unphysical, however the in the 0.5 ML case the lower value serves to place a lower limit on cluster size with an upper limit of bulk h.c.p. coordination number of 12. The 1.0 ML data exhibiting bulk h.c.p. coordination.

It is possible to make an estimate of the size of the Ti clusters if it is assumed that the lateral and vertical sizes of the particles are equal and the Ti assumes the bulk hexagonal close packed structure.[40] Using this formalism the lower limit of average cluster size can be estimated as 3.0±0.75 atoms in diameter at 0.5 ML Ti coverage. It should however be noted that this treatment ignores the effects of anharmonicity exhibited by edge atoms which results in an underestimation of coordination numbers and therefore cluster sizes, these effects being exacerbated by the use of a high power of k-weighting during the fitting procedure.[41,42] This treatment oversimplifies the effects of surface wetting known to be of importance in the adsorption of highly reactive metals upon oxide surfaces.[5] The Ti - Ti first shell distance is consistent over all three coverages and remains close to the bulk value of 2.89 Å.

The Ti - O distances vary only slightly between all three coverages being 2.00±0.03 Å at 0.25 ML, 1.96±0.03 Å at 0.5 ML and increasing slightly to 2.00±0.03 Å at 1.0 ML. These distances are consistent with both a rutile structure, which has Ti - O distances of 1.944 Å and 1.988 Å, and the anatase structure, which has Ti - O distances of 1.937 Å and 1.964 Å.[43] It should be noted that the Ti - O distances obtained here are the same for both the Si containing or non-Si containing models.

Coverage / ML	Si Model R-Factor	No Si Model R-Factor
0.25	53.42	61.83
0.5	50.81	56.28
1.0	40.75	49.54

Table 5.4 Least squared R-factor for intercalation model (Si) and surface reaction model (No Si) of Ti on α-quartz (0001)

In the case of the Si containing model the Ti - Si distance remains constant at 2.36±0.03 Å at all coverages. It is significantly different from the bulk $TiSi_2$ distances of 2.54 Å and 2.75 Å[43] and also from the C49 TiSi phase, 2.63 Å.[41]

Figure 5.11 shows the Ti K-edge XANES recorded at 298 K which exhibits a 2.4 eV shift in the edge position from 4972.4 eV at 0.25 ML and 0.5 ML coverages to 4970.0 eV at 1.0 ML coverage. Allied with this is the suppression of the pre-edge

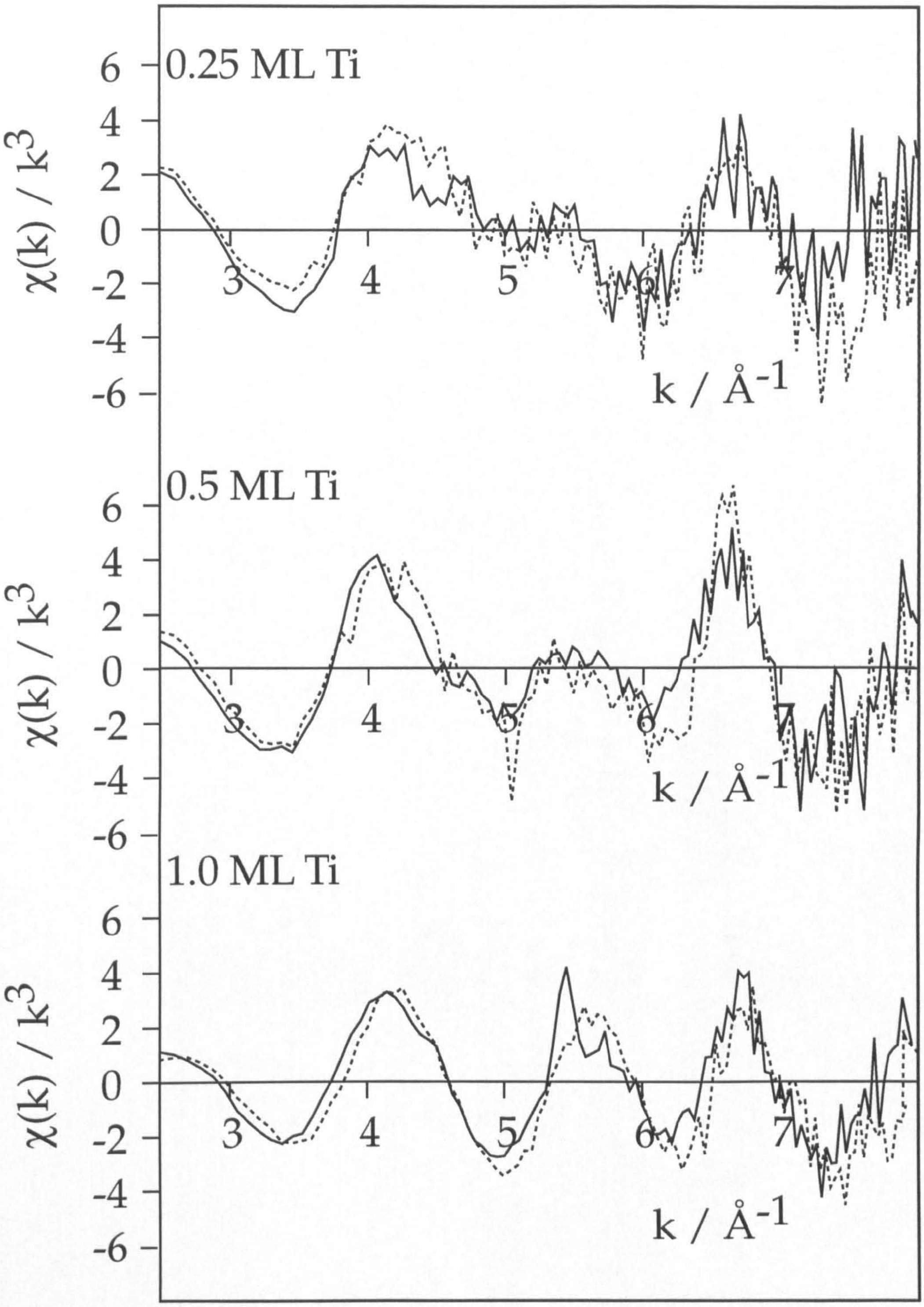

Figure 5.12 Ti K-edge SEXAFS from Ti adsorbed upon α-quartz (0001) $(\sqrt{84}\mathrm{x}\sqrt{84})\mathrm{R}11^{\circ}$ after background subtraction and weighting to k^3.

Shown are both near normal incidence (solid lines) and grazing incidence (broken lines) spectra. The nominal coverages are indicated.

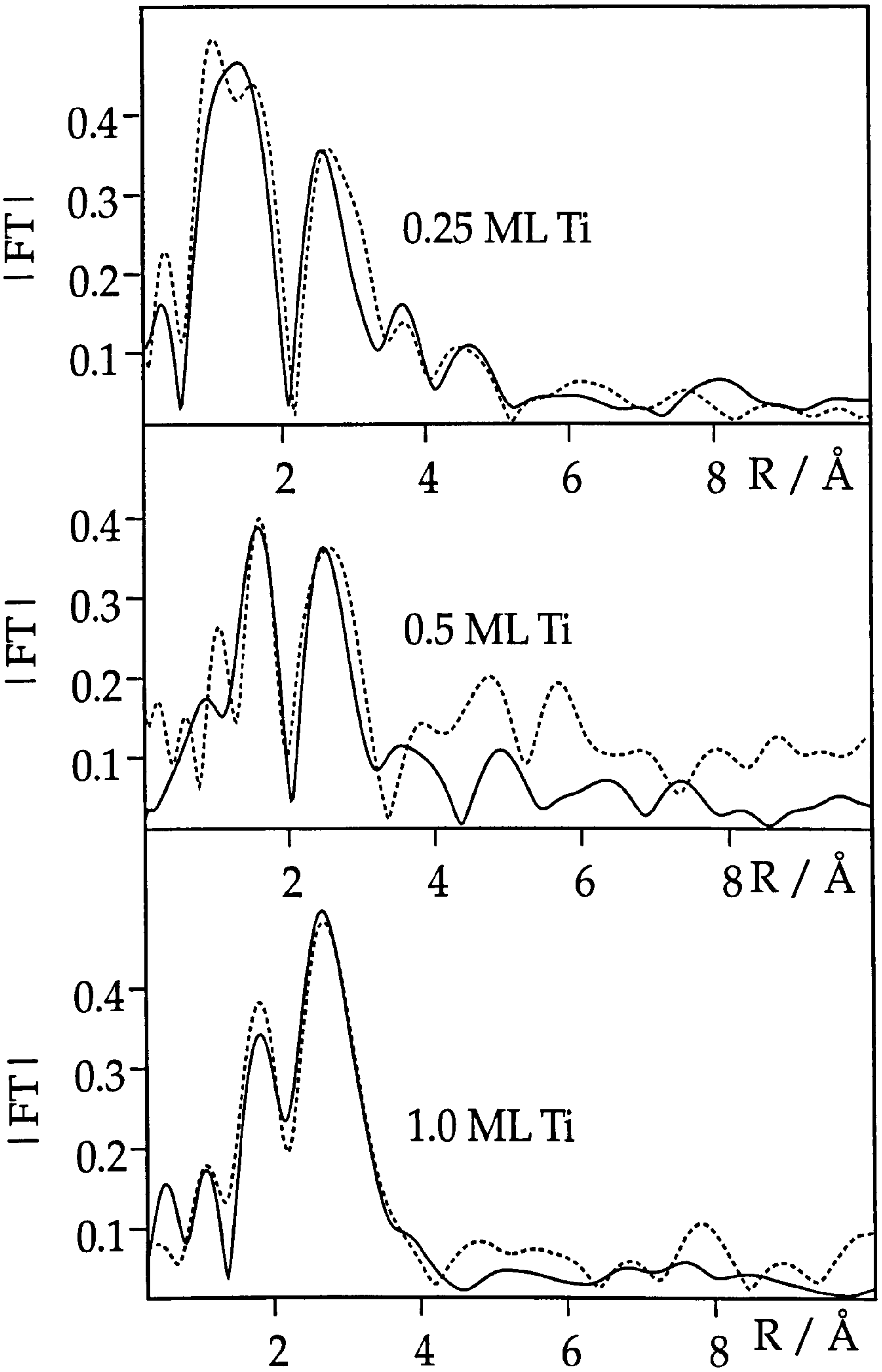

Figure 5.13 Fourier transforms of SEXAFS, shown in Figure 5.12, from Ti adsorption upon α-quartz (0001) ($\sqrt{84}$x$\sqrt{84}$) R11° , shown are both near normal incidence (solid lines) and grazing incidence (broken lines) spectra. Nominal coverages are indicated.

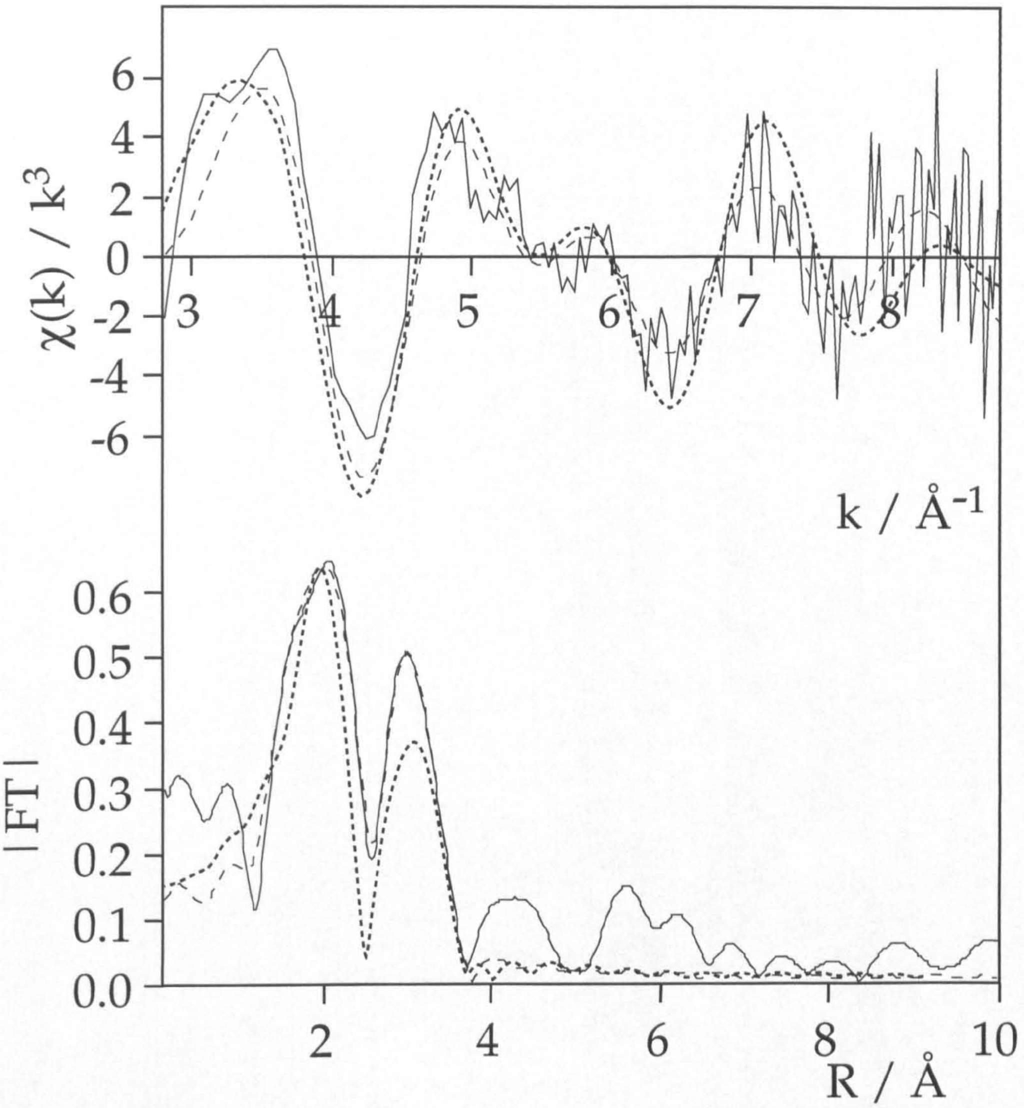

Figure 5.14 Ti K-edge SEXAFS spectrum and corresponding Fourier transform of 0.25 ML Ti deposited on α-quartz (0001) (1x1) at 298 K after background subtraction, conversion to k space and weighting to k^3. The data were recorded at 20° incidence angle (solid line). Shown are the theoretical fits with the intercalation model (dashed line) and the surface reaction model (dotted line). The spectrum was recorded with the **E** vector parallel to the $[10\bar{1}0]$ azimuth.

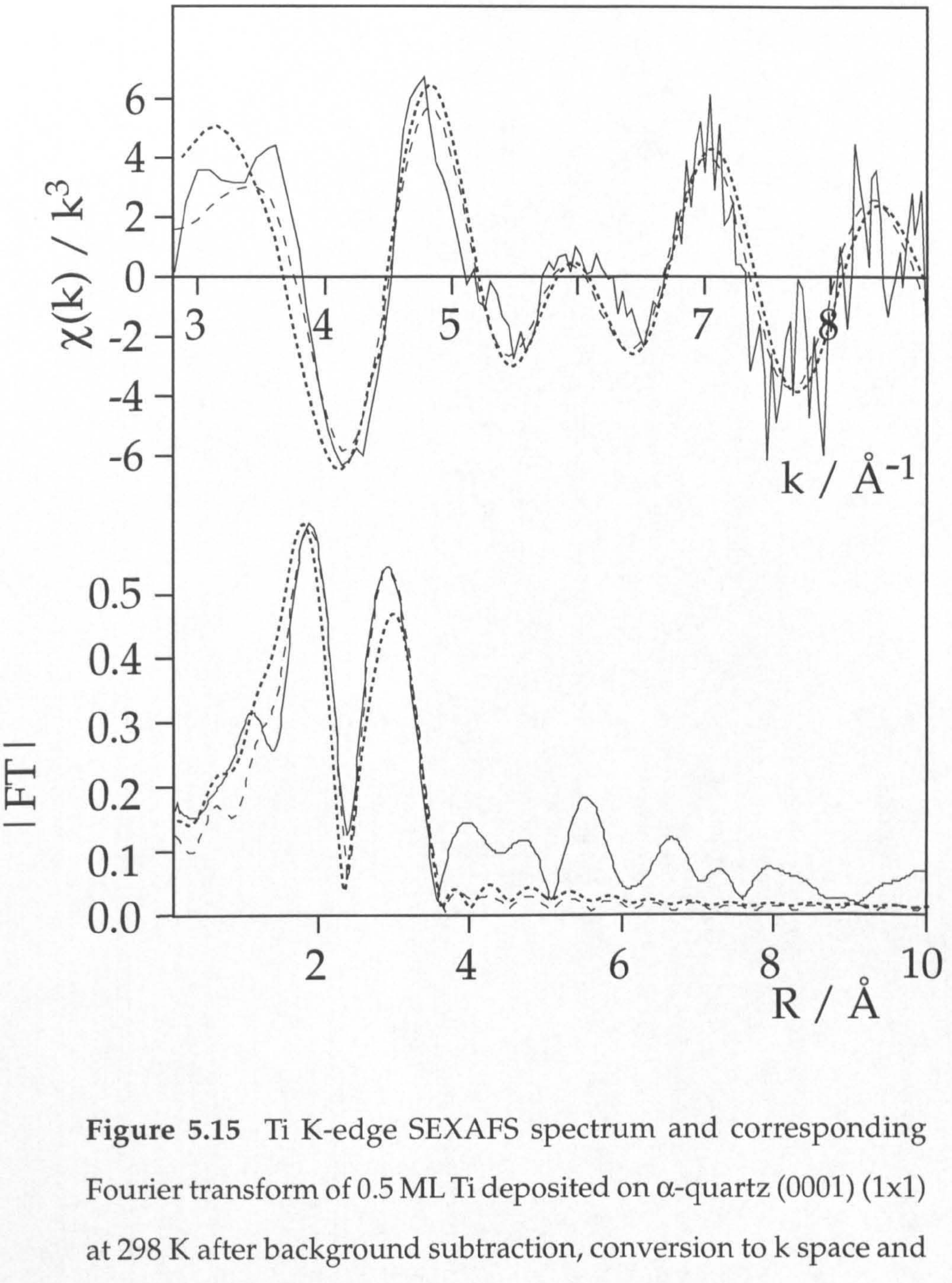

Figure 5.15 Ti K-edge SEXAFS spectrum and corresponding Fourier transform of 0.5 ML Ti deposited on α-quartz (0001) (1x1) at 298 K after background subtraction, conversion to k space and weighting to k^3. The data were recorded at 20° incidence angle (solid line). Shown are the theoretical fits with the intercalation model (dashed line) and the surface reaction model (dotted line). The spectrum was recorded with the **E** vector parallel to the $[10\bar{1}0]$ azimuth.

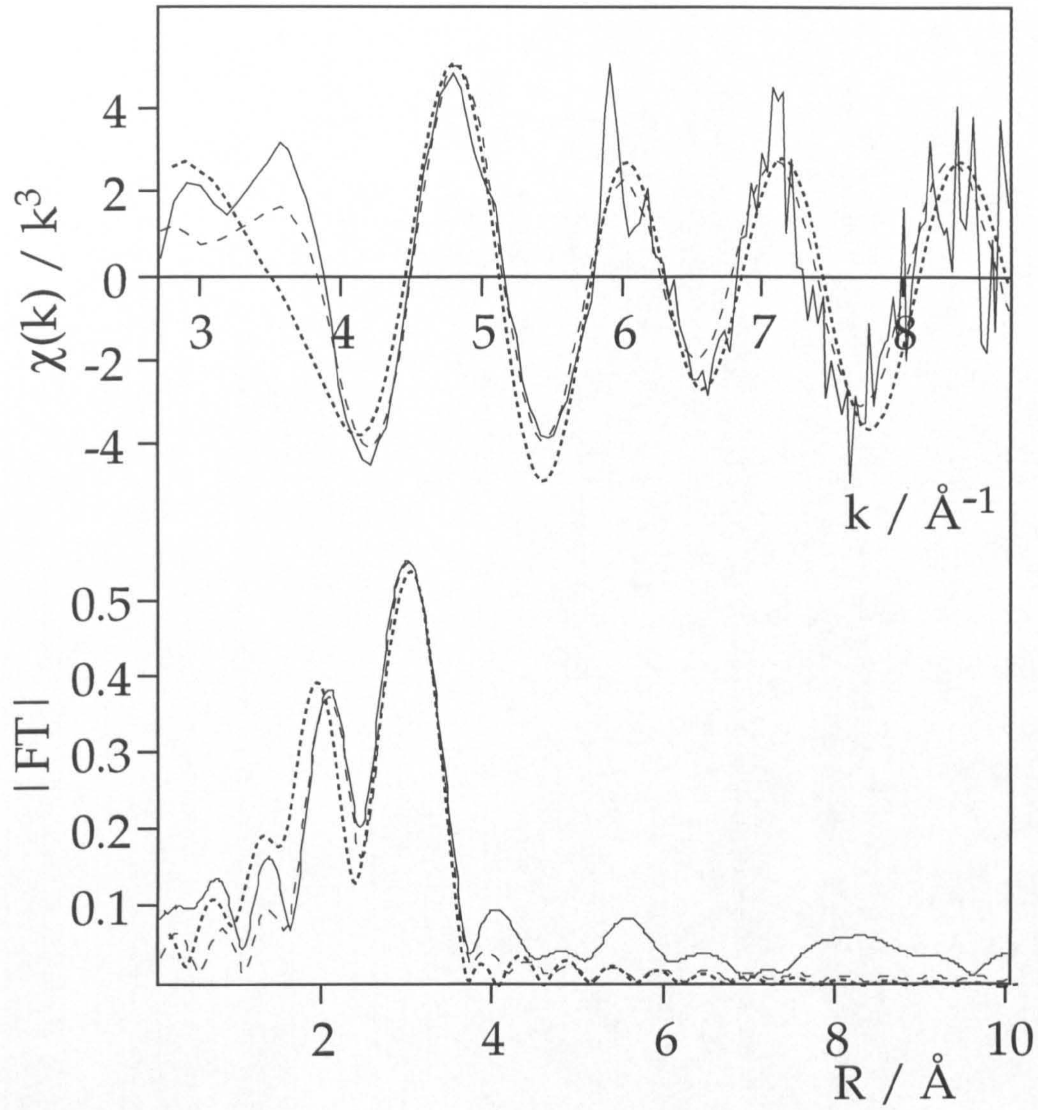

Figure 5.16 Ti K-edge SEXAFS spectrum and corresponding Fourier transform of 1.0 ML Ti deposited on α-quartz (0001) (1x1) at 298 K after background subtraction, conversion to k space and weighting to k^3. The data were recorded at 20° incidence angle (solid line). Shown are the theoretical fits with the intercalation model (dashed line) and the surface reaction model (dotted line). The spectrum was recorded with the **E** vector parallel to the $[10\bar{1}0]$ azimuth.

Coverage / ML	Si Model χ^2/x10^{-6}	No Si Model χ^2/x10^{-6}
0.25	71.74	61.09
0.5	100.00	46.91
1.0	58.50	43.94

Table 5.5 χ^2 Quality of fit index for intercalation (Si) model and surface reaction (No Si) model on $(\sqrt{84}\mathrm{x}\sqrt{84})$ R11° surface.

Coverage /ML	Atom Type	Coordination Number	Radius /Å ± 0.03 Å
0.25	O Ti	6.6±1.0 2.6±1.2	1.92 2.91
0.5	O Ti	4.3±0.9 8.3±1.2	1.98 2.89
1.0	O Ti	3.1±0.5 6.8±0.6	2.04 2.87

Table 5.6 Best fit parameters for $(\sqrt{84}\mathrm{x}\sqrt{84})$ R11° surface.

feature at 4965 eV with increasing coverage. This is consistent with the formation of a TiO_x film at low coverages and the subsequent deposition of metallic Ti upon this film.[40]

5.3.2 Ti adsorption on α-quartz (0001) $(\sqrt{84}\mathrm{x}\sqrt{84})$ R11°

The lack of polar angular dependence of the SEXAFS evidenced for Ti adsorption

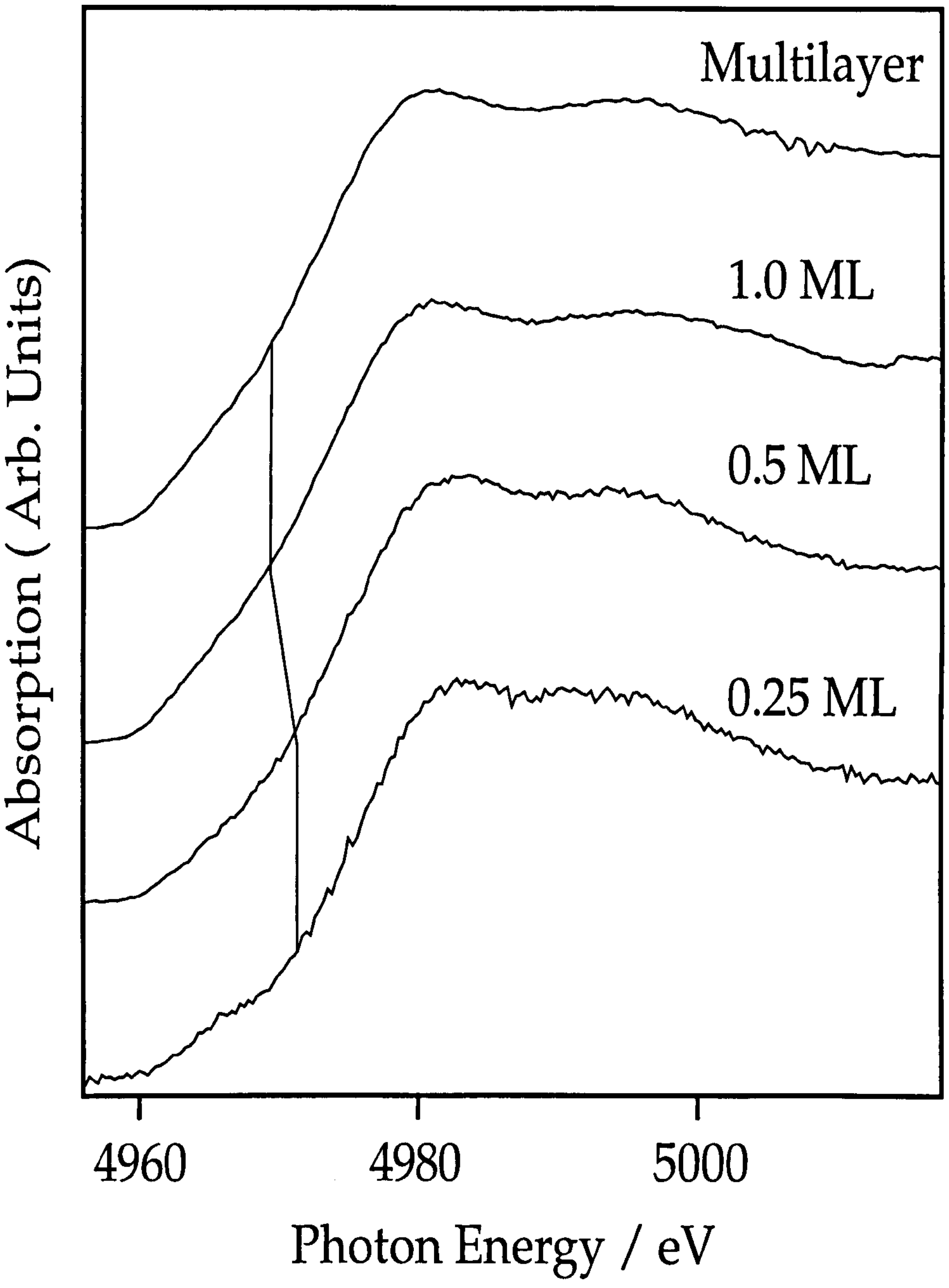

Figure 5.17 Ti K-edge XANES recorded from Ti on α-quartz (0001) ($\sqrt{84}$x$\sqrt{84}$) R11° at 298 K recorded at 0.25, 0.5 and 1.0 ML nominal Ti coverages.

upon the (1x1) surface is again evident for the $(\sqrt{84}\times\sqrt{84})\,R11^{\circ}$ reconstruction, as shown by the similarity of the near normal and grazing incidence data sets shown in Figures 5.12 and 5.13.

Figures 5.14, 5.15 and 5.16 show the background subtracted SEXAFS spectra recorded from Ti on the $(\sqrt{84}\times\sqrt{84})\,R11^{\circ}$ reconstruction, weighted to k^3 at 0.25±0.08, 0.5±0.16 and 1.0±0.33 ML Ti coverages.

For the $(\sqrt{84}\times\sqrt{84})\,R11^{\circ}$ surface there was no polar angular dependence evidenced as with the (1x1) case, inferring a significant spatially extensive interfacial region with a high degree of disorder, and only near normal incidence spectra, recorded at $\theta_i = 20^{\circ}$, are shown.

Table 5.4 shows the R-factors for both the intercalated Ti and surface reaction models with the intercalated Ti model having a lower R-factor at all three coverages. The χ^2 values are shown in Table 5.5. While the values of the two models for the 0.25 ML coverage are similar, at 0.5 ML and 1.0 ML the surface reaction model has significantly lower χ^2 values than the intercalation model implying that this model best describes the interactions within the system. Table 5.6 shows the best fit parameters for the fits shown in Figures 5.14, 5.15 and 5.16.

The corrected Ti - Ti coordination number for 0.25 ML Ti again cannot be derived. However for the 0.5 ML Ti coverage the corrected coordination number lies in the range 7.1 to 38.2 and in the 1.0 ML Ti case the corrected coordination numbers are within the range 11.9 to 18.5.
The lower limit on cluster size imposed by the lower limit to the coordination number for 0.5 ML Ti coverage yields a limiting average cluster size of 5.5±0.5 atoms, with the 1.0 ML case exhibiting a bulk h.c.p. coordination number.

The 0.25 ML Ti coverage results in a Ti -O radial distance of 1.92±0.03 Å. Due to the lack of polarisation dependence this is, as in the (1x1) case, indicative of a spatially extensive interfacial region. A coverage of 0.5 ML results in an Ti - O bond distance of 1.98±0.03 Å. A further increase in Ti coverage to 1 ML results in an increase in the Ti - O distance to 2.01±0.03 Å.

The XANES from the $(\sqrt{84}\mathrm{x}\sqrt{84})$ R11° (0001) SiO_2 / Ti system is shown in Figure 5.17 and shows evidence of a pre-edge feature at 4965 eV in the 0.25 ML Ti coverage data which becomes less evident with increasing Ti coverage. Further to this there is a shift of the edge position of approximately 2.4 eV from 4971.3 eV at 0.5 ML to 4968.9 eV at 1 ML Ti coverage. This movement of the edge position indicates a more metallic overlayer at higher coverages.[40]

5.4 DISCUSSION

The lack of polar angular dependence in the SEXAFS indicates the existence of a spatially extensive interfacial region. This interfacial region may be due to the interpenetration of Ti atoms into the quartz lattice, the formation of a TiO_x overlayer or a combination of both effects. The nature of the Ti - Ti interaction is highly indicative of the simultaneous formation of mesoscopic particulate formation.

5.4.1 General Considerations of TiO_x Formation

When considering the nature of the interfacial region between reactive metals and oxide substrates it is convenient to consider the thermodynamic properties of the interface in terms of the surface free energies of the substrate and the adsorbate species. The interfacial energy must also be accounted for,[5,6,7] the principal components of which are the relative enthalpies of the adsorbate oxygen bond and the substrate oxygen bond.

The formation of the oxide layer is entirely consistent with the thermodynamic

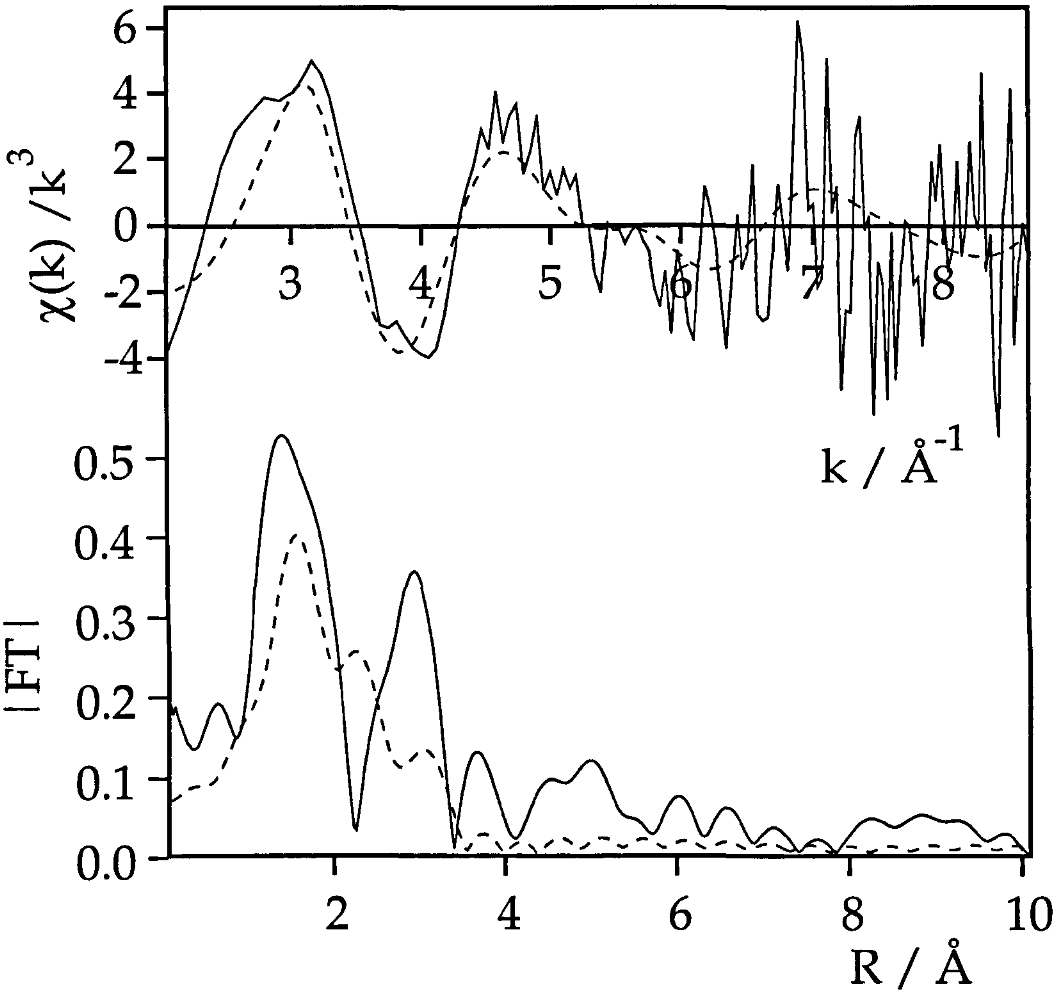

Figure 5.18 Comparison of experimentally recorded Ti K-edge SEXAFS spectrum of 0.25 ML Ti on α-quartz (0001) (1x1) after background substraction , conversion to k-space and weighting to k^3 with EXAFS simulation of single Ti atom placed in centre of quartz bulk unit cell.

stability of the Si - O bond versus the Ti - O bond. The Si - O bond has an associated bond energy of 4.5 eV [45] while the Ti - O bond being more stable with a bond energy of 5.2 eV.[45] On this basis the reaction of the substrate bound oxygen with adsorbed titanium would be expected. In addition to this is the reduction of free surface energy of Ti upon oxidation from 2.570 Jm^{-2} [46] for the polycrystalline metal to 0.279 - 0.379 Jm^{-2} [47] for the oxide, TiO_2, which would further favour the formation of an oxide film. The free surface energy of TiO_x, assuming it to be similar to that of TiO_2, is also significantly less than that of SiO_2 0.604 Jm^{-2}.[47] The formation of TiO_x would most likely continue if there was a ready supply of oxygen as in the reaction of Ti with TiO_2 which has been seen to result in the formation of 12 Å thick oxide layer after the deposition of 4 Å of Ti.[8] This is due to the high diffusivity of oxygen through the TiO_2 lattice, $d=2.77\times10^{-11}$ m^2s^{-1} (348 K).[11] The diffusivity of oxygen through a vitreous quartz lattice is, however, much smaller, being less than 10^{-21} m^2s^{-1} (298 K),[48] and therefore oxide formation is limited to the immediate interfacial region.

It has been shown[49] that SiO_2 spontaneously hydroxylates under normal atmospheric conditions. It is therefore possible, considering the preparative method employed,[24] that both the reconstructions studied will be hydroxylated. The bond energy of an SiO - H bond has been shown to be 3.4 eV,[50] this is considerably less than the 5.2 eV bond energy associated with the formation of a Ti - O bond and therefore displacement of hydrogen by Ti could be expected to occur. Therefore the presence of a hydroxylated surface would not greatly inhibit reaction of deposited Ti with surface oxygen.

5.4.2 Ti / SiO_2 (0001) (1x1)

Further to the purely statistical consideration of the two models under consideration, a simulation of the intercalation of Ti into the centre of a quartz unit cell is shown in Figure 5.18. This shows the similarity of the 0.25 ML data to this model, however it must be noted that there is a peak at 2.28 Å in the Fourier transform of the model not present in the experimental data. This arises from backscattering from one of the three Si atoms within the quartz unit cell.

The Ti - O distances at all three coverages are extremely close to both the major coordination sphere anatase Ti - O distance, 1.93 Å, and the rutile, 1.95 Å distance. The variation in bond length may be due to the formation of a disordered TiO_x overlayer from the direct reaction of Ti with O as discussed earlier. These changes in bond length are consistent with trends developed in work showing chemical disorder in ion bombarded TiO_x films.[53]

The Ti - O distances are also similar to the Ti - O distance, 1.95 Å, in a bulk sample of Ti containing zeolite-Y,[54] where the catalytic activity is ascribed to the reducibility of the rutile-like particles.

The size of the mesoscopic Ti particles, at 0.5 ML coverages, of 3.5 atoms corresponds to a mean particle radius of 5.0 Å, effectively metallic dimers. At 1.0 ML this becomes a mean radius of 11 Å with a particle size of 5 atoms. Another possible explanation of the reduced Ti - Ti coordination number is Ti residing in environments where it does not contribute coherently to the EXAFS. The possibility of Ti existing in the b.c.c. β phase can be discounted as the nearest neighbour distance in the β phase is 2.33 Å compared to the 2.89 Å seen here.

It can be suggested from this that a reaction with surface oxygen is occurring and there is insufficient driving force for the disruption of the underlying lattice structure to allow the intercalation of titanium into the interstices.

The formation of three dimensional particles even at the lowest, 0.25 ML, titanium coverage is consistent with a very low localised critical coverage[55] in those regions where reduction of the surface by deposited titanium has taken place.

This is supported by the movement of the XANES Ti K-edge position in Figure 5.11 as coverage is increased emphasising the increasingly metallic nature of the titanium overlayer. The limiting factor in the extraction of further information from the XANES is the resolution of the double crystal monochromator Ge(111) crystal pair being 2.9 eV at the Ti K-edge (4966 eV).

5.4.3 Ti / SiO_2(0001) $(\sqrt{84}\mathrm{x}\sqrt{84})$ R11°

The increased bulk like corrected coordination number of Ti upon the $(\sqrt{84}\mathrm{x}\sqrt{84})$ R11° reconstruction at 0.5 ML Ti coverage compared to those on the (1x1) surface is reminiscent of the behaviour of copper adsorption on alumina substrates[56,57] in which reduced substrates result in a larger cluster size than oxidised substrates. There is however no direct evidence to support an oxygen deficient model for the $(\sqrt{84}\mathrm{x}\sqrt{84})$ R11° reconstructed α-quartz surface. Another possible hypothesis arises from the nature of the Dauphiné twin structure. This forms the reconstruction via the reduction in symmetry of the surface unit cell to a ternary symmetry from the bulk hexagonal symmetry. Upon cooling through the α - β phase transition there is a misorientation between the surface unit cell and the crystallographic {100} axes introduced.[24] This may result in a more highly ordered surface than the (1x1) and the additional disorder in the (1x1) case may prevent formation of bulk like Ti overlayers.

Ti K-edge XANES data shown in Figure 5.17 obtained from Ti on SiO_2(0001) $(\sqrt{84}\mathrm{x}\sqrt{84})$ R11° show again that a pre-edge feature observed in titanium oxides and oxidised Ti films at 4965 eV,[40] reduces in intensity with increasing coverage. Coupled with this is the reduced energy of the edge position indicating a more metallic like overlayer with increasing coverage.

5.5 Conclusion

The possibility of Ti intercalation into the α-quartz lattice is considered but rejected as it does not result in a statistically significant increase in fit quality which is acceptable over a model in which a direct reaction between surface oxygen and titanium occurs.

Titanium vapour deposition upon both the known stable terminations of the SiO_2 (0001) proceeds via the formation of TiO_x surface layer, with Ti - O distances close to those in both anatase and rutile. Coupled with this in the (1x1) case is formation of three dimensional mesoscopic Ti particles with a bulk or near bulk interatomic spacing. For both the (1x1) and the $(\sqrt{84}\times\sqrt{84})\,R11^\circ$ case a bulk like Ti overlayer is seen to form at coverages in excess of 0.5 ML.

In both the (1x1) and the $(\sqrt{84}\times\sqrt{84})\,R11^\circ$ reconstruction cases Ti K-edge XANES show a change from a predominantly oxidised Ti species to a metallic like species between 0.5 ML and 1.0 ML Ti coverages.

References

1. K. Armstrong, Applied Materials HP PVD Update, **2**, 4, (1995)

2. R.B. Byers, Ph.D. Thesis, Stanford University, California, United States of America, (1989)

3. C.E. Marsden in "Preparation of Catalysts V", pp. 215-227, G. Poncelet, P.A. Jacobs, P. Grange and B. Delmon eds., Elsevier Science Publishers B.V., Amsterdam, 1991.

4. J.-M. Pan and T.E. Madey, J. Vac. Sci. Technol., **A11**, 1667, (1993)

5. U. Diebold, J.-M. Pan and T.E. Madey, Surf. Sci., **287/288**, 896, (1993)

6. U. Diebold, J.-M. Pan and T.E. Madey, Surf. Sci., **331-333**, 845, (1995)

7. J.-M. Pan and T.E. Madey, Surf. Sci., **295**, 411, (1993)

8. J.T. Mayer, U. Diebold, T.E. Madey and E. Garfunkel, J. Electron Spectrosc. Relat. Phenom., **73**, 1, (1995)

9. U. Diebold, J.-M. Pan and T.E. Madey, Phys. Rev. B, **47**, 3868, (1993)

10. Z. Zhang and V.E. Henrich, Surf. Sci., **277**, 263, (1992)

11. G. Rocker and W. Göpel, Surf. Sci., **181**, 530, (1987)

12. Y.-M. Sun, D.N. Belton and J.M. White, J. Phys. Chem., **90**, 5178, (1986)

13. H.-P. Steinrück, F. Pesty, L. Zhang and T.E. Madey, Phys. Rev. B, **51**, 2427, (1995)

14. S. Iida and S. Abe, Appl. Surf. Sci., **78**, 141, (1994)

15. M.A. Taubenblatt and C.R. Helms, J. Appl. Phys., **53**, 6308, (1982)

16. J.T. Mayer, R.F. Lin, and E. Garfunkel, Surf. Sci., **265**, 102, (1992)

17. M. Liehr, F.K. LeGoues, G.W. Rubloff and P.S. Ho, J. Vac. Sci. Technol., **A3**, 983, (1985)

18. R. Butz, G.W. Rubloff and P.S. Ho, J. Vac. Sci. Technol., **A1**, 771, (1983)

19. A.A. Schmidt, H. Eggers, K. Herwig and R. Anton, Surf. Sci., **349**, 301, (1996)

20. S.K. Saha, H. Jain, A.C. Miller and R.K. Brown, Surf. Interface Analysis, **24**, 113, (1996)

21. X. Wallart, H.S. Zeng, J.P. Nys, G. Dalmai and P. Friedel, J. Appl. Phys., **69**, 8168, (1991)

22. Charging Effects in Electron Spectroscopies, Special Issue of J. Electron

Spectrosc. Relat. Phenom., **59**, (1992)

23. F. Bart, M.J. Guittet, M. Henriot, N. Thromat, M. Gautier and J.P. Duraud, J. Electron Spectrosc. Relat. Phenom., **69**, 245, (1994)

24. F. Bart and M. Gautier, Surf. Sci. Lett., **311**, L671, (1994)

25. R.B. Sosman, "The Phases of Silica", Rutgers University Press, New Jersey, (1965)

26. J. Van Landuyt, G. Van Tendeloo, S. Amelinckx and M.B. Walker, Phys Rev. B, **31**, 2986, (1985)

27. A.W. Robinson, S. D'Addato, V.R. Dhanak, P. Finetti, and G. Thornton, Rev. Sci. Instrum., **66**, 1769, (1995).

28. F. Bart, M. Gautier, J.P. Duraud and M. Henriot, Surf. Sci., **274**, 317, (1992)

29. S.J. Gurman, N. Binsted, and I. Ross, J. Phys. C, **17**, 143, (1984)

30. S.J. Gurman, N. Binsted, and I. Ross, J. Phys. C, **19**, 1845, (1986)

31. N. Binsted and D. Norman, in: "The Structure of Surfaces IV", Eds. Xide Xie, S.Y. Tong and M.A. Van Hove (World Scientific, Singapore, 1994) p. 118

32. N. Binsted and D. Norman, Phys. Rev. B, **49**, 15531, (1994)

33. S.J. Gurman, J. Phys. C: Solid State Phys., **21**, 3699, (1988)

34. L. Hedin and S. Lundqvist, Solid State Phys., **23**, 1, (1969)

35. S. Ogawa and S. Ichikawa, Phys. Rev. B, **51**, 17231, (1995)

36. J. Stöhr in "Chemical Analysis Vol. 92, 'X-ray Absorption - Principles, Applications, Techniques of EXAFS, SEXAFS and XANES'", Eds. D.C. Koningsberger and R. Prins, Wiley Interscience, John Wiley and Sons Inc., London, (1988)

37. G. Bunker, D. Crozier, N. Binsted, Y. Ma, A. McKale, E.A. Stern, M. Vaarkamp and K. Zhang, Data Analysis Subgroup Report, International Workshops on Standards and Criteria in XAFS, X-Ray Absorption Fine Structure, Ed. S. Samar Hasnain, Ellis Horwood, London, (1991)

38. R.W. Joyner, K.J. Martin and P. Meehan, J. Phys. C-Solid State Phys., **20**, 4005, (1987).

39. E.A. Stern, Phys. Rev. B., **48**, 9825, (1993).

40. M.C. Asensio, M. Kerkar, D.P. Woodruff, A.V. de Carvalho, A. Fernández, A.R.

González-Elipe, M. Fernández-Garcia and J.C. Conesa, Surf. Sci., **273**, 31, (1992)

41. B.S. Clausen, H. Topsøe, L.B. Hansen, P. Stoltze and J. Nørskov, Jpn. J. Appl. Phys., **Suppl. 32 - 2**, 95, (1993)

42. B.S. Clausen, H. Topsøe, L.B. Hansen, P. Stoltze and J. Nørskov, Catalysis Today, **21**, 49, (1994)

43. A.F. Wells, "Structural Inorganic Chemistry", pp. 988 - 990, Oxford University Press, London, (1986)

44. A.M. Edwards, Y. Dao, R.J. Nemanich and D.E. Sayers, Jpn. J. Appl. Phys.,**Suppl. 32 - 2**, 393, (1993)

45. R.C. Weast Ed., CRC Handbook of Chemistry and Physics (1977-1978)

46. L.Z. Mezey and J. Giber, Jap. J. Appl. Phys., **21**, 1569, (1982)

47. S.H. Overbury, P.A. Bertrand and G.A. Somorjai, Chem. Rev., **75**, 547, (1975)

48. J.C. Mikkelsen Jr., Appl. Phys. Lett., **45**, 1187, (1984)

49. C. Noguera, J. Goniakowski and S. Bouette-Russo, Surf. Sci., **287/288**, 188, (1993)

50. A. Vittadini, A. Selloni and M. Casarin, Phys. Rev. B, **52**, 5885, (1995)

51. J.F. Hamilton, D.R. Preuss and G.R. Apai, Surf. Sci., **106**, 146, (1981)

52. P.A. Lee and G. Beni, Phys. Rev. B, **15**, 2862, (1977)

53. S. Bayliss, Private communication.

54. E. Scultz, C. Ferrini and R. Prins, Jap. J. Appl. Phys., **32 Suppl. 32-2**, 490, (1992)

55. C.T. Campbell, Surf. Sci. Rep., **27**, 1, (1997)

56. S. Gota, M. Gautier, L. Douillard, N. Thromat, J.P. Duraud and P. Le Fèvre, Surf. Sci., **323**, 163, (1995)

57. M. Gautier-Soyer, S. Gota, L. Douillard, J.P. Duraud and P. Le Fèvre, Phys. Rev. B., **54**, 10366, (1996)

Chapter 6

A SEXAFS study of Ni(110)-Sc(2x2)

6.1 Introduction

In principle, one can glean quite extensive knowledge about the local structure surrounding an absorber from the surface extended X-ray absorption fine structure (SEXAFS). Unfortunately, relatively poor statistics and short data ranges have generally restricted SEXAFS studies to details about nearest neighbour or at most next-nearest neighbour backscatterers. More recently, superior data, such as those obtained in a study of Cu(100)c(2x2)N,[1] have enabled a more complete analysis of the local structure. This has involved an evaluation of the multiple scattering contribution to the surface EXAFS, which is found to be important for coplanar, short-bond systems.[1] Here we present an analysis of SEXAFS data from a deeper core level (S 1s) to assess the influence of multiple scattering.

Ni(110)c(2x2)S is an archetypal adsorption system, having a well known surface structure in which S lies in the two fold hollow site.[2-8] A significant outward relaxation of the uppermost Ni layer accompanies adsorption. Previous analysis of SEXAFS data from this system[5-9] has been restricted to single scattering processes involving the four surface Ni atoms and the second layer Ni atom directly bonded to the S atom.

6.2 Experimental

The version of the EXCURV[10,11] programme employed for this analysis allows simultaneous fitting of up to three spectra recorded with inequivalent directions of the polarisation vector, leading to a self-consistent array of fitting parameters. The refinement procedure exploits the crystallographic symmetry of the data to increase the determinacy of the fitting parameters.[12] With our new analysis we re-examine the substrate relaxation[12] and consider more subtle structure variations such as rumpling of the Ni second layer atoms. Such a sub-surface rumpling of Ni(110)c(2x2)S was previously suggested on the basis of angle-resolved photoemission fine structure (ARPEFS) measurements.[4]

Sulphur K-edge (2472 eV) SEXAFS measurements were performed using a Ge(111) crystal pair in the double-crystal monochromator of station 4.2 at the SRS, Daresbury Laboratory.[13] Third order output from the monochromator was removed through the use of a combination of chromium coated and quartz mirrors.[14] A gas flow proportional counter[15] was used to record the S K_α fluorescence yield as a monitor of the surface X-ray absorption coefficient.

Normalisation of the SEXAFS data to the incident photon flux was accomplished by measuring the drain current from a thin Al foil placed between the monochromator and sample chamber. The chamber base pressure was below 2×10^{-10} mbar.

Preparation of Ni(110)c(2x2)S followed the method described by Warburton.[5] This involved the exposure of clean Ni(110) to 8 L (1 L = 1.32×10^{-6} mbar s) of H_2S at 293 K followed by flashing the sample to 415 K to desorb residual hydrogen. Sample cleanliness and order were checked with Auger spectroscopy and LEED. SEXAFS measurements were recorded at normal (90°) and grazing (20°) photon incidence. In the grazing incidence geometry the photon **E** vector was in the $[1\bar{1}0]$ azimuth whilst normal incidence spectra were recorded with the **E** vector in the $[1\bar{1}0]$ and [001] azimuths. During the SEXAFS measurements the sample temperature was maintained at about 95 K to reduce Debye-Waller-like attenuation of the SEXAFS amplitude. SEXAFS spectra recorded in the three experimental geometries described above are displayed in Figure 6.1. Background subtraction and normalisation of these spectra were performed with the programme PAXAS[16] in which one or two coupled polynomials of order 6 to 8 were used to approximate the atomic background above the S K-edge. Subtraction of the polynomial is believed to be valid above 2492 eV. This coincides

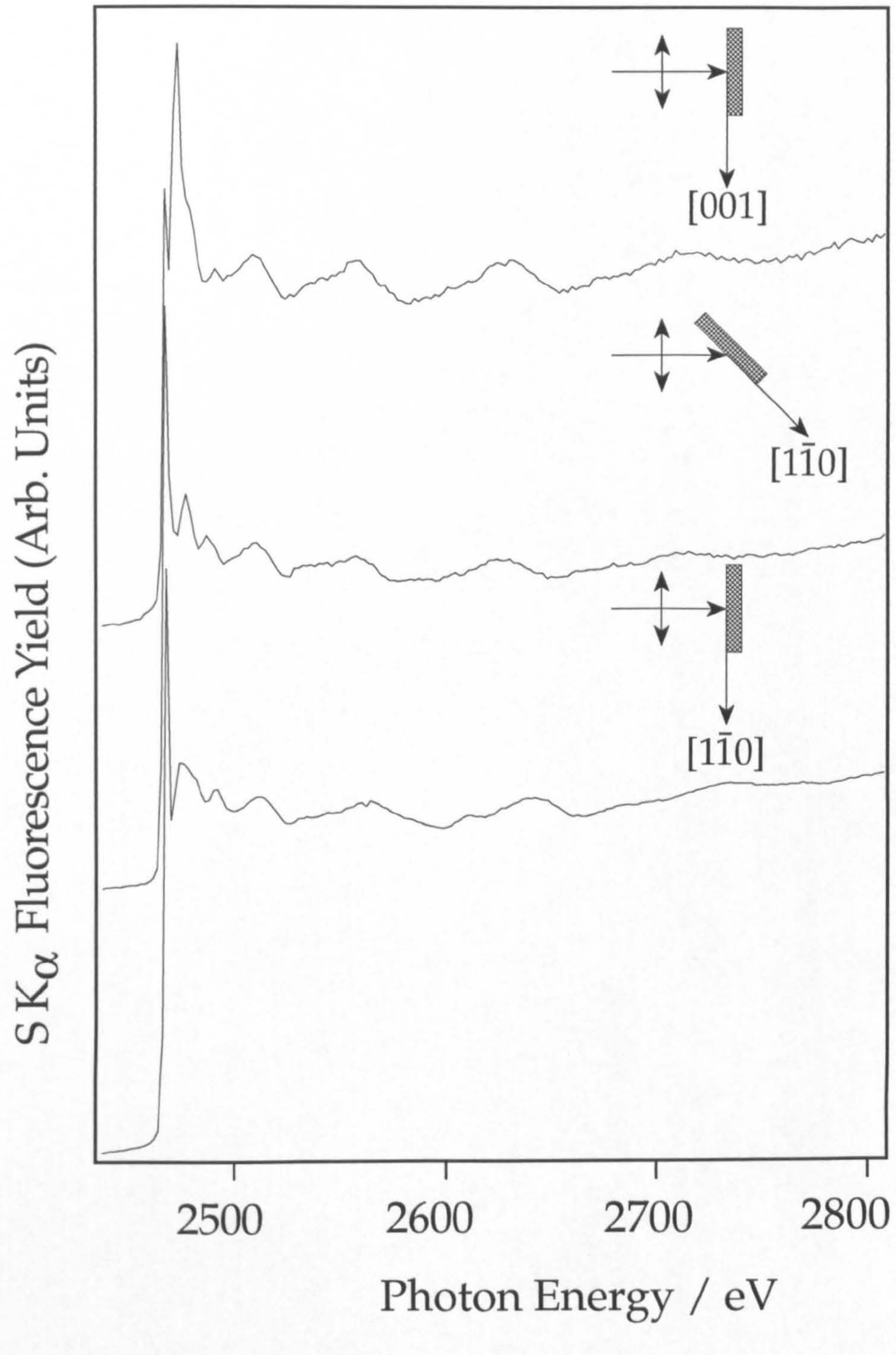

Figure 6.1 S K-edge SEXAFS spectra of Ni(110)c(2x2)S at 95 K. The spectra were recorded at an X-ray incidence angle of 90° with the **E** vector parallel to the [001] and $[1\bar{1}0]$ azimuths and at an incidence angle of 20° with the **E** vector in the $[1\bar{1}0]$ azimuth.

approximately with the energy beyond which the theoretical phase shifts used in this analysis have previously been shown to be adequate.[17]

The new code employed in this analysis utilises full spherical wave theory. It includes the small atom approximation to the polarisation-dependent angle factor, which breaks down only within about 30 eV of the edge.[17-19] Whilst the transferability of phase shifts is generally accepted, there has been an anomaly concerning the empirical derivation of S-Ni phase shifts.[20,21] This led to an incorrect distance for even the first shell, which has appeared typically 0.06 Å too short.[20] This problem is addressed here through the use of *ab initio* Hedin-Lundqvist potentials[22] to derive the S-Ni phase shifts rather than the use of reference-compound derived phase shifts. Thermal disorder for the single scattering case is dealt with by the integral of the configurational average including a phase correction term.[23] For multiple scattering a new treatment of disorder is used.[24] The number of possible multiple scattering paths is limited via the exclusion of all path lengths in excess of 15 Å and also the introduction of a minimum path amplitude below which scattering paths are discarded. The number of free parameters used in fitting is minimised to avoid statistical under-determinacy. The structural parameters varied during the fitting process were the first and second Ni layer distances, the individual Debye-Waller-like terms for the two nearest neighbour shells and other Debye-Waller-like terms grouped according to their local environment. The relative positions of the more distant atoms were fixed.

6.3 Results and Discussion

Figures 6.2, 6.3 and 6.4 shows the spectra derived from Figure 6.1, after background subtraction, conversion to k space and weighting by k, with the best fit obtained using either a single scattering formalism only or including multiple scattering up to third order. The first and second shell S-Ni bond distances

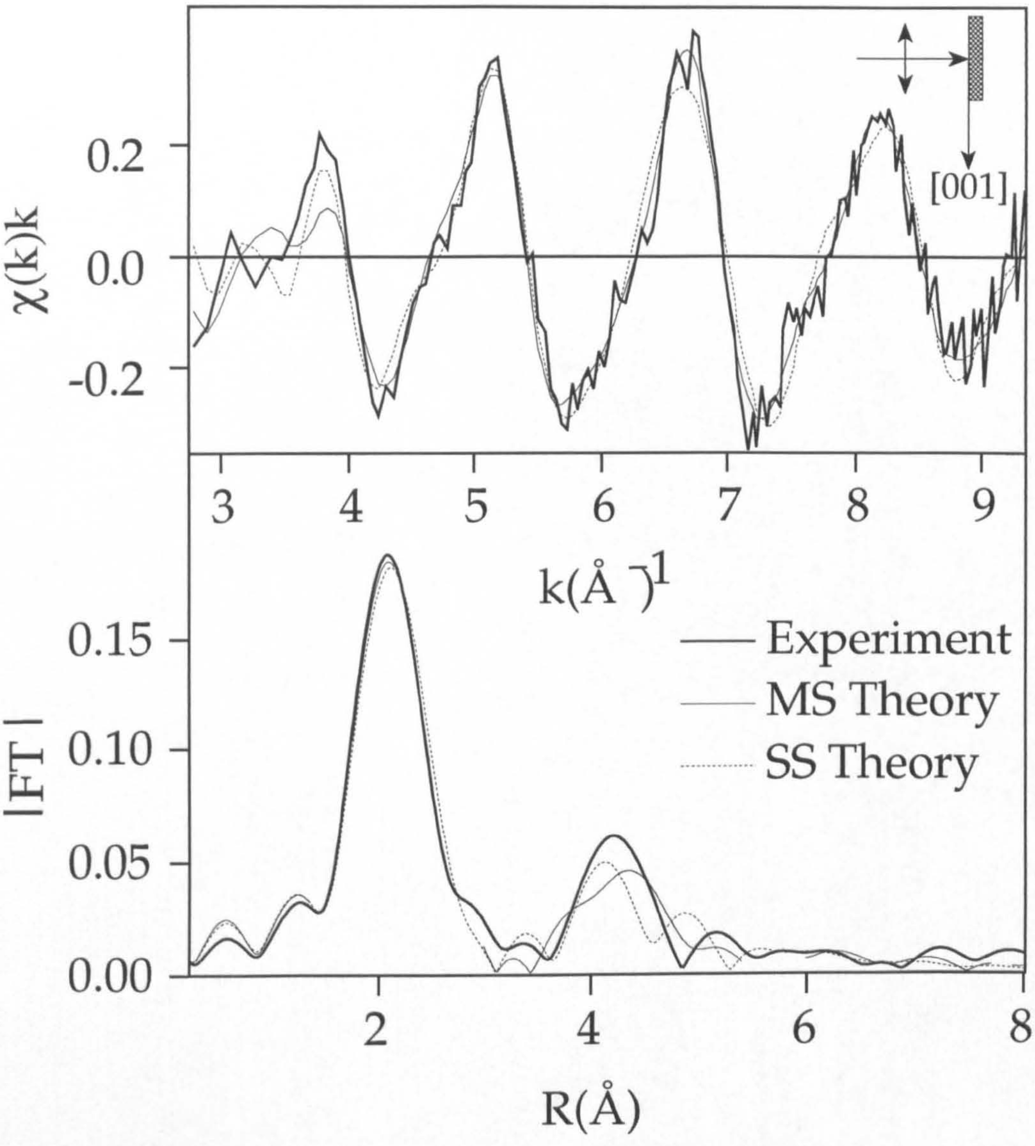

Figure 6.2 S K-edge SEXAFS spectra of Ni(110)c(2x2)S at 95 K after background subtraction, conversion to k space and weighting by k. The experimental data are compared with the best fit from calculations in the single scattering approximation as well as with calculations which include up to third order multiple scattering events. Spectra were recorded at an x-ray incidence angle of 90° with the **E** vector parallel to the [001] azimuth.

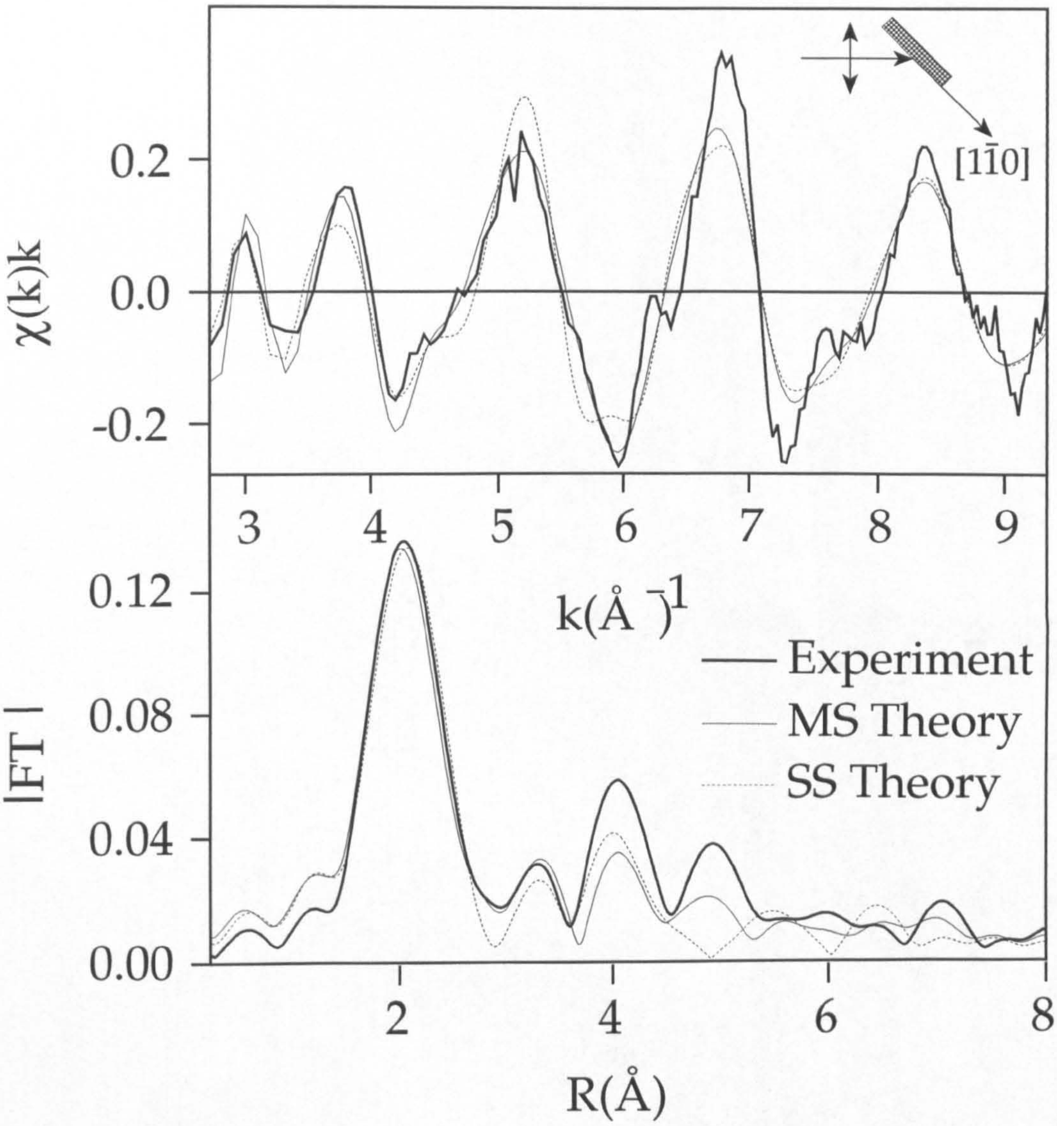

Figure 6.3 S K-edge SEXAFS spectra of Ni(110)c(2x2)S at 95 K after background subtraction, conversion to k space and weighting by k. The experimental data are compared with the best fit from calculations in the single scattering approximation as well as with calculations which include up to third order multiple scattering events. Spectra were recorded at an x-ray incidence angle of 90° with the **E** vector parallel to the $[1\bar{1}0]$ azimuth.

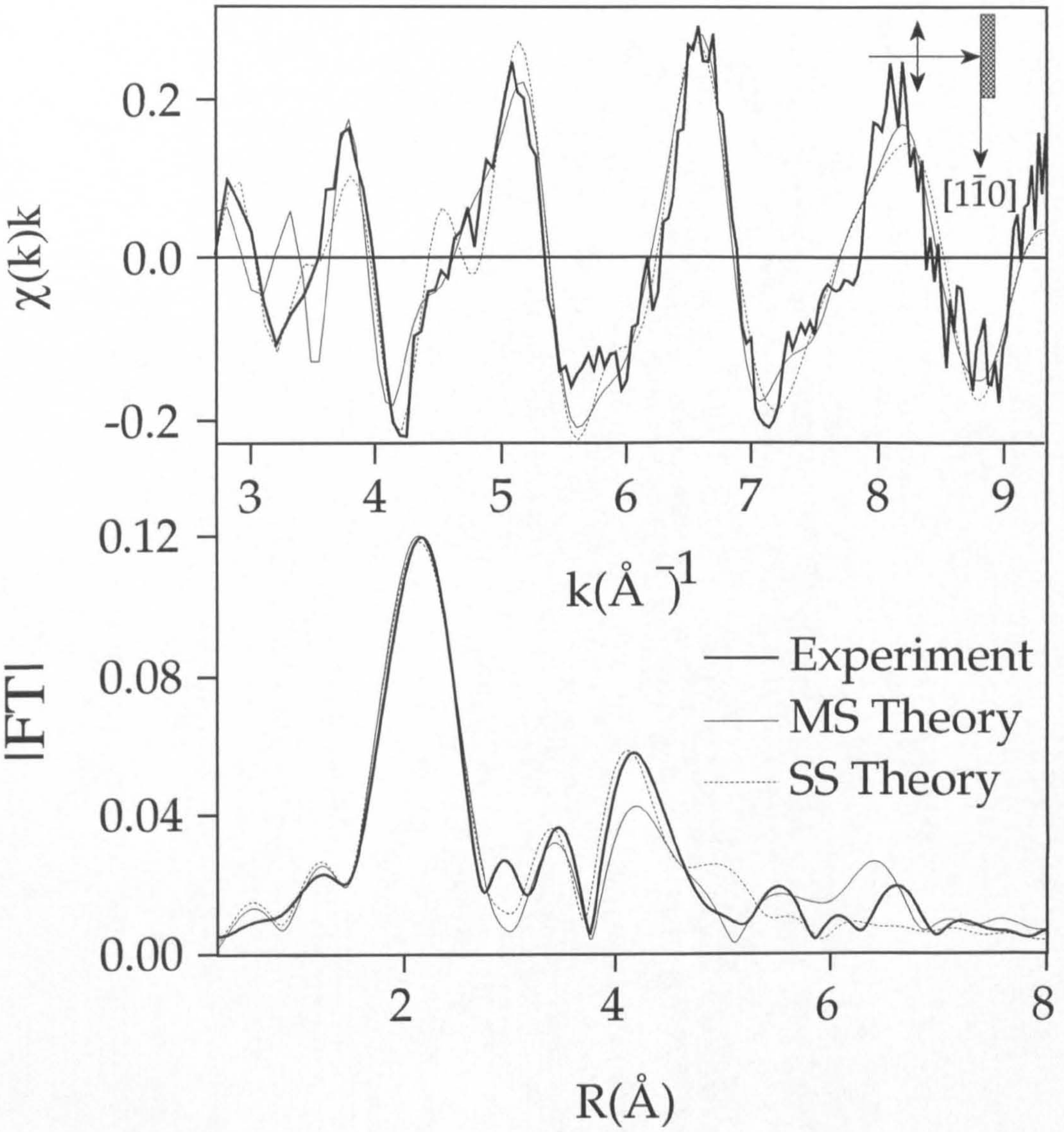

Figure 6.4 S K-edge SEXAFS spectra of Ni(110)c(2x2)S at 95 K after background subtraction, conversion to k space and weighting by k. The experimental data are compared with the best fit from calculations in the single scattering approximation as well as with calculations which include up to third order multiple scattering events. Spectra were recorded at an x-ray incidence angle of 20° with the **E** vector parallel to the $[1\bar{1}0]$ azimuth.

	Path	Path Length(Å)	Relative Intensity	Scatter Angle(°)
$[1\bar{1}0]$ Normal Incidence				
	S-2-2-S	8.132	0.0195	101.7
	S-3-2-S	10.020	0.0184	101.8
	S-6-2-S	8.965	0.0212	122.9
	S-6-2-S	11.477	0.0219	96.3
	S-S_1-2-S	8.863	0.0274	143.3
	S-S_1-6-S	10.471	0.0219	77.5
$[1\bar{1}0]$ Grazing Incidence				
	S-2-1-S	7.123	0.0162	71.8
	S-4-1-S	8.726	0.0233	119.5
	S-7-1-S	9.337	0.0121	180.0
	S-1-7-1-S	9.337	0.0104	180.0
	S-13-1-S	12.791	0.0147	149.8
[001] Normal Incidence				
	S-2-2-S	8.068	0.0282	101.7
	S-8-2-S	9.740	0.0480	163.6
	S-2-8-2-S	9.790	0.0293	163.6
	S-S_1-2-S	8.860	0.0358	143.6

Table 6.1 Principal multiple scattering pathways showing path lengths in Ångstroms and scattering angle in degrees. The intensity is the maximum of $\chi(k)k$ at any value of k in the range 3-9 Å^{-1}. The paths are labelled by the shells of atoms involved, as depicted in Figure 6.5, and suffices (a) and (b) indicate different atoms in the same shell.

derived from this work are 2.20±0.02 Å and 2.29±0.02 Å. The first shell distance differs from that recently reported by Binsted et al. (2.23±0.04 Å) [21] in a preliminary analysis of this data using Hedin-Lundqvist phase shifts. The reasons for the discrepancy in values that we have reported lie in the use of an improved background subtraction method in the present analysis. Errors in the background subtraction are compounded by a high degree of correlation between Debye-Waller-like effects and the two closely-spaced nearest-neighbour distances. This correlation is an inherent limitation in EXAFS, which cannot achieve precise radii for two such closely spaced shells unless their individual Debye-Waller-like factors can be independently established.

The values for the nearest and next-nearest S-Ni neighbour distances now determined (2.20±0.02 Å and 2.29±0.02 Å) are in excellent agreement with earlier SEXAFS and ARPEFS studies.[4-7] The surface relaxation obtained from this work is 14±3%, which is slightly larger than reported elsewhere.

A comparison of the bond distances obtained from analysis using a model containing only the first and second nearest neighbours with those obtained with a fifteen shell cluster with single scattering shows no significant variation. Nor does the error associated with the first shell radius. However, the R factor [25] decreases by 28% between the fits for the two and fifteen shell models, the corresponding error associated with the distance of the second radial shell falling to two thirds of that for the two shell model. The inclusion of multiple scattering does not alter the best-fit first and second coordination shell distances although the R factor [25] is reduced by a further 9%, indicating a more complete description of the scattering processes.

Including buckling of the second layer nickel atoms resulted in a reduction of the R-factor by 3%. However, a rigorous statistical analysis utilising a χ^2 index[26] to account for the increased degrees of freedom in the fitting procedure[27] indi-

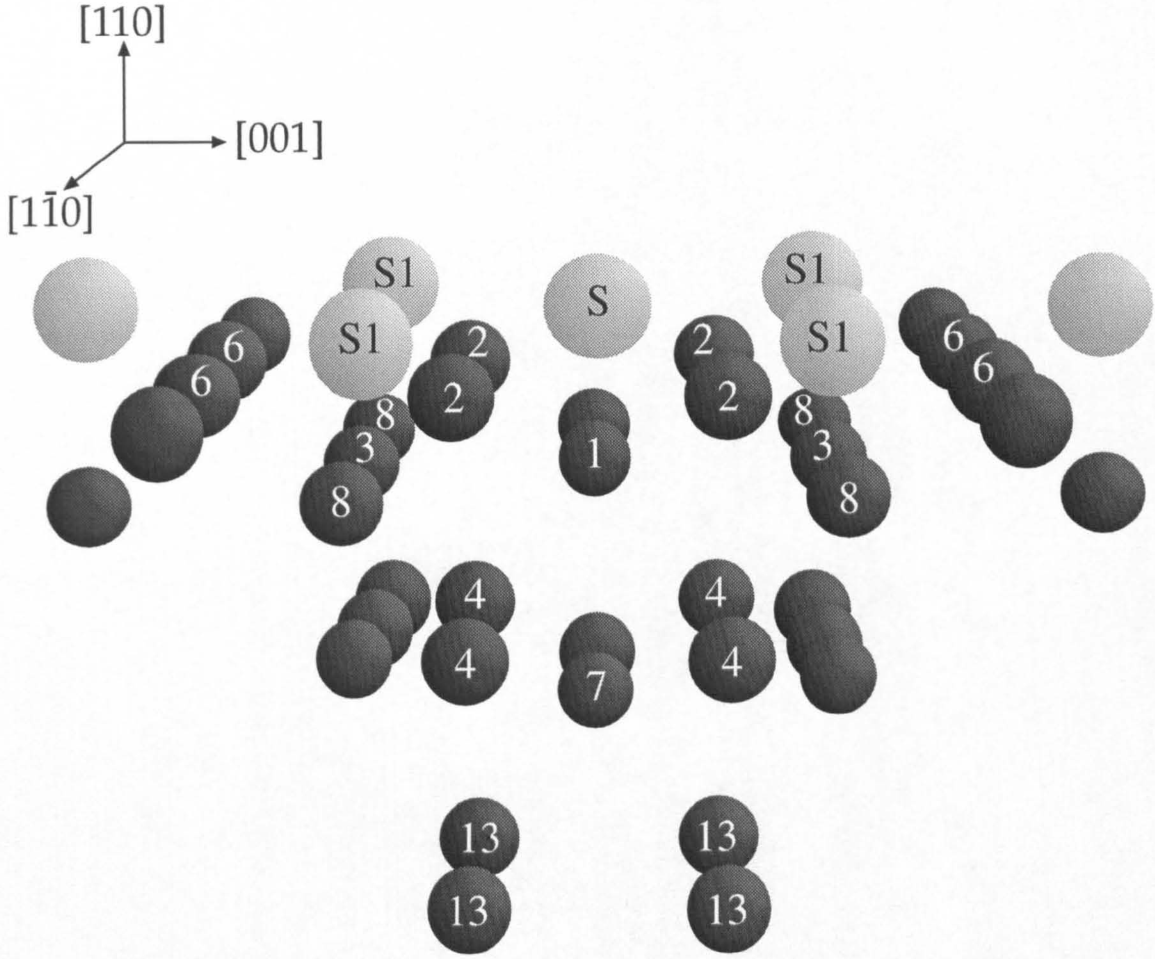

Figure 6.5 Model of Ni(110)c(2x2)S indicating the 15 shells about the S absorber which were used for fitting purposes. The numbered shells are those which contribute significantly to multiple scattering pathways. The atoms in front of shells 1 and 7 are removed for clarity.

cated that the inclusion of second layer rumpling led to a degradation of fit quality, by 1% in the χ^2 value. Hence inclusion of second layer rumpling is not justified in fitting the data presented here.

The principal multiple scattering paths observed in all three geometries are tabulated in Table 6.1, the atom types being illustrated in Figure 6.5. These paths are those consistent with occupation by S of a high symmetry site. The S atoms are closer to coplanar in this structure than with the other low index Ni surfaces ($d_{\perp}$=0.95 Å, compared to Ni(001)c(2x2)S $d_{\perp}$=1.3 Å and Ni(111)p(2x2)S $d_{\perp}$=1.4 Å),[2] thus enhancing the multiple scattering.[17,18]

The multiple scattering paths available in a face centred cubic lattice lead to numerous and significant contributions from pathways other than the colinear focusing paths[28] which are seen to dominate in simple cubic systems.[29] This is exemplified by both the double and triple scattering colinearly focused paths, {S-S_1-1-S} and {S-1-S_1-1-S} (for a description of the labelling system see Figure 6.5). These contribute less to the backscattering amplitude in the grazing incidence spectrum than the shorter {S-4-1-S} pathway (see Table 6.1). The importance of the collinear paths is evidenced by the contribution made to the Fourier transform at the half path length of 4.7 Å (Figure 6.3). In both normal incidence spectra there are significant contributions to the EXAFS due to multiple scattering with half path lengths in the 4.8 - 5.5 Å range and it is here that the largest differences between multiple and single scattering become evident, especially in the $[1\bar{1}0]$ azimuth spectrum. The multiple scattering paths responsible for this are the {S-3-2-S} and {S-S_1-6-S}, with total path lengths of 10.02 Å and 10.47 Å, respectively. The triple scattering pathway {S-2-8-2-S} and the double scattering pathway {S-8-2-S} in the [001] azimuth spectrum have a similar effect to {S-3-2-S} and {S-S_1-6-S} in the $[1\bar{1}0]$ azimuth spectrum. Path lengths in excess of 5 Å are found to have an appreciable effect in both grazing and normal incidence spectra, resulting in peaks in the theoretical Fourier transforms with analogous features in the experimental data. In the grazing incidence spectrum the {S-13-1-S} path with a half path length of 6.4 Å has a limited yet noticeable effect on the Fourier transform and the {S-6-2-S} path in the $[1\bar{1}0]$ azimuth spectrum results in an appreciably large feature corresponding to an overall path length of 11.48 Å.

6.4 Conclusion

To summarise, analysis of SEXAFS data from Ni(110)c(2x2)S indicate that the first and second shell distances about S in the hollow site are 2.20±0.02 Å and 2.29±0.02 Å. The shorter distance is to a second layer Ni atom directly under S. The previously reported rumpling of the second layer nickel atoms was not discernible. The principal multiple scattering paths have been identified and their inclusion in the data analysis yields a significant improvement in the quality of the theoretical fit. However, inclusion of multiple scattering does not significantly influence the derived first and second shell distances about S.

References

1. T. Lederer, D. Arvanitis, M. Tischer, G. Comelli, L. Tröger and K.Baberschke, Phys. Rev. B., **48**, 11277, (1993)

2. J.E. Demuth, D.W. Jepsen and P.W. Marcus, Phys. Rev. Lett., **32**, 1182, (1974)

3. J.F. van der Veen, R.M. Tromp, R.G. Smeek and F.W. Saris, Surf. Sci., **53**, 501, (1975)

4. S.W. Robey, J.J. Barton, C.C. Bahr, G. Liu and D.A. Shirley, Phys. Rev. B, **35**, 1108, (1987)

5. D.R. Warburton, P.L. Wincott, G. Thornton, D. Norman, C.H. Richardson, F.M. Quinn and R. McGrath, Vacuum, , (1988) 241.

6. T. Ohta, Y. Kitajima, P.M. Stefan, M.-L. Stefan, N. Kosugi and H. Kuroda, J. de Phys., **47**, C8-503, (1986)

7. T. Yokohama, H. Hamamatsu, Y. Kitajima, Y. Takata, S. Yagi and T. Ohta, Surf. Sci., **313**, 197 (1994)

8. D.R. Warburton, G.Thornton, D. Norman, C.H. Richardson and R. McGrath, Phys. Rev. B, **43**, 12289, (1991)

9. F. Sette, T. Hashizume, F. Comin, A.A. MacDowell and P.H. Citrin, Phys. Rev. Lett., **61**, 1384, (1988)

10. S.J. Gurman, N. Binsted and I. Ross, J. Phys. C., **17**, 143 (1984)

11. S.J. Gurman, N. Binsted and I. Ross, J. Phys. C., **19**,1845 (1986)

12. N. Binsted and D. Norman, in "The Structure of Surfaces IV", Eds. Xide Xie, S.Y. Tong and M.A. Van Hove, (World Scientific, Singapore, 1994)

13. A.W. Robinson, S. D'Addato, V.R. Dhanak, P. Finetti and G. Thornton, Rev. Sci. Instrum., **66**, 1769, (1995)

14. G. van der Laan and H.A. Padmore, Nucl. Instrum. Meth. A, **291**,225, (1990)

15. D.A. Fischer and C.Y. Yang, Nucl. Instrum. Meth. A, **291**, 123, (1990)

16. Available from N. Binsted.

17. N. Binsted and D. Norman, Phys. Rev. B, **49**,15531, (1994)

18. N. Binsted and D. Norman, Japan. J. Appl. Phys., **Suppl. 32-2**, 342, (1993)

19. S.J. Gurman, J. Phys. C: Solid State Phys., **21**, 3699, (1988)

20. D. R. Warburton, D. Purdie, C. A. Muryn, N. S. Prakash, K. Prabhakaran, G. Thornton, R. A. D. Pattrick and D. Norman, Phys. Rev. B, **45**, 12043, (1992)

21. N. Binsted, D. Norman and G. Thornton, Phys. Rev. B, **51**, 7905 (1995)

22. L. Hedin and S. Lundqvist, Solid State Phys., **23**, 1, (1969)

23. J.M. Tranquada and R. Ingalls, Phys. Rev. B., **28**, 3520 (1983)

24. N. Binsted, M.T. Weller and J. Evans, J. Am. Chem. Soc., **118**, 10200, (1996)

25. N. Binsted, R.W. Strange and S.S. Hasnain, Biochem., **31**,1211, (1992)

26. G. Bunker, D. Crozier, N. Binsted, Y. Ma, A. McKale, E.A. Stern, M. Vaarkamp and K. Zhang, Data Analysis Subgroup Report, International Workshops on Standards and Criteria in XAFS, X-Ray Absorption Fine Structure, Ed. S. Samar Hasnain, (Ellis Horwood, London, 1991).

27. R.W. Joyner, K.J. Martin and P. Meehan, J. Phys. C: Solid State Phys., **20**, 4005, (1987)

28. P.A. Lee and J.B. Pendry, Phys. Rev. B, **11**, 2795, (1975)

29. A.I. Frenkel, E.A. Stern, M. Qian and M. Newville, Phys. Rev. B, **48**, 12449, (1993)